Regular Article

The electron capture in ¹⁶³Ho experiment – ECHo

L. Gastaldo[1,a], K. Blaum[2], K. Chrysalidis[3], T. Day Goodacre[4], A. Domula[5],
M. Door[2], H. Dorrer[6,7,8], Ch.E. Düllmann[6,9,10], K. Eberhardt[6,10], S. Eliseev[2],
C. Enss[1], A. Faessler[11], P. Filianin[2], A. Fleischmann[1], D. Fonnesu[1], L. Gamer[1],
R. Haas[6], C. Hassel[1], D. Hengstler[1], J. Jochum[12], K. Johnston[4], U. Kebschull[13],
S. Kempf[1], T. Kieck[3,6], U. Köster[14], S. Lahiri[15], M. Maiti[16], F. Mantegazzini[1],
B. Marsh[4], P. Neroutsos[13], Yu.N. Novikov[2,17,18], P.C.O. Ranitzsch[1,b], S. Rothe[4],
A. Rischka[2], A. Saenz[19], O. Sander[20], F. Schneider[3,6], S. Scholl[12], R.X. Schüssler[2],
Ch. Schweiger[2], F. Simkovic[21], T. Stora[4], Z. Szücs[22], A. Türler[7,8], M. Veinhard[4],
M. Weber[20], M. Wegner[1], K. Wendt[3], and K. Zuber[5]

1   Kirchhoff Institute for Physics, Heidelberg University, Heidelberg, Germany
2   Max-Planck Institute for Nuclear Physics, Heidelberg, Germany
3   Institute for Physics, Johannes Gutenberg-University, Mainz, Germany
4   ISOLDE, CERN, Geneve, Switzerland
5   Institute for Nuclear and Particle Physics, TU Dresden, Germany
6   Institute for Nuclear Chemistry, Johannes Gutenberg University, Mainz, Germany
7   Laboratory of Radiochemistry and Environmental Chemistry, Department Biology and
    Chemistry, Paul Scherrer Institute, Villigen PSI, Switzerland
8   Laboratory of Radiochemistry and Environmental Chemistry, Department of Chemistry
    and Biochemistry, University of Bern, Freiestrasse 3, Bern, Switzerland
9   GSI Helmholtzzentrum für Schwerionenforschung, Darmstadt, Germany
10 Helmholtz Institute Mainz, Mainz, Germany
11 Institute for Theoretical Physics, University of Tübingen, Tübingen, Germany
12 Physics Institute, University of Tübingen, Germany
13 Goethe-Universität, Frankfurt am Main, Germany
14 Institut Laue-Langevin, Grenoble, France
15 Chemical Sciences Division, Saha Institute of Nuclear Physics, 1/AF Bidhannagar,
    Kolkata, India
16 Department of Physics, Indian Institute of Technology Roorkee, Roorkee, India
17 Petersburg Nuclear Physics Institute, Gatchina, Russia
18 St.Petersburg State University, St. Petersburg, Russia
19 Institut für Physik, Humboldt-Universität zu Berlin, Berlin, Germany
20 Karlsruhe Institute of Technology, Institute for Data Processing and Electronics,
    Karlsruhe, Germany
21 Department of Nuclear Physics and Biophysics, Comenius University, Bratislava,
    Slovakia
22 Institute of Nuclear Research of the H.A.S., Bem ter 18/C, Debrecen, Hungary

a   e-mail: Loredana.Gastaldo@kip.uni-heidelberg.de
b   *Present address*: Institut für Kernphysik, Universität Münster, Münster, Germany

Abstract. Neutrinos, and in particular their tiny but non-vanishing masses, can be considered one of the doors towards physics beyond the Standard Model. Precision measurements of the kinematics of weak interactions, in particular of the ^{3}H β-decay and the ^{163}Ho electron capture (EC), represent the only model independent approach to determine the absolute scale of neutrino masses. The electron capture in ^{163}Ho experiment, ECHo, is designed to reach sub-eV sensitivity on the electron neutrino mass by means of the analysis of the calorimetrically measured electron capture spectrum of the nuclide ^{163}Ho. The maximum energy available for this decay, about 2.8 keV, constrains the type of detectors that can be used. Arrays of low temperature metallic magnetic calorimeters (MMCs) are being developed to measure the ^{163}Ho EC spectrum with energy resolution below 3 eV FWHM and with a time resolution below 1 μs. To achieve the sub-eV sensitivity on the electron neutrino mass, together with the detector optimization, the availability of large ultra-pure ^{163}Ho samples, the identification and suppression of background sources as well as the precise parametrization of the ^{163}Ho EC spectrum are of utmost importance. The high-energy resolution ^{163}Ho spectra measured with the first MMC prototypes with ion-implanted ^{163}Ho set the basis for the ECHo experiment. We describe the conceptual design of ECHo and motivate the strategies we have adopted to carry on the present medium scale experiment, ECHo-1K. In this experiment, the use of 1 kBq ^{163}Ho will allow to reach a neutrino mass sensitivity below 10 eV/c^2. We then discuss how the results being achieved in ECHo-1k will guide the design of the next stage of the ECHo experiment, ECHo-1M, where a source of the order of 1 MBq ^{163}Ho embedded in large MMCs arrays will allow to reach sub-eV sensitivity on the electron neutrino mass.

1 Introduction

Although the current Standard Model (SM) is a very successful and accurate description of particle physics, we know it is incomplete and an extension is needed to understand the structure of the universe, the hierarchy of masses and to achieve a grand unification. At the Large Hadron Collider (LHC) so far experimental hints to physics beyond the SM are missing and the favored supersymmetric extension of the SM seems to be less likely. The observation of neutrino oscillations [1,2] about 20 years ago, establishing that neutrinos must be massive, gives a clear hint of physics beyond the SM. To guide the development of theories beyond the SM, one of the most interesting open questions is therefore the absolute scale of neutrino masses.

From neutrino oscillations, only the differences of the masses squared can be extracted [3], but not the absolute values. The determination of the neutrino mass scale is a challenging task due to the smallness of the masses and to the weak interaction with other standard model particles. There exist several approaches which can potentially yield this result: the analysis of the visible structures in the universe [4], the observation of neutrinoless double beta decay [5,6] and resonantly enhanced double electron capture [7], the measurement of the time of flight of neutrinos emitted in supernova explosions [8] and the analysis of the kinematics of low energy beta decays and electron capture (EC) processes [9]. In particular, direct kinematical methods allow to perform a model-independent measurement of the electron neutrino and antineutrino mass with high sensitivity and low systematic uncertainties. In the past this approach was mainly driven by the investigation of the ^{3}H beta spectrum. KATRIN, the KArlsruhe TRItium Neutrino experiment [10], is designed to either measure the electron-antineutrino mass down to 0.3 eV/c^2 or alternatively give an upper limit of

$0.2\,\mathrm{eV}/c^2$ with 95% C.L. [9]. These values are approximately a factor of ten smaller than the 95% C.L. upper limits of 2.12 and $2.30\,\mathrm{eV}/c^2$ that the two precursor experiments, "Troitsk neutrino mass experiment" and "The Mainz Neutrino mass experiment" respectively, determined [11–13]. Together with KATRIN, two other experiments are designed to improve the limit on the electron anti-neutrino mass analyzing the ^{3}H beta-spectrum, these are Project8 [14] and PTOLEMY [15]. The most stringent limit for the electron neutrino mass is $m_{\nu_e} < 225\,\mathrm{eV}/c^2(95\%\ \mathrm{C.L.})$ obtained by the analysis of the Internal Bremsstrahlung in Electron Capture (IBEC) spectrum of ^{163}Ho [16]. The Electron Capture in ^{163}Ho experiment, ECHo, is designed to investigate the electron neutrino mass in the sub-eV region by the analysis of the calorimetrically measured electron capture spectrum of ^{163}Ho.

2 Electron capture in ^{163}Ho and neutrino mass

Given the present knowledge, ^{163}Ho is the best candidate to perform an experiment to investigate the neutrino mass in the sub-eV region. The half-life of ^{163}Ho is $T_{1/2} = 4570 \pm 50$ y [17,18]. According to the last release of the Atomic-Mass Evaluation by Audi et al. [19], the recommended value for the energy available to the decay of ^{163}Ho is $Q_{\mathrm{EC}} = 2.555 \pm 0.016\,\mathrm{keV}$ obtained by combining several measurements whose results actually span over a larger range, from $Q_{\mathrm{EC}} = 2.3 \pm 1\,\mathrm{keV}$ [20] to $Q_{\mathrm{EC}} \simeq 2.8\,\mathrm{keV}$ [21,22]. In all these measurements the Q_{EC}-value was determined by the analysis of the energy spectrum of ^{163}Ho, measured with different techniques. In order to remove any systematic error in the interpretation of the measured spectra, which could have led to the large discrepancies, the ECHo collaboration has recently determined the energy available to the decay of ^{163}Ho by directly measuring the mass difference between ^{163}Ho and ^{163}Dy using the Penning-trap mass spectrometry technique (PTMS). The result is $Q_{\mathrm{EC}} = 2.833 \pm 0.030_{\mathrm{stat}} \pm 0.015_{\mathrm{syst}}\,\mathrm{keV}$ [23]. The experimental technique and the challenges to reduce the uncertainties on the Q_{EC}-value to 1 eV will be described in Section 9.

In the EC process, a $^{163}_{67}$Ho nucleus ($J^P = 7/2^-$) decays to a $^{163}_{66}$Dy nucleus ($J^P = 5/2^-$) by capturing an electron from an inner atomic shell and emitting an electron neutrino. A tiny fraction of energy, less than 1 meV, is taken by the nuclear recoil due to the emission of the neutrino. The rest of the energy is shared between the emitted electron neutrino and the atomic excitations of the daughter atom ^{163}Dy. The small Q_{EC}-value energetically limits the capture processes to electrons occupying the third and higher shells. Among those, only electrons from s-levels and $p_{1/2}$-levels can be captured due to angular momentum conservation and to the finite overlap of their wave function with the nucleus.

The excited state in which the daughter atom ^{163}Dy is left after the EC in ^{163}Ho is characterized, for first order transitions, by a hole in an inner shell, corresponding to the captured electron, and an additional electron in the $4f$-shell. Higher order excited states with more than one hole in the atomic shells, due to shake-up or shake-off processes, have a much smaller probability to be created [24]. As discussed in Section 10 only the second order excitations, with two holes in the atomic shells, are expected to give a non-negligible contribution to the spectral shape.

The atomic de-excitation includes cascades of both X-rays and electrons (Auger electrons and those from Coster-Kronig transitions). The corresponding spectrum is slightly influenced by a non-zero neutrino mass, since this reduces the energy available to the decay. For the EC process, as for the beta decay, the largest effect of a non-zero neutrino mass on the spectral shape is close to the end-point of the spectrum itself. Therefore, also in this case, a small energy available for the decay, Q_{EC}, will lead to a larger fraction of events in the interesting region close to the end-point, rendering

isotopes with low Q-values as the most favorable for neutrino mass determination by electron capture and beta decay.

The interest in ^{163}Ho as a candidate to be used in an experiment investigating the electron neutrino mass started more than thirty years ago at the Department of Physics and Chemistry of Princeton University [25]. In early experiments only the emitted photons were measured. Two different strategies were used to constrain the neutrino mass: the analysis of the X-ray spectrum and the analysis of the Internal Bremsstrahlung in Electron Capture, IBEC spectrum. In the early phase the first approach was used by several groups [20,25,26] and led eventually to an upper limit for the electron neutrino mass of $m_{\nu_e} < 490\,\mathrm{eV}/c^2$ (68% C.L.) [27] obtained by analyzing the M-lines and N-lines of the ^{163}Ho X-ray spectrum. The second method, the analysis of the inner Bremsstrahlung photons, led to an even more stringent limit of $m_{\nu_e} < 225\,\mathrm{eV}/c^2$ (95% C.L.) [16], which is still today the best upper limit on the electron neutrino mass.

In 1982 De Rujula and Lusignoli pointed out for the first time that by performing a calorimetric measurement of the ^{163}Ho de-excitation spectrum, i.e. by measuring for each event the sum of the energies of all emitted photons, electrons and nuclear recoil with one single detector, the sensitivity to the neutrino mass is significantly increased [28,29]. This can be achieved when the source is completely contained within the detector itself, ensuring a quantum efficiency for the emitted particles, besides the electron neutrino, of practically 100 %. In this case all the energy emitted in the EC process minus the energy taken away by the neutrino is measured. The interpretation of the spectrum is therefore not affected by possible systematic errors due to the imperfect knowledge of branching ratios for the different de-excitation modes as well as to the necessary correction for energy self-absorption in the source, typical for X-ray measurements.

Following this idea, new kinds of experiments were developed. The first calorimetric measurement of the ^{163}Ho spectrum was performed by the collaboration of a group of Aarhus University and the ISOLDE group [30]. In this experiment the ^{163}Ho ions have been implanted into a Si(Li) detector. A second calorimetric spectrum of ^{163}Ho was measured by a group from Princeton University [31]. They used a gas proportional counter in which the ^{163}Ho ions where bound in the volatile compound Ho(fod)$_3$, where "fod" stands for fluoro-octanedione. A third measurement, the first using a low temperature microcalorimeter, was performed by a group of Genoa University (Italy) [21]. In this experiment, a small drop of a few micro-liters containing ^{163}Ho in an organic solution (2-Hydroxyisobutyric acid, α-HIBA) was put on a tin foil (about $1\,\mathrm{mm}^2$), dried and then covered by a second tin foil to form the absorber of the detector ensuring a quantum efficiency close to 100 %. The results of this experiment already indicated the larger potential of a low temperature calorimetric measurement over conventional detectors such as Si(Li) and proportional counters. However the development of suitable low temperature detectors was still in its infancy and more than a decade had to pass before it was possible to show that cryogenic microcalorimeters, optimized for the calorimetric measurement of the ^{163}Ho EC spectrum, can reach the performance required for a competitive neutrino mass experiment.

The first measurement with a fully micro-fabricated metallic magnetic calorimeter having ^{163}Ho ions implanted in a gold absorber (the detectors are described in Sect. 4) and having an energy resolution of ΔE_{FWHM} of 12 eV, resulted in a ^{163}Ho EC spectrum with unmatched precision, opening the path to a promising neutrino mass experiment using this isotope [22,32]. As a result of this, the international ECHo collaboration was formed and the design of the large scale ECHo experiment, which we discuss in this volume, was started [33]. Meanwhile two further large collaborations have established with the aim to develop large scale experiments based on cryogenic detectors to reach sub-eV sensitivity on the electron neutrino mass

using ^{163}Ho: the "Electron Capture Decay of ^{163}Ho to Measure the Electron Neu-trino Mass with sub-eV Sensitivity" (HOLMES) [34] and the "Neutrino Mass via Electron Capture Spectroscopy" (NuMECS) [35,36].

3 Neutrino mass sensitivity of ^{163}Ho-based experiments

3.1 ^{163}Ho electron capture spectrum

As discussed above, in a well-designed calorimetric measurement, all of the energy released in the decay of ^{163}Ho, except that taken away by the electron neutrino, contributes to the signal. The measured total energy includes all of the photons and electrons emitted in the atomic de-excitation as well as the tiny nuclear recoil. This last contribution, the nuclear recoil, which is vanishing near the endpoint of the spectrum, where the neutrino is not relativistic, will be neglected in the following. In this approximation, the ^{163}Ho spectrum is identical to the de-excitation spectrum of the daughter atom ^{163}Dy. Considering only first order excitations with one hole in the level H, corresponding to the eigenstate of the electron that has been captured, and one additional electron in the $4f$ shell, the shape of the spectrum is:

$$\frac{\mathrm{d}N}{\mathrm{d}E_\mathrm{C}} = A(Q_\mathrm{EC}-E_\mathrm{C})^2\sqrt{1-\frac{m_{\nu_e}^2}{(Q_\mathrm{EC}-E_\mathrm{C})^2}}\sum_H C_H n_H B_H\,\phi_H^2(0)\frac{\Gamma_H/2\pi}{(E_\mathrm{C}-E_H)^2+\Gamma_H^2/4}.$$

$$(1)$$

Equation (1) shows Breit-Wigner resonances centered at the energies E_H, given, to a first approximation, by the difference between the energy of the electron that has been captured, with respect to the daughter atom and the energy of the extra-electron in the $4f$-shell, with respect to the holmium atom. The resonances have an intrinsic width Γ_H related to the half-life of the excited states. The intensities of these lines are given mainly by the squared wave-function of the captured electron calculated at the ^{163}Ho nucleus, $\phi_H^2(R)$, with a small correction, B_H, due to exchange and overlap. These factors are then multiplied by the nuclear shape factors C_H which in the following are considered to be constant, and the fractions of occupancy n_H of the atomic shells H, which are considered to be 1 for each shell involved in the process. The Breit-Wigner resonances are then weighted by the phase space factor, which depends on the square of the electron neutrino mass $m_{\nu_e}^2$ and the energy available to the decay, Q_EC.

Due to the low Q_EC-value and considering only first order transitions, the ^{163}Ho spectrum consists of the following lines: MI ($3s$ electrons), MII ($3p_{1/2}$ electrons), NI ($4s$ electrons), NII ($4p_{1/2}$ electrons), OI ($5s$ electrons), OII ($5p_{1/2}$ electrons) and PI ($6s$ electrons). The binding energies of these electrons, E_H^bin, related to the dysprosium atom, and the intrinsic linewidths Γ_H of the transition are given in Table 1 for all the lines that have been measured with the calorimetric technique. As expected, the measured peak energies for the lines in the spectrum, stated in column 2 of Table 1, are slightly smaller with respect to the binding energies. In addition, higher order transitions modify the spectral shape by adding a number of resonances with capture probabilities smaller than 1% with respect to the probability to capture $3s$ electrons, according to [24]. Different theoretical calculations have already been performed in order to model the influence of higher order transitions [24,37–40] and will be discussed in Section 10. Since contributions of the higher order processes are rather small and the theoretical description is presently not fully clear, the estimation of the neutrino mass sensitivity of ECHo is evaluated by considering only the first

Table 1. Binding energies $E_{\rm bin}^{\rm lit}$ of the electrons in Dy and linewidths $\Gamma_H^{\rm lit}$ as reported in [46] and the corresponding experimental values as derived from the analysis of the calorimetrically measured spectra with enclosed ^{163}Ho [22], $E_{\rm bin}^{\rm exp}$ and $\Gamma_H^{\rm exp}$, respectively.

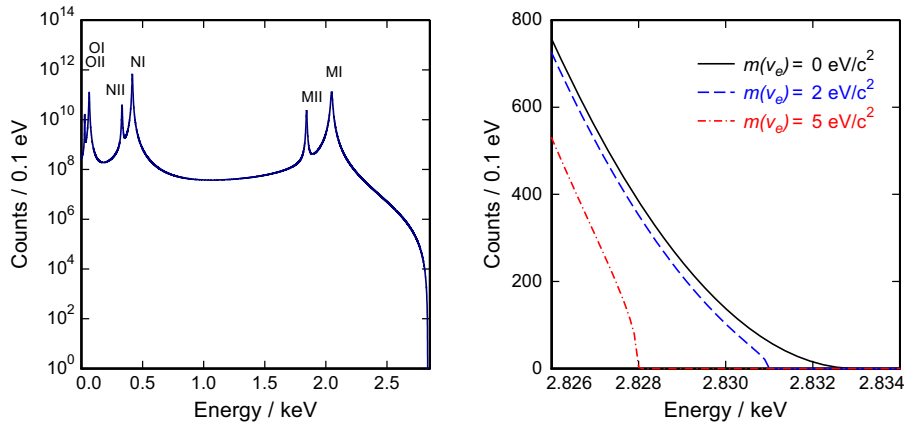| Level	$E_{\rm bin}^{\rm lit}$ (eV) [42]	$E_{\rm bin}^{\rm exp}$ (eV) [62]	$\Gamma_H^{\rm lit}$ (eV) [44]	$\Gamma_H^{\rm exp}$ [eV] [62]
M I	2046.9	2040	13.2	13.4
M II	1844.6	1836	6.0	4.8
N I	420.3	411	5.4	4.7
N II	340.6	333	5.3	13.0
O I	49.9 [43]	48	3.7 [45]	5.6

Fig. 1. Calculated ^{163}Ho EC spectrum for a total number of 10^{14} events using the $Q_{\rm EC} = 2.833$ keV [23], considering only first order excitations for the daughter ^{163}Dy atom using the parameters given in [41], and assuming zero neutrino mass (left). Shape of the spectrum near the endpoint calculated for neutrino masses of 0, 2 and $5\,{\rm eV}/c^2$, respectively, showing the effect of a finite electron neutrino mass on a linear scale (right).

order excitations. Higher order processes would have the effect, in proximity of the end-point, of increasing the number of counts, therefore the estimated neutrino mass limit has to be seen as an upper limit, meaning as a worst case scenario.

Figure 1 (left) shows the calculated EC spectrum of ^{163}Ho for a total number of 10^{14} events plotted on a logarithmic scale. In this calculation $Q_{\rm EC} = 2.833$ keV [23] and massless neutrinos have been assumed. All other parameters used in this calculation are taken from [41]. Several Breit-Wigner resonances, corresponding to capture processes originating from the different atomic levels, are clearly visible.

A magnification of the endpoint region of the ^{163}Ho spectra calculated assuming different neutrino masses $m(\nu_{\rm e}) = 0\,{\rm eV}/c^2, 2\,{\rm eV}/c^2$ and $5\,{\rm eV}/c^2$ is shown in Figure 1 (right). Note that the spectrum is plotted on a linear scale here. This very small part of the ^{163}Ho spectrum is most affected by a finite electron neutrino mass. The shape of the spectrum near the endpoint differs remarkably for these three different cases. It is interesting to quantify the fraction of counts expected in the case of $m(\nu_{\rm e}) = 0\,{\rm eV}/c^2$, in a small energy interval ΔE ending at $Q_{\rm EC}$, since this gives an idea of the fraction of counts that can actually be used to obtain information on the neutrino mass. Figure 2 shows how rapid this fraction decreases with the interval becoming smaller. In the last eV below $Q_{\rm EC} = 2.833$ keV the fraction of counts is only about 6×10^{-13}. This number already indicates that reaching sub-eV sensitivity on the electron neutrino mass requires more than 10^{14} events in the full energy spectrum. For acquiring such
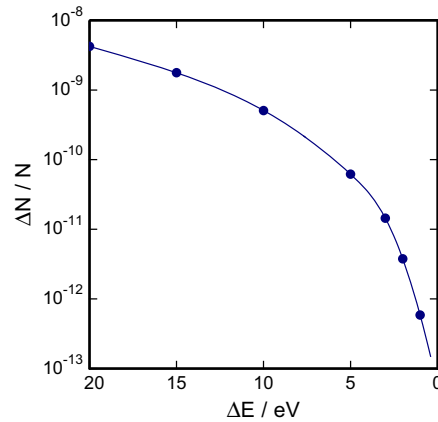
Fig. 2. Fraction of events at the endpoint region as a function of the energy interval ΔE below the endpoint calculated for $m(\nu_e) = 0 \, \text{eV}/c^2$. Solid line is a guide for the eye.

a large number of events within a measuring time of at most a few years, a ^{163}Ho activity of the order of MBq is needed. The methods to produce large quantities of ^{163}Ho for ECHo with extremely high purity will be discussed in Section 7.

3.2 Detector properties influencing the neutrino mass sensitivity

In a calorimetric measurement, each event is detected by a device with a well-defined response, which is characterized by a finite time resolution and an instrumental response function, typically a Gaussian characterized by its full-width at half maximum (FWHM). In a cryogenic calorimeter, the signal is a pulse described by its rise time, which, in first approximation, can be considered as the time resolution of the detector, its amplitude, which is proportional to the energy deposited in the detector, and its decay time, which depends on the link to the thermal bath to which the detector is coupled. In the following we will discuss important aspects in terms of detector performance that have to be considered to build a competitive experiment for neutrino mass determination based on ^{163}Ho.

The fact that each ^{163}Ho decay in the detector generates a signal with finite time resolution leads to the presence of an intrinsic source of background in the measured spectrum, namely the unresolved pile-up. An unresolved pile-up event occurs when two or more individual decays happen within a time interval that is shorter than the time resolution of the detector. In this case, the measured pulse looks like a signal corresponding to a single event with an energy approximately given by the sum of the energies of the two (or more) individual decays. Considering the case of unresolved pile-up due to only two events, the shape of the pile-up spectrum is given by the auto-convolution of the ^{163}Ho spectrum. The fraction of events leading to unresolved pile-up, f_{pu}, is given in first approximation by $f_{\text{pu}} = A \cdot \tau_{\text{res}}$, where A is the activity of the source contained in the detector and τ_{res} the time resolution of the detector.

A pile-up spectrum calculated with the parameters used for the spectrum in Figure 1, assuming an unresolved pile-up fraction $f_{\text{pu}} = 10^{-6}$ and considering a detector response with $\Delta E_{\text{FWHM}} = 3 \, \text{eV}$ is shown in Figure 3 (left) as solid red line. For comparison the ^{163}Ho spectrum, without considering any pile-up contribution, is shown as solid blue line in Figure 3 (left). The resulting total spectrum is given by the sum of the single event spectrum and the pile-up spectrum. The most interesting part near the endpoint is shown in Figure 3 (right) for neutrino masses of $0 \, \text{eV}/c^2$
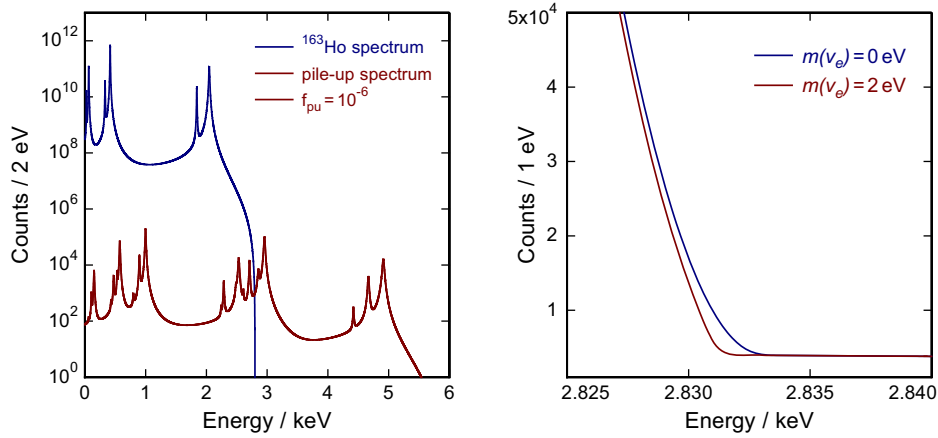
Fig. 3. (Left) Calculated ^{163}Ho EC pile-up spectrum (solid red line) assuming an unresolved pile-up fraction of 10^{-6} and the corresponding ^{163}Ho EC spectrum (solid blue line) without pile-up using the same parameters as in Figure 1. (Right) Sum of both contributions shown for the endpoint region calculated for two different values of the neutrino mass $0\,\mathrm{eV}/c^2$ and $2\,\mathrm{eV}/c^2$.

and $2\,\mathrm{eV}/c^2$ plotted with a linear y-scale. For a given detector, with a well defined rise time τ_r, which, at this stage, is assumed to be the time resolution of the detector, the requirements on the unresolved pile-up fraction constrain the maximum ^{163}Ho activity which can be enclosed in a single detector. In turn, this defines the number of detectors which needs to be used in the experiment aiming at a given total activity.

Cryogenic detectors with a rise-time as short as possible are favorable for this experiment. As discussed in more detail in Section 4, the detectors that are used for the ECHo experiment, metallic magnetic calorimeters (MMCs) [47,48], have already demonstrated an intrinsic rise time shorter than 100 ns at 30 mK [49]. This makes MMCs today by far the fastest microcalorimeter technology available at temperatures below 100 mK and therefore these constitute the best possible choice for the ECHo experiment in this respect. Despite the fast signal rise time of MMCs the total activity per detector should be kept below a few tens of Bq in order to keep the unresolved pile-up fraction below 10^{-5}, as will be discussed in the following.

Given the need of having a total ^{163}Ho activity of the order of MBq to reach a neutrino mass sensitivity in the sub-eV region, a number of the order of 10^5 single pixels is required. The availability of a multiplexed readout scheme for thousands of detectors is essential. Therefore a second very important property of the detector technology is its compatibility with multiplexed readout schemes able on one hand to preserve the performance of the single pixel readout and on the other hand to keep the total number of readout channels reasonably small. For MMCs, microwave SQUID multiplexing [50] is currently being developed and has already yielded promising results. This aspect will be discussed in more detail in Section 6.

The third property which can strongly affect the achievable neutrino mass sensitivity is the energy resolution, defined as the full width at half maximum of the Gaussian detector response, ΔE_FWHM. In particular, at the endpoint region of the spectrum, a very good energy resolution reduces the smearing of the data and increases the possibility to resolve the shape of the spectrum and to better distinguish between ^{163}Ho events and background. A FWHM of the order of a few eV enables all the structures present in the ^{163}Ho spectrum to be resolved, thus reducing possible systematic errors. MMCs developed for X-ray spectroscopy have already shown an
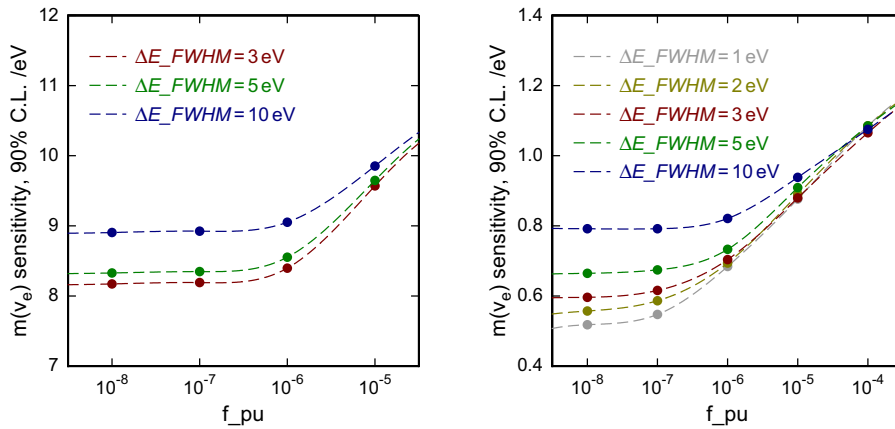
Fig. 4. Achievable sensitivity at 90% C.L. for an experiment collecting a total statistics of 10^{10} events as a function of the unresolved pile-up fraction for three different energy resolutions (left). Achievable sensitivity at 90% C.L. for an experiment collecting a total statistics of 10^{14} events as a function of the unresolved pile-up fraction for five different energy resolutions (right). For all the curves, $Q_{EC} = 2.833\,\text{keV}$ was used and the only considered background source was the unresolved pile-up.

energy resolution of $1.6\,\text{eV}$ FWHM at $5.9\,\text{keV}$ [51], which is comparable with the best energy resolution achieved by any kind of cryogenic detector at this energy. Therefore the MMC detector technology also appears to be well suited also in this respect for the ECHo experiment. Further details regarding this point will be discussed in Section 4.1.

The role of the unresolved pile-up fraction and of the energy resolution of the detectors with respect to the achievable sensitivity on the electron neutrino mass is shown in Figure 4 (left and right). Figure 4 (left) shows the sensitivity at 90% C.L. that can be achieved in an experiment measuring 10^{10} events in the full spectrum as a function of the unresolved pile-up fraction for three different detector responses, characterized by the their energy resolutions $\Delta E_{\text{FWHM}} = 3\,\text{eV}$, $\Delta E_{\text{FWHM}} = 5\,\text{eV}$ and $\Delta E_{\text{FWHM}} = 10\,\text{eV}$. Due to the relatively small statistics of 10^{10} counts, improvements on the unresolved pile-up fraction to $f_{\text{pu}} \leq 10^{-6}$ lead to almost negligible improvements in the sensitivity. In fact, only one event is expected in the energy region between $Q_{EC} - 5\,\text{eV}$ and Q_{EC}. For the same reason, improving the energy resolution to value better than $\Delta E_{\text{FWHM}} = 5\,\text{eV}$ does not lead to a better limit on the electron neutrino mass. It is important to mention that these curves have been calculated considering the only background source to be the unresolved pile-up events. The reason behind this approximation is that we aim to push the external background level at the endpoint region of the spectrum to be smaller than the intrinsic background level due to unresolved pile-up events. As a consequence, we could set a limit on the unresolved pile-up fraction of $f_{\text{pu}} \leq 10^{-5}$. This scenario is expected to be reached in the first phase of ECHo, ECHo-1k (see Sect. 11.1), where 100 pixels, each with about 10 Bq of ^{163}Ho will be measured for about one year. In this case the requirement on the unresolved pile-up leads to a limit for the external background of the order of 10^{-5} counts/eV/det/day. The challenges and methods to characterize and suppress the background in ECHo-1k and in general for the future ECHo phases are described in Section 8.

Figure 4 (right) shows the achievable sensitivity as a function of the unresolved pile-up fraction for an experiment with 10^{14} events in the full ^{163}Ho spectrum. The availability of increased statistics at the endpoint region of the spectrum enhances the
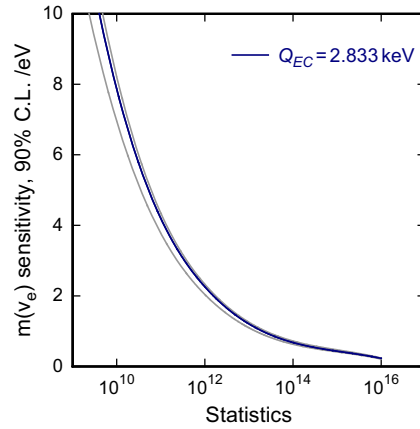
Fig. 5. Neutrino mass sensitivity as function of the total number of events for $Q_{\mathrm{EC}} = 2.833\,\mathrm{keV}$ assuming a detector energy resolution of $3\,\mathrm{eV}$ and an unresolved pile-up fraction of 10^{-6}. The region bordered by the grey lines reflects the achievable sensitivity for Q_{EC} lying between $2.7\,\mathrm{keV}$ and $2.9\,\mathrm{keV}$.

effects of the unresolved pile-up fraction and of the energy resolution on the achievable sensitivity. It is remarkable how, for an unresolved pile-up fraction of $f_{\mathrm{pu}} = 10^{-8}$, a large improvement on the achievable sensitivity to small neutrino masses can be obtained by increasing the energy resolution of the detectors from $\Delta E_{\mathrm{FWHM}} = 10\,\mathrm{eV}$ to $\Delta E_{\mathrm{FWHM}} = 1\,\mathrm{eV}$. In this analysis, the effect vanishes by increasing the unresolved pile-up fraction. Already for $f_{\mathrm{pu}} = 10^{-5}$, the achievable sensitivity is dominated by the background due to the unresolved pile-up events. At this point an important consideration should be done: an unresolved pile-up fraction $f_{\mathrm{pu}} = 10^{-8}$ in combination with a rise time of the detectors of $\tau_{\mathrm{r}} = 10^{-7}\,\mathrm{s}$ would lead to a maximum activity in a detector of $A = 0.1\,\mathrm{Bq}$, which, in turn, would require a larger number of single detectors, making any experiment more demanding. In a second phase of the ECHo experiment, ECHo-1M (see Sect. 11.2), we plan to reach a number of measured ^{163}Ho decays of the order of 10^{14}. For this experiment, we aim to reduce the unresolved pile-up fraction to $f_{\mathrm{pu}} \leq 10^{-6}$ which would require the allowed external background level to be smaller than 10^{-6} counts/eV/det/day.

Another key property of the detector technology, used for the calorimetric measurement of the ^{163}Ho spectrum, is the availability of a reliable calibration function which allows for the precise definition of the energy scale. Uncertainties in the calibration function result in uncertainties in the position of the endpoint of the spectrum which will then increase the systematic errors. For X-ray measurements, MMCs have demonstrated a stable and reliable calibration function with an unmatched small non-linearity of less than 1 % for X-ray energies up to about 10 keV, which can be well described by the thermodynamical properties of the detector [51]. This point will be discussed in more detail in Section 4.1.

Figure 5 shows the achievable sensitivity of the electron neutrino mass at 90% C.L. as a function of the total number of counts in the spectrum. The dark-blue curve is calculated for $Q_{\mathrm{EC}} = 2.833\,\mathrm{keV}$ [23] while the two light-grey curves define the region of the achievable sensitivity in case of Q_{EC} between $2.7\,\mathrm{keV}$ and $2.9\,\mathrm{keV}$. The calculations are performed using an unresolved pile-up fraction and an energy resolution that are conservatively chosen to be $f_{\mathrm{pu}} = 10^{-6}$ and $\Delta E_{\mathrm{FWHM}} = 3\,\mathrm{eV}$. Given the state of the MMC development and the potential for further improvements, it appears likely that these numbers will be reduced in the ECHo-1M experiment.

As already mentioned, the ECHo experiment will be divided into several phases. The first phase, ECHo-1k, is presently ongoing and will last until 2018. Detail on ECHo-1k will be given in the following Sections and summarized in Section 11.1. This experiment is characterized by the use of a ^{163}Ho activity of 1 kBq which will be divided into about 100 single detectors. The total number of events of the order of 10^{10} which will be measured in ECHo-1k will allow for a limit on the electron neutrino mass smaller than $10\,\text{eV}/c^2$. The second phase, ECHo-1M, is under study and will start at the end of ECHo-1k. ECHo-1M, as the name says, will be characterized by a ^{163}Ho activity of 1 MBq. More details on this second phase of the ECHo experiment are described in Section 11.2. A total number of events in the full spectrum of the order of 10^{14} is expected to be acquired in the ECHo-1M experiment. The analysis of such a high statistics spectrum will allow to reach a sensitivity on the electron neutrino mass below $1\,\text{eV}/c^2$.

3.3 Other uncertainties influencing the neutrino mass sensitivity

The value of the energy available to the ^{163}Ho decay, Q_{EC}, strongly influences the sensitivity that can be reached. The recent direct and high-precision measurement of the mass difference of ^{163}Ho and ^{163}Dy has remarkably reduced the indetermination of Q_{EC}, as discussed in Section 2. This allows for a precise design of the experiment by knowing which fraction of events is expected in the region of interest, given Q_{EC}. Nevertheless a further reduction of the uncertainties on Q_{EC} to about $1\,\text{eV}$ is required to reduce systematic errors in the analysis of the ^{163}Ho spectrum to achieve sub-eV neutrino mass sensitivity. In Section 9 the method used for the current best direct determination of the ^{163}Ho Q_{EC} will be discussed as well as the prospects for a direct measurement reaching the required level of precision of about $1\,\text{eV}$.

The sensitivity plot shown in Figure 5 has been obtained by considering only first order transitions in the decay of ^{163}Ho and no uncertainties in the parameters describing the related spectral shape. Adding uncertainties in these parameters induces slightly larger uncertainties in the evaluation of the sensitivity to neutrino mass, in particular in the case of the description of the line MI. More important is the present lack of a precise description of the structures which appear in the spectrum in case of higher order excitations in ^{163}Dy. To reduce the uncertainties in the parameters describing the shape of the structures in the ^{163}Ho spectrum related to higher order excitations, not only an experimental characterization, which can be obtained by high statistics and high resolution calorimetrically measured spectra, but also a solid theoretical model able to describe even the smallest structures at the endpoint region of the spectrum needs to be developed. A complete description of the theoretical methods used to investigate the spectral shape of the electron capture process in ^{163}Ho and the current results are described in Section 10.

4 Detector technology used for ECHo

For the reasons already mentioned in Section 3.2, ECHo has chosen MMCs as detector technology. MMCs are thermal equilibrium detectors that are operated as cryogenic microcalorimeters. In a simplified picture, cryogenic calorimeters consist of an energy absorber having a heat capacity C that is connected via a weak thermal link to a thermal bath kept at constant temperature T. The weak thermal link is characterized by its thermal conductance G. The absorption of a particle of energy E in the absorber results in an increase of its temperature given by $\Delta T \simeq E/C$. The energy deposited in the absorber will then flow to the thermal bath with a time constant $\tau = C/G$ and the detector will cool to the initial temperature. To give the order of magnitude
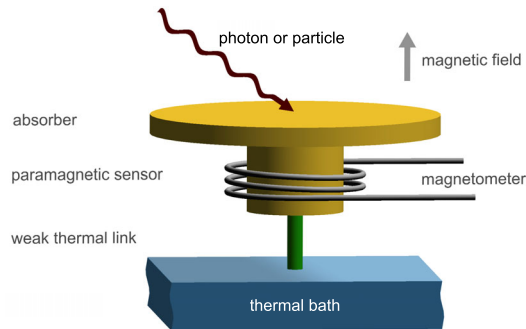
Fig. 6. Schematic illustration of a metallic magnetic calorimeter. Figure reproduced from [178]. (This figure is subject to copyright protection and is not covered by a Creative Commons license.)

for a typical temperature rise, 10 keV absorbed in a detector having a heat capacity of 1 pJ/K leads to an increase of temperature of about 1 mK. This small change of temperature can be measured with high precision only by very sensitive thermometers which are the heart of the microcalorimeters.

Different solutions are applied for transducing the temperature change resulting from the absorbed energy into a voltage pulse. The state-of-the-art of temperature transducers for low temperature microcalorimeters is summarized in [52,53]. Presently, the best performances in terms of energy resolution achieved by cryogenic detectors developed for soft X-ray spectroscopy is obtained by MMCs and Transition Edge Sensors (TESs)[54]. Both detectors have reached an energy resolution of $\Delta E_{\mathrm{FWHM}} = 1.6$ eV [51,55], which is presently the record in terms of energy resolution achieved by any energy dispersive detector for X-ray spectroscopy at the benchmark energy of 6 keV. In the following we will describe the function and performance of MMC based detectors for soft X-ray spectroscopy which is the relevant energy scale for ECHo. In addition, we will discuss MMC prototype detectors used to obtain high resolution ^{163}Ho spectra.

4.1 Function and performance of MMC detectors

MMCs use as temperature sensor a metallic paramagnetic material located in a constant weak magnetic field [47,48]. The magnetization of the sensor has a strong dependency on temperature, following roughly a Curie law $M \propto T^{-1}$. Figure 6 shows a schematic picture of a MMC detector with particle absorber and paramagnetic sensor connected to a thermal bath via a weak thermal link. The change of the detector temperature, upon the interaction with a particle in the absorber leads to a change of magnetization of the paramagnetic sensor and, in turn, to a change of flux $\Delta\Phi$ in a pick-up coil:

$$\Delta\Phi \propto \frac{\partial M}{\partial T}\Delta T \simeq \frac{\partial M}{\partial T}\frac{E}{C} = \frac{\partial M}{\partial T}\frac{E}{C_{\mathrm{a}} + C_{\mathrm{s}}}. \tag{2}$$

Here, the total heat capacity C of the detector is the sum of the heat capacity C_{a} and C_{s} of the absorber and the sensor, respectively. As we will discuss in more detail in Section 6, the change of magnetic flux $\Delta\Phi$ is typically read out by an inductively matched low-noise dc-SQUID transducing a change of magnetic flux into a voltage signal.

The presently mostly used sensor material is a dilute alloy of erbium in gold, **Au**:Er, with an erbium concentration between about 200 ppm, for detectors developed for soft X-rays spectroscopy, and about 800 ppm, for detectors developed for hard
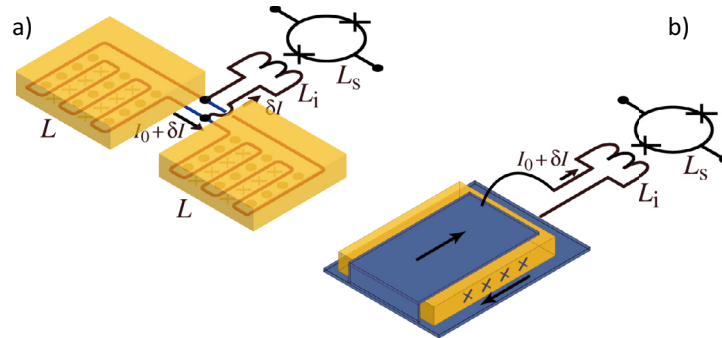
Fig. 7. Schematic illustration of two different MMC geometries. (a) MMC with two planar meander-shaped gradiometric pick-up coils. (b) MMC with one planar meander shaped pick-up coil, where the paramagnetic material is sandwiched between two superconducting layers [48].

X-rays spectroscopy. The typical absorber material is gold due to its chemical stability and high stopping power for X-rays, but also other materials have been used for special applications [56]. The electro-thermal behavior of MMCs can be confidently calculated by standard statistical physics. This allows for designing detectors with optimized properties for a large variety of applications [57].

There are many possible ways to design the pick-up coils for the flux coupling to the readout SQUID. Figure 7 shows the two geometries which presently are most commonly used, the so called meander-shape geometry and the sandwich geometry. Both of these design are based on planar temperature sensor to make possible the microfabrication of large and dense-packed arrays [49]. Scheme (a) is based on two planar meander-shaped pickup-coils, each having inductance L connected in parallel to the input coil of the front-end SQUID, with inductance L_i. The front-end SQUID is a current-sensor dc-SQUID with inductance L_S. Each meander is covered with a planar paramagnetic sensor. The necessary bias field for the sensor is produced by a persistent current of some tens of mA in the circuit formed by the two meanders. The bias-field as well as the magnetic response of the sensor is a multipole field of high order, reducing magnetic cross-talk between neighboring pixels. The planar superconducting pick-up coils are covered or "filled" with a few μm thick **Au**:Er film. For obvious reasons in this geometry the filling factor of the coil can reach maximally $F = 0.5$. In practice for numerically optimized meander-based detectors we find $F \simeq 0.4$, where the **Au**:Er thickness equals about one third of the meander pitch. In scheme (b) the sensor material is sandwiched between two superconducting stripes of the pick-up coil, which carries a persistent current in opposite direction to produce a nearly homogeneous bias field in the sensor volume. With this geometry a higher filling factor of $F \simeq 0.8$ is reached. All MMCs presently studied in Heidelberg are fabricated on 3 inch sapphire or thermally oxidized Si wafers. The microfabrication of MMCs is performed through a number of well-established processes which lead to a yield of about 99 %. Further details on different design concepts as well as on microfabrication techniques can be found in [48].

The typical energy resolution of fully micro-fabricated MMCs developed for soft X-rays, having a quantum efficiency of about 99 % at 6 keV, is $\Delta E_{\text{FWHM}} \leq 2$ eV [51]. The intrinsic pulse rise-time of such a MMC detector is $\tau_r \simeq 90$ ns which is determined by the strength of the electron-spin coupling [58]. Figure 8a shows the measurement of the K_α lines from an external ^{55}Fe calibration source taken by a MMC detector optimized for soft X-rays. The spectral shape is perfectly described by the natural line shape, as determined with crystal spectrometers [59], and the instrumental resolution
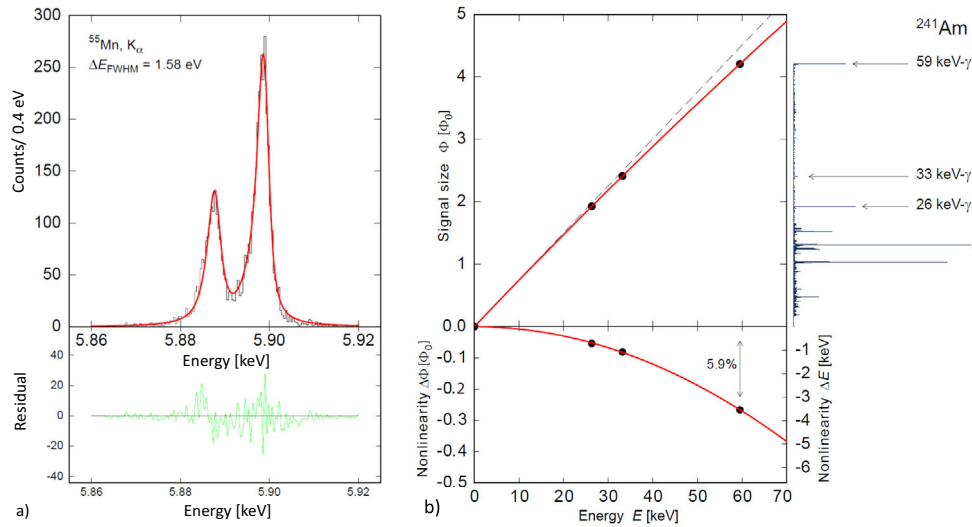
Fig. 8. (Left) The upper part of the plot shows the K_α lines from an external ^{55}Fe calibration source acquired with a MMC (histogram), the red line indicates the natural line shape convolved with a Gaussian taking into account the instrumental resolution of $\Delta E_{\text{FWHM}} = 1.6\,\text{eV}$. The lower part of the plot shows the difference between fit and data. (Right) The upper part of the plot shows a typical calibration function for MMCs, indicated by the red solid line in a plane where on the y-axis the signal sizes measured as magnetic flux coupled to the front-end SQUID and on the x-axis the expected energy are shown. The points in the plot indicate the experimental values related to events stemming from three different nuclear transitions of a ^{241}Am source. The corresponding energy spectrum is plotted at the right margin. For comparison the dashed line displays a linear dependence expected for an ideal detector. The lower part of the plot shows the difference between the expected ideal detector results and the calibration function. The solid line represents a polynomial function of second order.

of the MMC of $\Delta E_{\text{FWHM}} = 1.6\,\text{eV}$. The difference between fit and data is depicted in the bottom part of the figure.

The linearity of this detector has been investigated for energies up to 60 keV using an ^{241}Am source [51]. The corresponding results are shown in Figure 8b where only the sharp gamma lines of this source were considered. For comparison the ^{241}Am spectrum is shown on the left side of the calibration plot. The relative non-linearity $\Delta\Phi/\Phi$ at 6 keV is about 0.6 % while at 60 keV it is about 6 %. The energy calibration function is in very good approximation a polynomial of second order which is well understood by the thermodynamical properties of the involved materials. The energy calibration for spectra acquired with MMCs can therefore be defined with high precision and will, at a fixed base temperature, not vary over time.

4.2 MMCs with embedded ^{163}Ho

To perform a calorimetric total activity measurement with MMCs, the nuclide of interest needs to be surrounded by enough absorber material so that the stopping power for the emitted particles, electrons and photons is 100 %. A possibility to reach this goal is to perform an ion-implantation of the interesting nuclides directly into the active part of the detectors.
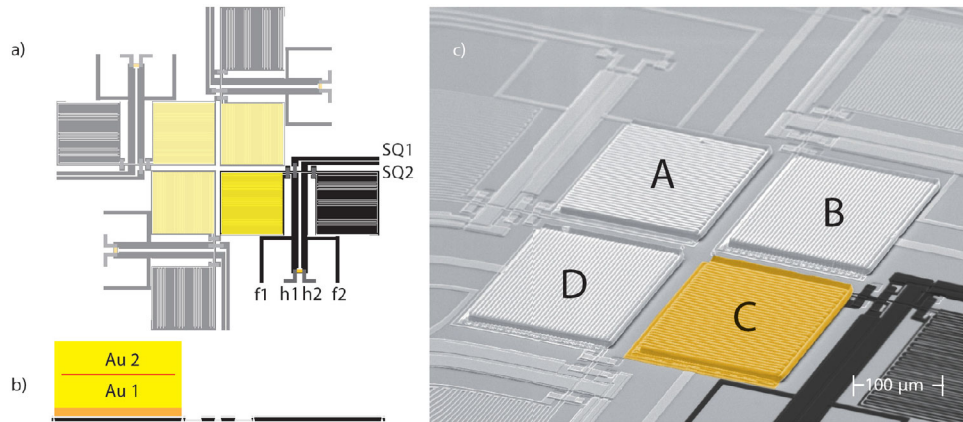
Fig. 9. Schematic illustration and SEM picture of the MMC detector chip used for ^{163}Ho implantation in 2009. (a) Layout of the four double-meander pickup coils, (b) schematic of the absorber cross-section, and (c) SEM picture of the central part of the fully micro-fabricated MMC with the four pixels (A, B, C and D) prepared to be irradiated. Figure reproduced from [32]. (This figure is subject to copyright protection and is not covered by a Creative Commons license.)

A first prototype of a MMC detector (MMC-ECHo-0) suited for ^{163}Ho implantation was designed and fabricated using the clean room facilities at the Kirchhoff Institute for Physics of Heidelberg University. The ion implantation was performed at ISOLDE-CERN [60] in 2009. The ^{163}Ho ions were produced using a spallation process where a high-energy proton beam (1.4 GeV) was hitting a Ta target kept at 1800–1900 °C. After ionization of the released atoms a mass selected beam with particles having mass number $A = 163$ was accelerated at 30 keV and collimated onto the surface of the detector chip. Figure 9a shows a schematic of the first detector chip developed for the ion-implantation test, which is equipped with four detectors positioned close to each other so that the implantation could be performed in each of them at the same time. The detector design is based on the niobium double-meander pick-up coil geometry that is depicted in Figure 7a. The leads used to inject the persistent current in the pick-up coils are labeled with f1 and f2. With the help of an on-chip persistent current switch, a current I_0 is injected. In order to heat up the switch, a current of a few mA runs through the resistive AuPd film heater switch via the contacts labeled with h1 and h2. Finally, the leads connecting the double-meander structure to the input coil of the dc-SQUID are labeled SQ1 and SQ2. Only one of the two wings of the meander-shaped pick-up coil is equipped with **Au**:Er sensor and Au absorber for a better characterization of the performance. The erbium concentration of about 210 ppm and the geometry of the sensor are optimized to reach high energy resolution when combined with a gold absorber having the dimension of $190 \times 190 \times 10 \, \mu m^3$.

Figure 9b shows the cross-section of one of the detectors. A red line between the two parts of the gold absorber, Au 1 and Au 2, indicates the position of the implanted ions. To obtain this 4π-geometry, the ions are implanted after the production of the first half of the absorber, Au 1, consisting of a 5 μm thick gold film, over an area of $160 \times 160 \, \mu m^2$. The second part of the absorber, Au 2, again a 5 μm thick gold film, is structured in a following step over the full absorber area, $190 \times 190 \, \mu m^2$. The detector was designed to achieve an energy resolution at $\Delta E_{\mathrm{FWHM}} = 4 \, eV$ at 30 mK under ideal conditions.

Figure 9c shows a Scanning Electron Microscope (SEM) picture of the central part of the detector chip. At this point the absorber was processed only until the first gold layer and the microfabrication prior implantation was completed. For the actual implantation process the detector chip was glued onto a glass support and covered with a protective layer of photoresist. Subsequently, four squared openings with an area of $160 \times 160 \, \mu m^2$ centered on top of each of the four absorbers were structured into the photoresist film to enable the implantation. After the ion-implantation at ISOLDE-CERN and an initial cooling time of about two months, the chip was covered with about 100 nm of gold before removing the photoresist. After that, a second (thick) photoresist layer was spinned over the entire chip and four holes, each with the same surface as the first gold absorbers Au 1 were structured. Finally the second part of the absorber Au 2, a gold layer 5 μm thick was deposited and the photo resist was removed. A detailed description of the detector design and of the ion-implantation process can be found in [32].

This first prototype of a MMC detector with implanted ^{163}Ho has been characterized in detail and its performance will be described in Section 5. Since 2009 the MMC detector technology for soft X-ray has advanced in many ways. One aspect that has been improved for the second generation of ECHo detectors is a design that allows for minimizing the loss of athermal phonons into the substrate. These hot phonons are generated in the initial phase of the thermalization process [61], after a particle has interacted in the absorber, and have a small but finite probability to escape to the substrate before thermalizing in the absorber. This unwanted effect can be reduced by minimizing the contact area between the gold absorber and the **Au**:Er sensor. Such a MMC detector design has been successfully developed and it was used to prepare a 1×16 array based on the maXs-20 sandwich design [49] for a second ^{163}Ho ion-implantation (MMC-ECHo-1). The implantation onto the MMC-ECHo-1 detector array was performed at ISOLDE-CERN in an off-line process using a chemically purified ^{163}Ho source. Details on the source production will be given in Section 7.

5 Performance of MMCs with embedded ^{163}Ho

Both MMC detector chips, which have been mentioned in the previous section, have been characterized in several measurement campaigns. After the first ion implantation and completion of the absorbers in 2009, the first prototype detector chip MMC-ECHo-0 has been investigated using different experimental setups. A full account of the results obtained in these experiments has been reported in [22,32,62]. Here we summarize the relevant results that will guide the further optimization of MMC detectors for the ECHo experiment.

The detector response has been characterized, as well as the performance, in terms of energy resolution and time profile of the signals. A double stage SQUID circuit [63] has been used for the read out of the detector. More details about the readout of MMCs will be given in Section 6. Figure 10 (left) shows a histogram corresponding to the $K_{\alpha1}$ and $K_{\alpha2}$ lines acquired using an external ^{55}Fe calibration source at an operating temperature of 30 mK. The red curve represents a fit obtained by the convolution of the expected intrinsic line shapes and a Gaussian detector response with $\Delta E_{FWHM} = 7.6$ eV [33]. The slight degradation of the instrumental resolution with respect to the expected value is caused mainly by an insufficient stabilization of the base temperature of the cryostat.

Figure 10 (right) shows the first 3 μs of two different pulses originating from the decay of ^{163}Ho and corresponding to the $3s$ and $4s$ capture respectively. A rise-time of about $\tau_r = 130$ ns was extracted by fitting the pulses in this time interval to an exponential function. The non-linear contribution of the second order polynomial
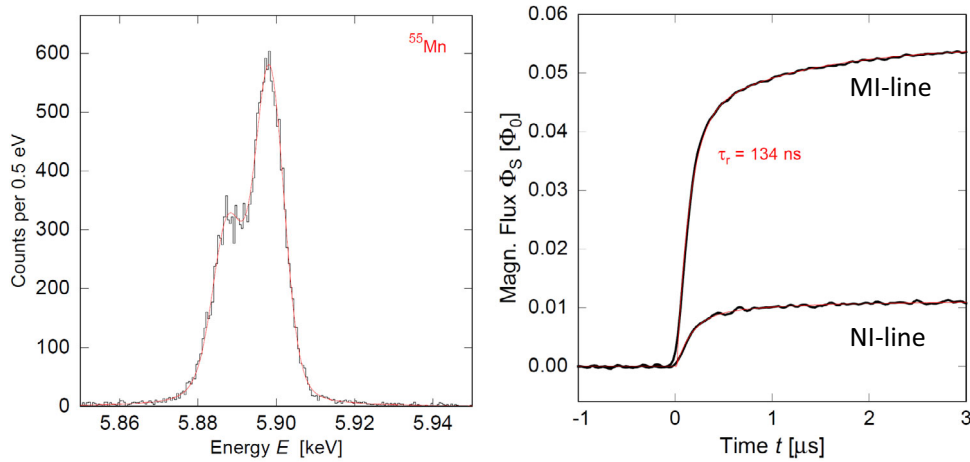
Fig. 10. (Left) Histogram corresponding to the $K_{\alpha1}$ and $K_{\alpha2}$ lines acquired with the MMC-ECHo-0 prototype detector with implanted ^{163}Ho using an external ^{55}Fe calibration source. The solid red line represents a fit based on the convolution of the natural line widths of the two lines and a Gaussian detector response with $\Delta E_{\mathrm{FWHM}} = 7.6\,\mathrm{eV}$ [33]. (Right) Signal shape in the first $3\,\mu s$ of two different pulses corresponding to events due to the capture of a $3s$ electron (MI line) and $4s$ electron (NI line), respectively. The solid red lines correspond to exponential functions of the signal rise with a rise time of $\tau = 134\,\mathrm{ns}$ [33].

calibration function at $6\,\mathrm{keV}$ is about $0.8\,\%$, as expected from the thermodynamical properties. While the rise-time and the well understood calibration function are already suitable for the ECHo experiment, further improvements of the energy resolution for detectors with embedded ^{163}Ho are necessary to meet the requirements which allow to reach sub-eV sensitivity on the neutrino mass. These improvements go along with an optimization of the detector geometry, to reduce unnecessary heat capacity, an improved stabilization and a lowering of the working temperature of the detector.

Figure 11 (left) shows a histogram corresponding to the M lines superimposed with a curve obtained by convolving the intrinsic line shapes with the Gaussian detector response having $\Delta E_{\mathrm{FWHM}} = 8\,\mathrm{eV}$. Obviously, the measured spectral shape is different from the theoretical prediction. At the low energy side of both peaks, a significant broadening is visible. These low energy tails are caused by events for which a fraction of the total energy escapes from the absorber, in form of athermal phonons, into the substrate before complete thermalization within the absorber is reached. As pointed out before, this effect can be reduced by minimizing the contact area between absorber and sensor. In the detector design used for the second implantation (MMC-ECHo-1) performed within ECHo-1k, such a reduced contact area is realized by using just five thin gold stems to connect sensor and absorber [64]. The resulting improvement in the shape of the M lines can be seen in Figure 11 (right). Evidently, the loss of athermal phonons is greatly reduced and no significant asymmetric broadening is observed. Note that the Gaussian detector response is $\Delta E_{\mathrm{FWHM}} = 12\,\mathrm{eV}$ in this case due to a slightly higher operation temperature.

The activity per pixel in the first two detector prototypes was rather small, about $0.02\,\mathrm{Bq}$ for MMC-ECHo-0 and about $0.1\,\mathrm{Bq}$ for MMC-ECHo-1 compared to the presently targeted design value of the ECHo experiment of a few tens of Bq. Ways to increase the activity in future detectors are related to the optimization of the physical separation of the ^{163}Ho ions from the rest of the source materials, namely the
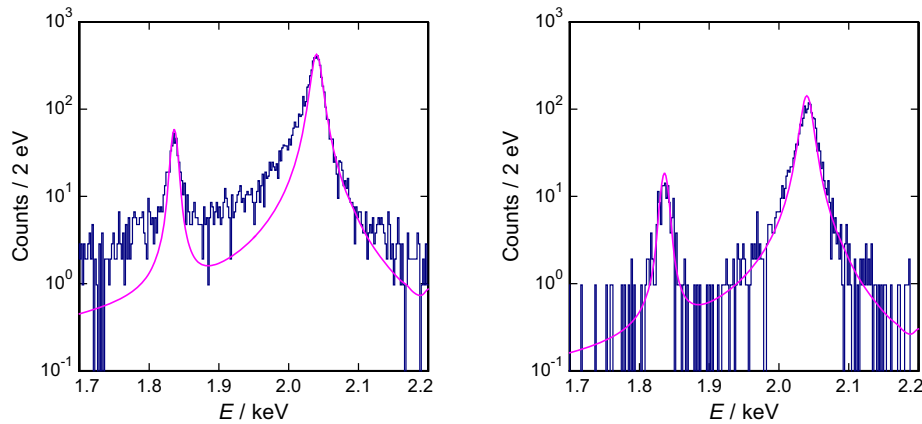
Fig. 11. Histogram of the ^{163}Ho spectrum in the energy range between 1.7 and 2.2 keV as acquired with MMC-ECHo-0 [62] (left) and MMC-ECHo-1 [64] (right) showing the M I and M II lines together with the superimposed curve obtained by the convolution of the natural line shape and a Gaussian detector response (solid magenta line).

development of a high efficiency ion source and the creation of a pure mass selected beam at the mass separator facilities. These aspects will be discussed in Section 7.

The optimal activity is still a matter of investigation. Not only the allowed unresolved pile-up fraction is limiting the maximum activity per detector, but also the fact that the heat capacity contribution of the Ho ions embedded in the absorber could be not negligible with respect to the heat capacity of the other thermodynamical systems of the detector. Therefore the number of allowed Ho ions in the detector will be selected in a way that the corresponding heat capacity does not degrade the signal to noise ratio of the detector. First investigations about the effect of ^{163}Ho ions enclosed in gold thin films have recently been performed within the HOLMES collaboration [65]. According to the authors, for all studied samples, the contribution due to the heat capacity of the holmium atoms was below the detectable limit.

In order to prove this somehow unexpected result, within the first phase of ECHo, ECHo-1k, we have started a series of measurements in which ^{165}Ho, the naturally occurring holmium isotope, has been implanted in MMC absorbers at the RISIKO facility at Mainz University (the facility will be introduced in Sect. 7.4), following the procedures developed for ^{163}Ho ions. The isotope ^{165}Ho has the same nuclear spin and angular momentum, $I = 7/2$ and $J = 15/2$, respectively, as ^{163}Ho and may serve as a model system for ^{163}Ho. The knowledge of the heat capacity contribution per ion will be one of the main ingredients to define the optimal activity per pixel.

5.1 ^{163}Ho spectra obtained with MMC prototype detectors

Let us now turn to the ^{163}Ho spectra obtained with the two different prototype detectors. Figure 12 (left) shows the ^{163}Ho spectrum as measured with the MMC-ECHo-0 prototype detector plotted on a logarithmic y-scale over an energy range up to 2.5 keV. Besides the structures related to the electron capture in ^{163}Ho, also other clear peaks are present around 1.4 keV. These peaks are related to the electron capture in ^{144}Pm. This nuclide (together with several other radioactive nuclides with shorter halflife) has been implanted as ionized molecule with mass number $A = 163$ (PmF$^+$) [32]. Although the presence of this background has not prevented the characterization of the detector, this relatively large contamination is not acceptable in an experiment
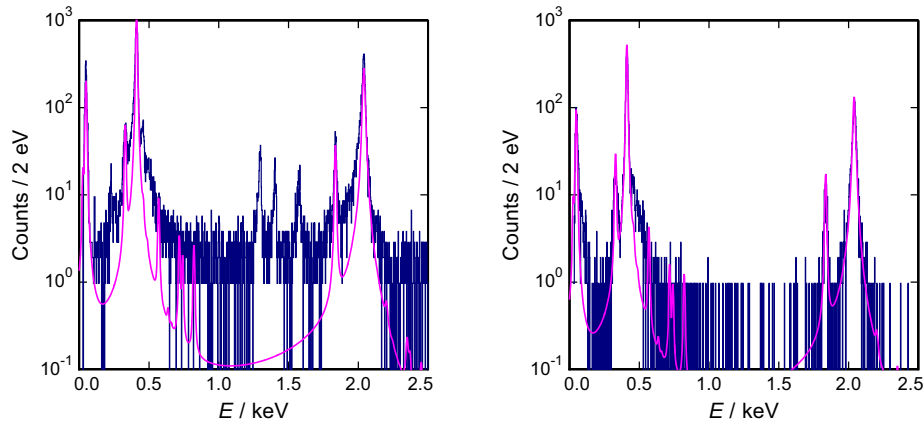
Fig. 12. Histogram of the ^{163}Ho spectrum for energies up to 2.5 keV as acquired by the prototype detectors MMC-ECHo-0 [62] (left) and MMC-ECHo-1 [64] (right). The solid magenta line in both plots represents a fit obtained by the convolution of the natural line shape, with the parameters given in [38], and a Gaussian detector response.

aiming to reach sub-eV sensitivity on the electron neutrino mass. Because of that the ECHo collaboration has developed dedicated processes which ensure the production of large amounts of high purity ^{163}Ho (see Sect. 7). A fraction of one of such sources has already been used for an offline ^{163}Ho implantation at ISOLDE [64]. A preliminary measurement of the ^{163}Ho spectrum obtained by measuring just one pixel for about two days is shown in Figure 12 (right). As expected, it does not show any evidence of the presence of radioactive nuclides other than ^{163}Ho, indicating that any strong radioactive contamination in the implantation beam can be ruled out.

With the first detector prototypes containing implanted ^{163}Ho, the presently most precise ^{163}Ho spectra have been obtained. We have measured five lines of the ^{163}Ho EC spectrum and characterized their peak energies and intrinsic widths. Note that the good energy resolution of these detectors allowed for the first time, using the first detector prototype MMC-ECHo-0, to trigger events corresponding to the capture of $5s$ electrons in ^{163}Ho leading to the first calorimetric measurement of the OI line [62]. Table 1 summarizes the experimental values for the peak energies and intrinsic widths for all five capture lines. The measured peak energies are shifted, as expected, towards slightly lower values with respect to the corresponding binding energies of the dysprosium atom due to the presence of the additional $4f$ electron. The de-excitation energy of ^{163}Dy after the electron capture in ^{163}Ho is in first approximation given by the difference between the binding energy of the captured electron and the binding energy of the $4f$ electron. The linewidths, besides the one of the NII line, agree well with literature values. The reason why the measured width of the NII line, $\Gamma_{\mathrm{H}}^{\mathrm{exp}} = 13\,\mathrm{eV}$, is so different from the expected one, $\Gamma_{\mathrm{H}}^{\mathrm{lit}} = 5.3\,\mathrm{eV}$, is still a matter of investigation within ECHo-1k both from the experimental point of view as well as from theoretical models.

From the analysis of the spectrum, in particular by comparing the amplitude of the lines with the expected ones it is possible to extract the value of the energy available to the decay, Q_{EC}. We have performed the analysis using the parameters reported in [41] for the case of massless neutrinos. The value we obtain is $Q_{\mathrm{EC}} = (2.858 \pm 0.010_{\mathrm{stat}} \pm 0.05_{\mathrm{syst}})\,\mathrm{keV}$. A detailed description of this analysis can be found in [62]. The systematic error is dominated by the uncertainties on the capture probabilities, as given by different theoretical calculation [41,66], which can be estimated to be 5%.
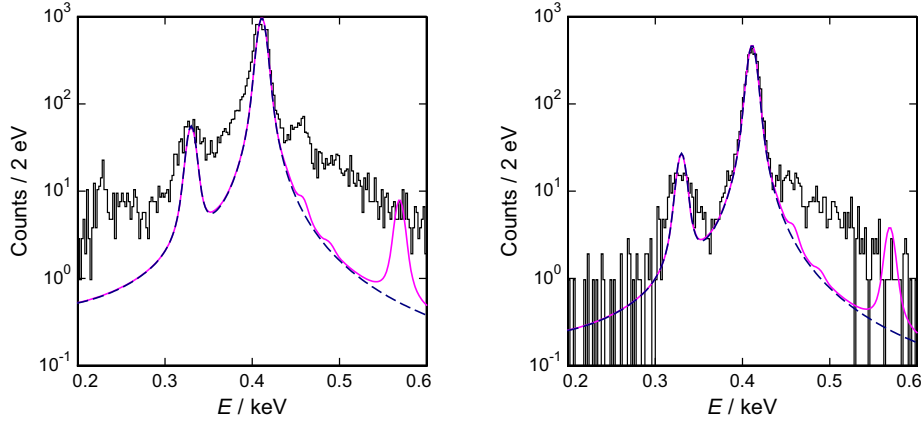
Fig. 13. Histogram of the ^{163}Ho spectrum in the energy range between 0.2 and 0.6 keV as acquired with MMC-Echo-0 [62] (left) and MMC-Echo-1 [64] (right) showing the NI and NII lines together with a fit (dashed blue line) obtained by considering only first order processes and a Gaussian detector response having FWHM = 8 eV. The solid magenta line corresponds to the convolution of a theoretical spectrum including second order processes as discussed in [38] and a Gaussian detector response having FWHM = 8 eV.

The Q_{EC}-value obtained by the analysis of the calorimetrically measured spectrum agrees very well with the one obtained as difference between the ^{163}Ho and the ^{163}Dy atomic masses [23]. The reduction of the systematic error is one of the aims of the ECHo-1k phase.

5.2 Evidence for the contribution of higher order processes

Figure 13 (left) shows the ^{163}Ho spectrum in the energy region around the NI and NII lines as obtained with the first detector prototype MMC-ECHo-0. The dark blue dashed line is a curve calculated considering only first order transitions and assuming the natural line shape convolved with a Gaussian detector response of $\Delta E_{FWHM} = 8$ eV. While the low-energy tail of the NI line, as discussed before, can be explained by the loss of athermal phonons for this detector type, the large excess of counts on the high-energy side of the NI line must have other reasons. Figure 13 (right) shows the histogram of the ^{163}Ho spectrum in the same energy range as acquired using one pixel from the new implanted MMC array MMC-ECHo-1 in which the ^{163}Ho ions were produced and purified according to the procedures discussed in Section 7. By comparing the two histograms in Figure 13 (left) and (right) it is evident that the excess of counts above the NI line does not depend on either the particular detector type nor on the contamination present in the source. Therefore one has to conclude that the additional counts at the high-energy side of the NI line are most likely intrinsic to the ^{163}Ho spectrum and not an experimental artifact. This observation has already triggered several theoretical investigations [24,37–40] in which higher order excited states in the daughter dysprosium atoms are considered to describe the spectrum. The idea is that at the moment of the capture of the electron in the Ho atom, another hole (or several other holes) is created in the electronic shells due to the promotion of the corresponding electron to an upper shell or to the continuum, referred to as shake-up and shake-off processes, respectively. These processes give rise to additional peaks or, as pointed out in [39,40], in case of shake-off processes to continuous structures.
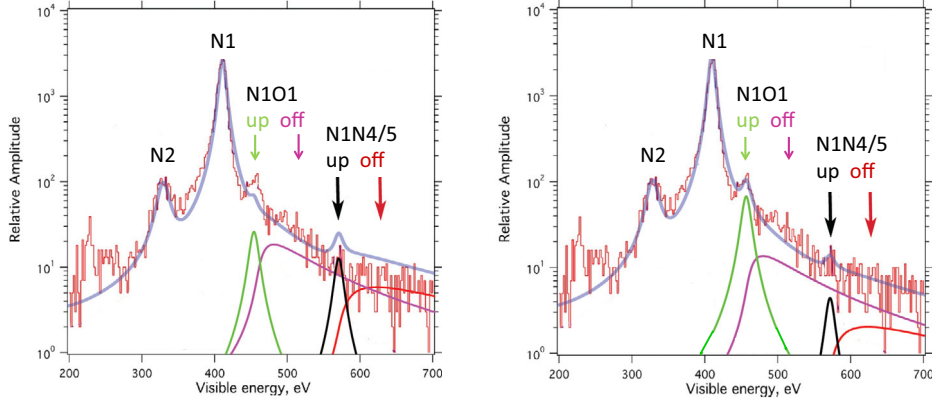
Fig. 14. Histogram of the ^{163}Ho spectrum acquired with the first detector prototype as in [32] in the energy range between 0.2 keV and 0.7 keV compared to a fit obtained by the convolution of the expected spectrum according to [39] and a Gaussian detector response with $\Delta E_{\mathrm{FWHM}} = 8.4$ eV. (Left) The theoretical model for the ^{163}Ho spectrum includes shake-up and shake-off transitions for the N1O1 and N1N4/5 excitations calculated using the simplified model described in [39]. (Right) The theoretical model for the ^{163}Ho spectrum includes shake-up and shake-off transitions for the N1O1 and N1N4/5 excitations with a free amplitude to fit the data [39].

In both plots shown in Figure 13 the solid magenta line represents the convolution between the theoretical ^{163}Ho spectrum, including second order shake-up excitations where two holes are present in the excited ^{163}Dy atom, calculated using the parameters given in [38], and a Gaussian detector response. The difference between the first order and second order description is clearly visible on the high-energy side of the NI line. It is also evident, that the theoretical description in this form, while predicting new structures in the spectrum at the energy where the excess of events is seen, is not able to fit the experimental data satisfactorily.

A better description of the measured spectrum is possible, as discussed in [39,40], by considering that, in case of shake-off processes, the electron can be promoted to the continuum having a finite kinetic energy. In fact during the electron capture, when one electron from the shell H' is shaken-off to the continuum, the process can be described as:

$$^{163}\mathrm{Ho} \rightarrow {}^{163}\mathrm{Dy}[\mathrm{H}, \mathrm{H}'] + e^- + \nu_{\mathrm{e}}. \tag{3}$$
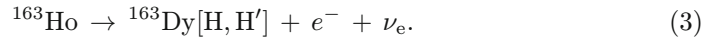
This is a typical three bodies decay process and therefore both the electron and the neutrino have a continuous energy spectrum which fulfils:

$$E_\nu + T_{\mathrm{e}} = Q_{\mathrm{EC}} - E_{\mathrm{H}} - E_{\mathrm{H}'}. \tag{4}$$

In a calorimetric measurement all the energy released in the EC process, besides the one taken away by the electron neutrino is measured. In this case the measured energy can then be written as:

$$E_{\mathrm{c}} = T_{\mathrm{e}} + E_{\mathrm{H}} + E_{\mathrm{H}'}. \tag{5}$$

A first attempt to give a theoretical prediction of the spectrum including the continuum structures of shake-off electrons has been described in [39]. Figure 14 (left) shows a reproduction of Figure 3 showed in [39]. The theoretical model used for the fit includes the excited states with two holes corresponding to the 4s and 5s electron for both shake-up and shake-off processes and with two holes corresponding to the 4s

and $4d$ ($3/2$ and $5/2$) electrons for both shake-up and shake-off processes. The fit is done on the data described in [22] which have been obtained using the detector MMC-ECHo-0. The agreement is still not perfect, but the model seems to better describe the general shape of the measured spectrum. In particular, Figure 14 (right) shows that if one allows more freedom for the amplitude of each transition, the agreement between data and fit in the energy range between 200 eV and 700 eV is astonishing (the excess of counts between 200 eV and 300 eV are due to the EC in ^{144}Pm, see Sect. 5.1). Unfortunately the statistics in the present spectra is too poor to allow for a more fine investigation of these structures.

Spectra with much higher statistics as well as further refinements of the theoretical description are among of foci of the first phase of ECHo experiment, ECHo-1k, with the aim to fully clarify the role of higher order excited states on the ^{163}Ho spectrum.

6 Readout technology used for ECHo

Superconducting quantum interference devices (SQUIDs) are sensitive superconducting electronics devices converting a change of magnetic flux into a voltage or current signal [67]. They provide very large system bandwidth, quantum limited noise performance and are intrinsically compatible with operation temperatures well below 1 K. SQUIDs are therefore very well suited for the readout of MMCs. Typically, the input coil of a current-sensing SQUID is connected to the pickup coil of an MMC to form a superconducting flux transformer transducing the magnetization change of the temperature sensor into a change of magnetic flux threading the SQUID loop [47,68]. In this case, a magnetic flux change $\delta\Phi$ in the pickup coil with inductance L (see Fig. 7) causes a magnetic flux change $\delta\Phi_s$ in the SQUID:

$$\delta\Phi_s = \frac{k\sqrt{L_s L_i}}{L_i + L_w + L}\delta\Phi. \tag{6}$$

Here L_s denotes the SQUID inductance, L_i the inductance of the input coil, k the magnetic coupling factor between the SQUID and its input coil, and L_w is the sum of all parasitic inductances within the flux transformer.

6.1 Single-channel readout of metallic magnetic calorimeters

To achieve very good noise performance as well as to ensure that the system bandwidth is large enough to retain the fast signal rise time of MMCs, both properties that are essential for the ECHo experiment (see Sect. 3.2), two dc-SQUIDs are very often arranged in a two-stage SQUID setup [69]. As depicted in Figure 15, the detector is connected to the first-stage SQUID (SQ1) that is located in direct vicinity of the detector and is therefore operated at mK temperatures. SQ1 is usually voltage-biased by injecting a bias current through a bias resistor R_b which is connected in parallel to SQ1 and whose value is smaller than the dynamic SQUID resistance, R_{dyn}. In this configuration, a change of magnetic flux threading the first-stage SQUID loop is converted into an output current change of SQ1. The output current is running through the input coil with inductance L_{amp} of the second-stage SQUID (SQ2), that can be an N-SQUID series array [69], creating magnetic flux inside the SQUID(s) loop. SQ2 is current-biased and can be operated either at the same temperature as the detector and SQ1 or at higher temperatures to minimize the heat load to the cryogenic platform. Using this scheme, the initial flux change in SQ1, $\delta\Phi_1$, is boosted
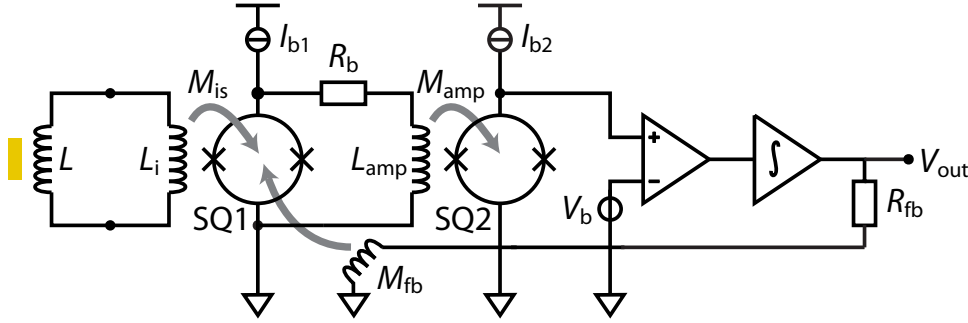
Fig. 15. Schematic of a two-stage SQUID setup consisting of a first-stage SQUID (SQ1) reading out the detector and a subsequent secondary SQUID (SQ2) boosting the output signal of the front-end SQUID. A room-temperature electronics is used to provide negative flux feedback to SQ1. For clarity, the detector is depicted as a yellow box that is coupled to a pickup coil with inductance L.

into flux change $\delta\Phi_2$ threading SQ2, where the small-signal flux gain is given by

$$G_\Phi = \frac{\partial\Phi_2}{\partial\Phi_1} = \frac{M_{\mathrm{amp}}}{M_{\mathrm{dyn}} + R_{\mathrm{g}}/V_\Phi}. \tag{7}$$

Here, M_{amp} denotes the mutual inductance between SQ2 and its input coil, V_Φ is the flux-to-voltage transfer coefficient of SQ1 and $M_{\mathrm{dyn}} = R_{\mathrm{dyn}}/V_\Phi$ is the intrinsic current sensitivity of SQ1. The output voltage of SQ2 is amplified using a low-noise amplifier at room-temperature and fed into a voltage integrator. The output voltage V_{out} of the integrator is, on one hand, the signal to be acquired and, on the other hand, is converted into a feedback current using the feedback resistor R_{fb}. The feedback current runs through a feedback coil that is mutually coupled via M_{fb} to SQ1 to create a negative flux feedback signal compensating the initial flux change in SQ1 in order to have a linear relation between applied flux and output voltage [69].

The implementation of a two-stage SQUID setup requires a first-stage SQUID, an amplifier SQUID, a room-temperature feedback electronics as well as about ten electrical wires that are routed from room-temperature to the SQUID setup. The power load to the cryogenic platform is of the order of some nW [63] and is therefore acceptable for modern dilution refrigerators. However, the readout of large MMC detector arrays as required for the ECHo experiment is hardly possible by simply multiplying the single-channel detector readout since the number of SQUIDs, feedback electronics and electrical wires scales linearly with the number of detectors. This demands the use of a suitable multiplexing technique.

6.2 Multiplexed readout of metallic magnetic calorimeters

Currently, two kinds of multiplexers are being developed for the readout of MMC detector arrays. The first kind operates in the time-domain and is based on low-β_{L} dc-SQUID arrays (where $\beta_{\mathrm{L}} = 2\pi L_{\mathrm{s}} I_{\mathrm{c}}/\Phi_0$ with $\Phi_0 = 2.07 \times 10^{-15}$ Vs being the magnetic flux quantum) acting as flux-actuated superconducting-to-normal-conducting switches [70–72]. This gives the possibility to measure the signals from N detectors with only one physical output channel by interleaving different detector signals in time. For this, each channel is repeatedly turned on and off, one after the other. During the time period, when a channel is switched on, the output signal of the
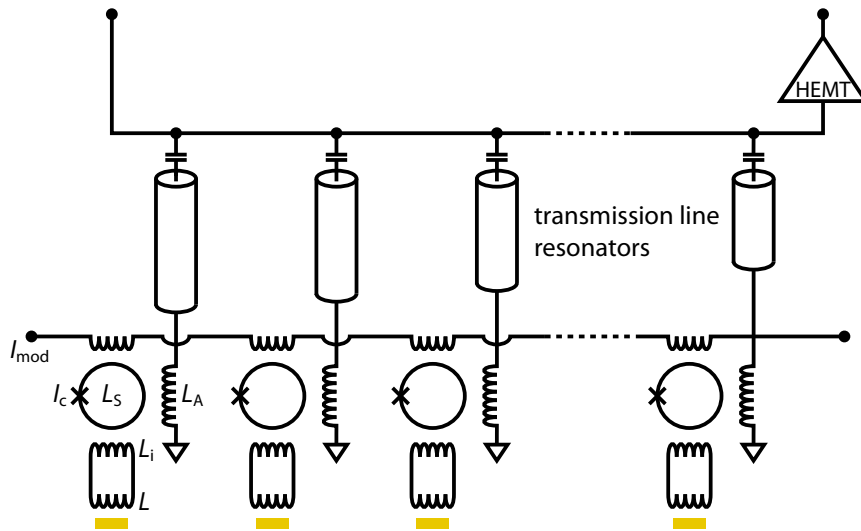
Fig. 16. Schematic circuit diagram of the microwave SQUID multiplexer. For clarity, the detectors are depicted as yellow boxes that are coupled to a coil L and the superconducting $\lambda/4$ GHz transmission line resonators are shown as short coaxial cables.

corresponding detector is sampled. A very basic requirement of this approach is the possibility to switch rapidly between different channels. This requires a high open-loop system bandwidth, f_{ol}, to allow the signals to settle before sampling. At the same time, the bandwidth per pixel f_{pixel} is reduced to $f_{\mathrm{pixel}} = f_{\mathrm{ol}}/N$ due to sequential sampling. Therefore, the Nyquist-Shannon sampling theorem is not fulfilled and wideband noise contributions are aliased. Hence, the overall noise will increase compared to the single-channel detector readout. In addition, the bandwidth per pixel gets smaller with increasing number of pixels such that the fast signal rise time of MMCs cannot be retained anymore.

The second kind of multiplexer is depicted in Figure 16. It is based on the microwave SQUID multiplexer (μMUX) that was originally introduced in the context of the readout of detector arrays based on superconducting transition edge sensors (TESs) [50,73,74]. It relies on the use of non-hysteretic rf-SQUIDs that are inductively coupled to microwave resonators. More precisely, each detector is inductively coupled to a non-hysteretic, un-shunted rf-SQUID consisting of a closed superconducting loop with inductance L_{s} that is interrupted by a Josephson tunnel junction with critical current I_{c}. For $\beta_{\mathrm{L}} < 1$, the SQUID is non-hysteretic and behaves purely reactive. It therefore can be modeled as a non-linear inductor whose value depends on the magnetic flux Φ threading the SQUID loop [75–77]. In this readout scheme, the SQUID is inductively coupled to a load inductor L_{A} terminating a high-quality superconducting $\lambda/4$ GHz transmission line resonator that is capacitively coupled to a transmission line common to each resonator. Since the load inductor is screened by the SQUID, its self-inductance depends on the magnetic flux Φ threading the SQUID loop, thus leading to a magnetic flux dependence of the resonance frequency of the associated resonator. For this reason, the circuit's resonance frequency gets shifted as the detector signal changes. To measure this frequency shift standard homodyne or heterodyne detection techniques are used. Due to the capacitive coupling, many resonators, each having a unique resonance frequency, can be coupled to a common transmission line. This allows for simultaneously measuring hundreds or thousands of detectors by injecting a microwave frequency comb and continuously monitoring the
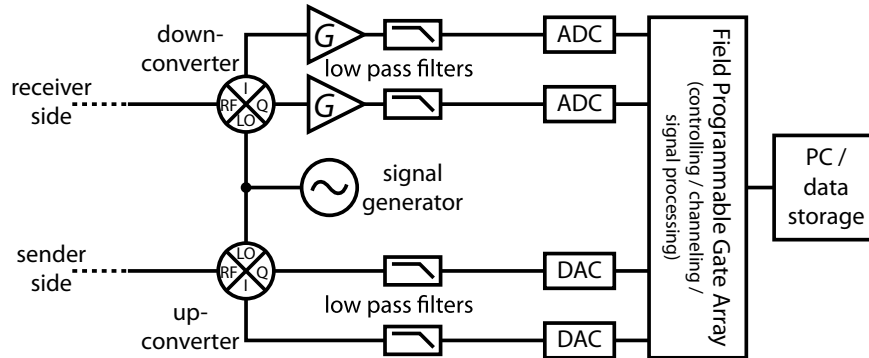
Fig. 17. Schematic of a software defined radio-based digital readout scheme for the operation of a microwave SQUID multiplexer. The meaning of the different devices is explained in the text.

amplitude and phase of each carrier signal. This requires only one cryogenic high electron mobility transistor (HEMT) amplifier and two coaxial cables routed from room temperature to the multiplexer. More precisely, the total number of detectors that can be simultaneously readout depends on the available HEMT amplifier bandwidth, the required signal rise-time, the level of tolerable crosstalk as well as the fabrication accuracy of the multiplexer. In contrast to any time-domain multiplexing technique, the noise performance of an individual readout channel of a μMUX does not depend on the total number of channels being multiplexed [78]. The total number of detectors in a multiplexer therefore does not affect the performance of single pixels. In addition, the bandwidth per pixel is given by the loaded quality factor of the microwave resonator which can be adjusted by changing the coupling capacitor C_c. This allows to maintain the intrinsic fast signal rise time of MMCs.

During the superconducting transition of the film forming the SQUID loop magnetic flux can be randomly trapped inside the superconducting structures. Therefore, the SQUID performance might suffer from a random flux offset that shifts away the SQUID characteristics from the optimal bias point [50,79]. While this offset can be easily compensated using a flux bias coil, an individual flux bias for all SQUIDs of a μMUX is hardly possible due to the number of required electrical wires. The probably most suited solution for this problem is to couple a common flux bias coil to all SQUIDs within the μMUX (see Fig. 16) and to apply a modulation technique, such as flux-ramp modulation [79]. Even though this decreases the signal-to-noise ratio, a flux modulation technique also reduces the effect of low-frequency noise that is introduced after the SQUID, e.g. phase noise due to atomic tunnel systems [74,79].

A big challenge that has to be met when using a μMUX is the generation of the GHz frequency comb and the real-time determination of the amplitude or phase of each transmitted carrier signal. A straightforward solution is to use a software defined radio (SDR) technique (see Fig. 17) such as for microwave kinetic inductance detectors [80–82]. Two digital-to-analog converters (DACs) create two MHz frequency combs that are $\pi/2$-phase-shifted with respect to each other. The frequency spacing between the individual carriers is adjusted according to the frequency spacing of the microwave resonators. The frequency combs are then up-converted using an I/Q-up-converter to match the resonance frequencies of the resonators and are injected into the transmission line. The use of an I/Q-up-converter in combination with two $\pi/2$-phase-shifted frequency combs instead of a standard single-sideband mixer in combination with a single frequency comb effectively doubles the usable bandwidth of the ADCs. After passing the μMUX, the signal is down-converted using an
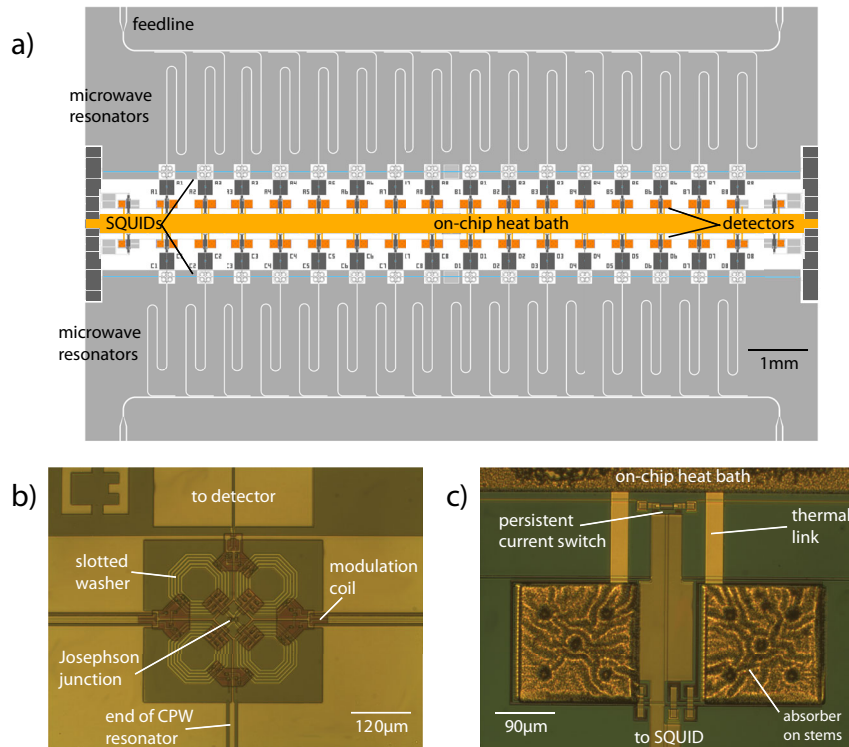
Fig. 18. (a) Design of the first μMUX developed within the framework of the ECHo experiment. (b) Optical photograph of the current-sensing rf-SQUID showing the slotted washers, the sephson junction, the modulation coil as well as the connections to the CPW resonator and the detector. (c) Optical photograph of one two-pixel detector showing the two absorbers connected via five Au stems to the temperature sensor, the persistent current switch as well as the thermal link to the on-chip heat bath.

I/Q-down-converter and digitized by two fast analog-to-digital converters (ADCs). The subsequent signal processing, i.e. the separation of the combined signal into the different carriers as well as the determination of amplitude and phase of each carrier, is done by using a field programmable gate array (FPGA). The FPGA is also used for real-time raw data processing, i.e. for triggering and pulse height determination.

6.3 Prototype multiplexer device

Figure 18a shows the first μMUX developed at the Kirchhoff-Institute for Physics that was designed within the framework of the ECHo experiment. It is described in detail in [83]. This first multiplexer allowed to test the integration of a μMUX and a detector array on the same chip and to specifically demonstrate the compatibility of the fabrication processes for SQUIDs and MMCs respectively. The detector array consists of 32 two-pixel detectors (see Fig. 1c) that are arranged in a 2×16 linear configuration. This arrangement of detectors allows for implantation of ^{163}Ho ions by scanning along the detector line. Each detector consists of two electroplated absorbers made of Au, each covering an area of $170\,\mu$m $\times$ $170\,\mu$m and having a total thickness of $10\,\mu$m. In between the two Au layers, ^{163}Ho can be implanted within a slightly reduced area resulting in a 4π geometry with a quantum efficiency of more
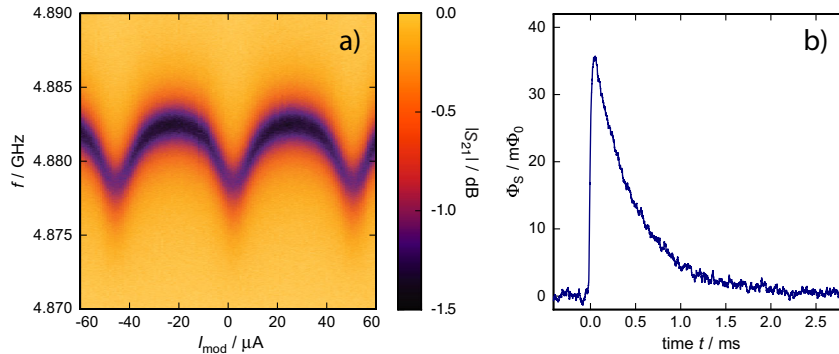
Fig. 19. (a) Transmission measurement of one of the resonators of the μMUX prototype for different currents running through the modulation coil but without the detectors to be biased. (b) Output signal of one of the detectors when a 6 keV photon hits the absorber after demodulation of the microwave carrier.

than 99.9% for particles emitted during the ^{163}Ho decay, using similar methods as described in Sections 4 and 7.4. Each absorber is connected via five stems made of Au to the underlying planar **Au**:Er temperature sensor covering the same area as the absorber. Underneath both sensors, superconducting meander-shaped pickup coils are placed. They are gradiometrically connected in parallel with the input coil of the current-sensing rf-SQUID reading out the detector. The rf-SQUID, which is shown in Figure 18b, is a second order parallel gradiometer. It is formed by four slotted octagonal washers that are connected in parallel. In addition to the input coil, the SQUID is equipped with a common flux modulation coil that runs through all SQUIDs. The coplanar transmission line resonators have a resonance frequency f_r between 4 GHz and 6 GHz which is set by their geometrical length. The coupling capacitance C_c is chosen to achieve a loaded quality factor $Q_l = 5000$ and is implemented by running a part of each resonator in parallel to the common transmission line.

Figure 19a shows a transmission measurement of one of the resonators of the multiplexer device for different currents running through the modulation coil but without the detectors to be biased. It is clearly visible that the resonance frequency of the resonators shifts as the magnetic flux threading the SQUID loop changes. This proves that the device is fully operational. To further characterize the multiplexer, the detectors was biased by injecting a persistent current into the pickup coils of the detectors and monitored the time evolution of the resonance frequency by means of a standard homodyne detection technique. Figure 19b shows the measured output signal of one of the detectors when a 5.9 keV photon hits the absorber. The measured signal size as well as the noise level are consistent with the design parameters, the measured noise temperature of the non-optimized microwave setup and the value of the injected persistent current. This proves that our initial design goal of achieving an energy resolution below 5 eV can be met within ECHo-1k using an optimized microwave setup. Moreover, this is the very first demonstration of a μMUX-based MMC readout.

6.4 Current status and developments for ECHo-1k

Based on the results obtained with the first integrated μMUX MMC array, an optimized detector array with integrated μMUX for ECHo-1k has been developed [84]. In order to enhance the implantation efficiency, the geometrical arrangement of the detector array has been changed. First, the distances between two neighboring detectors as well as between the two absorbers of a detector are significantly reduced to less than

$10\,\mu$m. Second, a different technique is used to heat sink the detectors, which allows to place detector lines closer to each other. More precisely, each temperature sensor is connected to an island made of sputtered Au using well-defined thermal links. For connecting these islands to the thermal bath, i.e. the sample holder, a part of the substrate underneath the islands is etched away using a cryogenic SF_6-based deep reactive ion etching process. The resulting holes are then filled up with electroplated Au forming low-ohmic posts through the Si substrate. These posts are thermally anchored by a continuous Au layer to the backside of the wafer, which will be pressed to the sample holder.

For ECHo-1k, two 64 pixel detector arrays with integrated μMUX will be used. The μMUX is optimized according to the readout requirements of the ECHo experiment, i.e. the degradation of the intrinsic detector energy resolution as well as the slowing down of the signal rise-time will be kept as low as possible. For this, we have thoroughly adjusted the resonator bandwidth, the SQUID-resonator-coupling, the SQUID input circuit as well as the overall SQUID gain. Each μMUX will be then read out by an individual physical readout channel, i.e. one HEMT amplifier and two coaxial cables. For the operation of the μMUXs, i.e. the generation of the baseband frequency comb and the real-time monitoring of the amplitude or phase of each resonator, commercial SDR systems with customizing capabilities will be used. State-of-the-art SDR systems provide a bandwidth of several 100 MHz which directly corresponds to the size of the frequency bands in which the resonance frequencies of all the resonators can be placed.

7 ^{163}Ho source: production and separation

The production of suitably large amounts of radionuclides in high-purity form is of interest for different applications. Examples include radiopharmaceutical use, where the most stringent quality assurance measures are implemented as the radionuclide samples are applied to humans. Other applications include radionuclide source production for industrial radiography (a non-destructive materials testing method) [85] or radioisotope batteries [86]. Several basic research fields also depend on a reliable supply of significant amounts of high-purity radioisotopes, e. g., to be used as target material in nuclear reaction studies, see [87] for an example. The ^{163}Ho is an artificial, long-lived isotope with a half-life, $T_{1/2}$, of $(4570 \pm 50)\,$a [18] and decays via EC. In many respects, its behavior is similar to that of a stable isotope as it does not emit α-, β- or γ-rays. Therefore production of pure ^{163}Ho and its quantification is a challenge, while use of high purity ^{163}Ho, free from any co-produced long-lived radionuclides or from stable lanthanides, is a prerequisite for neutrino mass measurements. Production of ^{163}Ho may be approached either by charged particle reactions using an accelerator or neutron activation in a reactor. Both pathways lead to the co-production of unwanted radionuclides in significant amounts, which must be removed to obtain ^{163}Ho samples suitable for the determination of the neutrino mass. As it will be shown, chemical as well as mass separation play an important role both before and after the irradiation to obtain ultrapure ^{163}Ho free from the bulk target matrix and other coproduced radionuclides. Figure 20 shows a cut-out from the chart of nuclides of the relevant region.

While a first experiment within the ECHo project exploited spallation as the nuclear reaction to produce ^{163}Ho (see Sects. 5 and 7.2), more typical pathways for the production of significant amounts of radionuclides include neutron irradiation of a suitable target at high-flux reactors and charged-particle irradiation at accelerator facilities. Both production pathways were evaluated within the ECHo collaboration and also elsewhere, see [89].

Fig. 20. Chart of nuclides in the region around ^{163}Ho [88] showing relevant isotopes.

Within the ECHo collaboration, ultrapure ^{163}Ho samples need to be produced for two different applications: (i) calorimetric measurements of the spectrum following ^{163}Ho EC decay (see Sect. 4.2), and (ii) Penning-trap mass spectrometry (PTMS) for measurements of the Q_{EC}-value populating ^{163}Dy (cf. Sect. 9). The requirements for the corresponding samples differ: the MMC-based calorimetric measurements require radiochemically and radioisotopically ultrapure samples, as any nuclear decay unrelated to that of ^{163}Ho will generate background in the acquired spectra, hence limiting the sensitivity of the measurement. For proper handling of the background, measurements of the radio-chemical purity of the samples are performed, e.g., in the Felsenkeller low-level underground laboratory at the TU Dresden [90]. This is located beneath an overburden of 125 m water equivalent of rock, which provides significantly reduced background conditions, see [91]. In contrast, in Penning trap mass spectrometry, ions of mass numbers other than 163 will generally not reach the measurement trap (unless they are abundantly present in molecular form with mass 163). However, the Q_{EC}-value measurement needs ^{163}Ho samples where the contamination with ^{163}Dy (stable, 24.9 % natural abundance), which is the only stable isobar, is below $\sim$0.2 %. To avoid overloading of the purification traps with ions, the ratio of ^{163}Ho to the total holmium amount should not be less than 1/10.

To achieve the necessary radio-purity (for the MMC measurements) and sufficiently small amounts of ^{163}Dy (for the PTMS measurements) chemical separation schemes based on ion-chromatography [92] optimized to separate neighboring lanthanides are required, and developments towards the ^{163}Ho separation for neutrino mass measurement projects have been described [93]. The presence of ^{166m}Ho ($T_{1/2} = 1200$ a) in the sample poses a special problem, as chemical approaches cannot provide any elimination of this byproduct, which is especially problematic in calorimetric measurements. Thus, electromagnetic separation is necessary for producing radiochemically ultrapure ^{163}Ho samples without significant traces of ^{166m}Ho. A detailed analysis of different production pathways [89] indicates that the ratio of ^{163}Ho:^{166m}Ho differs significantly among the available options, but ultimately a final isotope separation step appears necessary in all the cases where sufficient ^{163}Ho can be produced within a reasonable time.

7.1 Production pathways for ^{163}Ho

Different pathways offer access to significant amounts of ^{163}Ho. Besides ^{163}Ho, unwanted nuclides are inevitably coproduced, at a level depending on the amount of

impurities present in the target and the chosen production pathway [89]. In the case of ^{163}Ho production, where a lanthanide target is irradiated (Er in case of reactor production, Dy in the accelerator pathway, see below), it is worthwhile pointing out that commercially available samples of any lanthanide element generally contain significant impurities of other lanthanides. Aiming at high radiochemical purity, an inspection of the chart of nuclides immediately reveals that both pathways thus lead to significantly contaminated samples. In the case of reactor production, long-lived neutron-rich isotopes like ^{151}Sm $(T_{1/2} = 93\,\mathrm{a})$, ^{154}Eu $(T_{1/2} = 8.8\,\mathrm{a})$, ^{160}Tb $(T_{1/2} = 72.3\,\mathrm{d})$, ^{166m}Ho $(T_{1/2} = 1200\,\mathrm{a})$, ^{170}Tm $(T_{1/2} = 128.6\,\mathrm{d})$, or ^{177m}Lu $(T_{1/2} = 160.1\,\mathrm{d})$ are the most prominent problematic isotopes. Accelerator production yields samples containing proton-rich nuclei like ^{139}Ce $(T_{1/2} = 137.6\,\mathrm{d})$, several long-lived Pm, Eu, and Lu $(T_{1/2} > 1\,\mathrm{a})$ isotopes and ^{168}Tm $(T_{1/2} = 93.1\,\mathrm{d})$. On the positive side, detection via γ-spectrometry is possible in most cases, as γ-rays of suitable energy and intensity are emitted by these nuclides. Thus, after the samples have been chemically and physically separated, a characterization with respect to radioactive contamination can be performed via low-level γ spectrometry, if desirable also in a low-background environment, as in an underground laboratory, where detection limits of few tens of mBq/kg are reached [90].

7.2 Accelerator production of ^{163}Ho

In the 1980s ^{163}Ho was produced and separated at CERN, Switzerland [20,94,95]. At KEK (Tsukuba, Japan), an enriched Dy target (^{164}Dy$_2$O$_3$) was irradiated with a 20 MeV proton beam to produce ^{163}Ho via the ^{164}Dy(p,2n)^{163}Ho reaction. Holmium was separated from the Dy matrix using an ion-exchange technique where Ho was eluted by alpha-hydroxyisobutyric acid (α-HIBA) from the cation-exchange resin AG 50W-X8 [95]. Katsube et al. measured the excitation function of the residues ^{164}Ho, ^{162}Ho and ^{161}Ho from the ^{164}Dy(p,xn) reaction and compared the results with predictions of the ALICE code [96]. The measured cross sections agreed well with the available theoretical estimations [97]. However in [98] it is discussed how theoretical estimations could be 30–50% higher than the experimentally detected cross-sections. It is thus reasonable to assume that the estimate of $\sim$1000 mb for the production cross sections of ^{163}Ho provided by this method should be considered an upper limit. This means one should consider a 30-50% extra irradiation time when we want to produce ^{163}Ho via the ^{164}Dy(p,2n) reaction.

Spallation At CERN, another effort to produce ^{163}Ho was undertaken by bombarding a tantalum target with a 600 MeV proton beam of 2.4 μA current from the CERN-synchrocyclotron (SC). Rare-earth elements effused from the hot target were surface ionized and then passed through the mass separator at the ISOLDE facility. The fraction of mass 163 contained ^{163}Ho. Due to molecular sidebands, the mass 163 fraction was contaminated with ^{147}Gd and, due to tails of heavier masses, with traces of ^{167}Tm, ^{169}Yb, etc. Therefore, further purification was done by wet chemistry [20,94,95,99]. A very first source of ^{163}Ho embedded in MMCs for the ECHo project was produced in 2009 [32] in the 1.4 GeV proton-induced spallation of a ^{nat}Ta target at CERN-ISOLDE. Reaction products leaving the $\sim$1800-1900 °C hot target were ionized on a hot tungsten surface, accelerated in a 30 kV electrostatic field and separated in ISOLDE's General Purpose Separator (GPS) [60], which provided a mass resolving power of $m/\Delta m \approx 1000$. Spallation reactions populate a substantial fraction of the chart of nuclides, especially on the neutron-deficient side. Some undesired products form molecular ions with mass 163 and were present in the beam delivered by the GPS. The implantation of ^{163}Ho into four MMCs (about 10^9 each) was performed and a first calorimetric spectrum was acquired (see Fig. 12). Besides
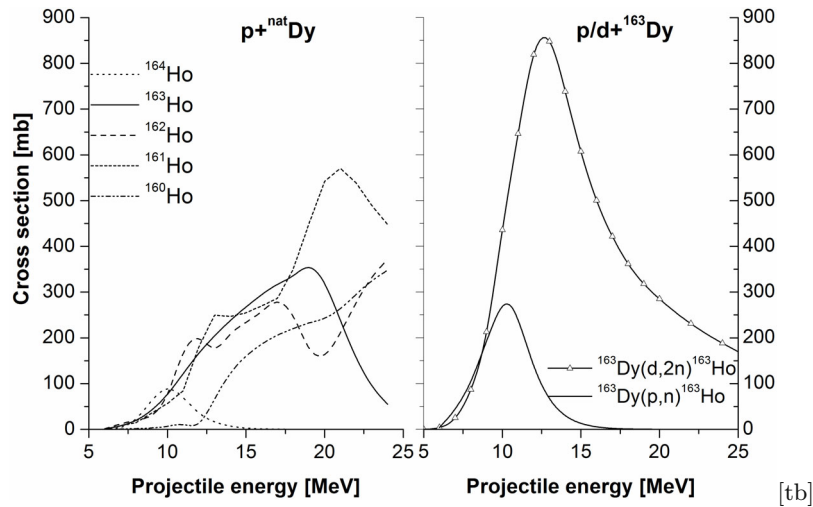
Fig. 21. Calculated excitation functions for the production of Ho isotopes in p- and d-induced reactions on Dy targets. Left: excitation functions of different Ho isotopes from the p+^{nat}Dy reaction as estimated using the ALICE code. Right: comparison of cross sections of ^{163}Ho obtained from TALYS [100] for proton- and deuteron- induced reactions on ^{163}Dy.

lines from ^{163}Ho, most pronouncedly, lines originating from ^{144}Pm also appear in the spectrum, due to contamination of the A = 163 beams with a molecular sideband of ^{144}Pm (as PmF$^+$) and A = 147 oxides. The latter had decayed at the time of the measurement. Due to the comparatively small amounts of ^{163}Ho that can be produced by this approach and the poor purity of the delivered beam, online production and implantation of ^{163}Ho via spallation and subsequent mass separation do not appear promising for the requirements of the ECHo project.

In order to reduce the background in the low energy measurements, it is important to maintain the purity of the source with respect to the radioactive contaminants. In view of this, some theoretical and experimental investigations carried out within the ECHo collaborations are discussed below.

Direct reactions Using the nuclear model codes ALICE [96] and TALYS [100], the cross sections for proton- and deuteron-induced reactions on natural or enriched Dy (^{163}Dy, ^{164}Dy) have been estimated. The ^{163}Dy(p,n)^{163}Ho reaction offers ~ 300 mb cross section at 10 MeV projectile energy, whereas an approximately four times larger cross section, $\sim$1200 mb at 19 MeV, is estimated for the ^{164}Dy(p,2n)^{163}Ho reaction. Using ^{nat}Dy targets, about 350 mb at 19 MeV are obtained, resulting from the two above mentioned reactions [101,102]. Ho isotopes other than ^{163}Ho will also be produced at energies below 25 MeV, namely $^{160-162,164}$Ho as shown in Figure 21 (left). For an enriched ^{163}Dy target, the ^{163}Dy(d,2n)^{163}Ho reaction is found to be superior compared to the ^{163}Dy(p,n)^{163}Ho reaction, as it provides a three times higher cross section of ~ 900 mb at 13 MeV (Fig. 21 (right)) [101,103].

In addition, several long-lived radio-lanthanide contaminants may be co-produced, as shown in Table 2. Some ^{161}Tb might also be present because of the (p, α) reaction on ^{164}Dy, though the cross section of this reaction is smaller than 5 mb. Ideally, highly enriched ^{164}Dy is used to suppress co-production of contaminants in reactions on other Dy isotopes.

The main disadvantage of direct reactions is the reduced size of the produced ^{163}Ho samples. Moreover, similarly to neutron-induced reactions, a difficulty lies in separation of adjacent lanthanides, particularly as the target element (Dy) is present

Table 2. Unwanted side-reactions occuring in the p-induced irradiation of Dy targets.

^{158}Dy(p,2n)^{157}Ho → ^{157}Dy →	^{157}Tb	(99 a)	
^{160}Dy(p,2n)^{159}Ho →	^{159}Dy	(144.4 d)	
^{160}Dy(p,pn)^{159}Dy	^{159}Dy	(144.4 d)	
^{156}Dy(p,3n)^{154}Ho →	^{154}Dy	($3 \cdot 10^6$ a)	
^{161}Dy(p,α)^{158}Tb	^{158}Tb	(180 a)	
^{163}Dy(p,α)^{160}Tb	^{160}Tb	(72.3 d)	($\sigma \approx 5$ mb up to 50 MeV)
^{164}Dy(p,α)^{161}Tb	^{161}Tb	(6.9 d)	($\sigma \approx 5$ mb up to 50 MeV)

in mg-size quantity and the amount of ^{163}Ho will be of the order of micrograms only. Therefore, indirect reactions were also studied.

Indirect reactions The exploration of the production of pure ^{163}Ho in an indirect production route is reported in [101,104]. Here, we will discuss mainly the following reactions $^{nat/enriched}$Dy(α, xn)^{163}Er →^{163} Ho and ^{159}Tb(^{7}Li, 3n)^{163}Er(EC)^{163}Ho. The desired pathway of the α-particle induced reaction on a Dy target is $^{nat/enriched}$Dy(α,xn)^{163}Er → ^{163}Ho. Specific aspects to this production route when compared to the direct one include:

(i) the activity of ^{163}Er through the above nuclear reaction will be very high due to its short half-life (75 minutes). However, in terms of the number of atoms, both proton and α-particle induced reactions offer $\sim 1 \times 10^{11}$ atoms/μA·h of ^{163}Ho for a target thickness of 10 mg/cm^2. As the half-life of ^{163}Er is only 75 min, the maximum activity will be available after about 6.5 h. Therefore, production-separation cycles for large ^{163}Ho amounts need to be repeated many times. To avoid high exposure due to the high ^{163}Er activity and the many production-separation cycles, all steps will ideally be performed by remote operation.

(ii) to avoid the many separation cycles, the separation of the ^{163}Ho daughter at the end of a long production cycle might be worthwhile.

(iii) on the other hand, it might be easier to separate ^{163}Er from the Dy target rather than the separation of Dy-Ho, as the former introduces between the target and the product a two atomic number increment.

For both approaches, the separation of ^{163}Er or ^{163}Ho from the Dy target, suitable tracers exist – co-produced ^{161}Er (3.21 h) in the former case, and ^{166}Ho (26.80 h), which can be produced without simultaneous production of undesired ^{166m}Ho (1200 a) in double-neutron capture on ^{164}Dy in a research reactor with a reasonably high neutron-flux, in the latter – which will allow tracing the desired fraction in the chemical separation procedure.

Production cross sections of ^{163}Er from each abundant isotope of Dy in α-induced reactions, i.e., $^{160-164}$Dy(α,xn)^{163}Er have been estimated using the ALICE code [96]. The most attractive ^{163}Er production pathway appears to be from ^{161}Dy (~ 600 mb at 26 MeV), ^{162}Dy (> 1000 mb at 35 MeV), and ^{163}Dy (~ 1000 mb at 45 MeV) below 50 MeV α-particle energy (see Fig. 22).

Such a comparatively low α-particle energy (< 50 MeV) suppresses the production of long-lived radioactive impurities like ^{159}Dy (144.4 d), ^{157}Tb (99 a), ^{158}Tb (180 a), ^{154}Dy (3×10^6 a) in any of the above enriched matrices. Since the 100 % enrichment of a Dy isotope is a difficult and expensive task, the co-production from a natural Dy target of ^{160}Er (28.6 h), ^{161}Er (10.3 h), ^{163}Er (75 min), and ^{165}Er (10.3 h), along with ^{163}Ho were also studied. The maximum cross section (> 500 mb) for ^{163}Er was obtained at ~ 38 MeV energy. It was also evident that production of ^{159}Er and ^{159}Ho, which eventually decay to the long-lived ^{159}Dy, is mostly coming from ^{156}Dy(α,n)^{159}Er (~ 200 mb at 20 MeV), ^{158}Dy(α,3n)^{159}Er (~ 1150 mb at 40 MeV), ^{160}Dy(α,5n)^{159}Er, ^{158}Dy(α,p2n)^{159}Ho reactions. The production of ^{159}Dy (144.4 d)
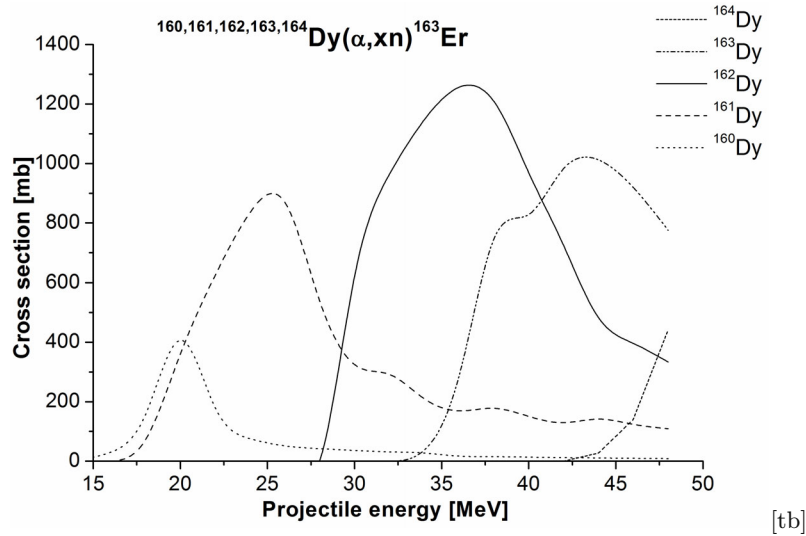
Fig. 22. Excitation functions of ^{163}Er from α-induced reactions on various Dy-targets [103] calculated using ALICE [96].

is possible mainly from the two least abundant isotopes, ^{156}Dy and ^{158}Dy, below 40 MeV. Therefore, using a natural Dy target may introduce minute amounts of long-lived impurities in the target matrix.

The ALICE code was also used to study the use of Terbium targets (which are monoisotopic) to produce ^{163}Ho through the ^{159}Tb(^{7}Li,3n)^{163}Er(EC)^{163}Ho reaction. The ^{163}Er is produced with $\sigma \approx 300$ mb at 30 MeV via ^{159}Tb(^{7}Li,3n)^{163}Er. Short-lived ^{163}Er (75 min) decays to the long-lived ^{163}Ho [105]. Even if the cross-section for this reaction is smaller with respect to the cross-sections for ^{163}Er production using dysprosium isotopes, this process does not lead to the production of long-lived impurities and the chemical separation of the Ho-Tb pair might be much easier compared to the Er-Dy and Ho-Dy pairs. On the other hand it is important to consider that the available ^{7}Li beam intensity is less than 1 μA. Therefore, this production route may be suitable if comparatively small amounts of ^{163}Ho are needed, and additional purification is not feasible.

Another indirect production route is the p-induced reaction on ^{164}Er, leading to ^{163}Ho via the ^{164}Er(p,2n)^{163}Tm (1.8 h) $\rightarrow$ ^{163}Er (75 min) $\rightarrow$ ^{163}Ho path. The main disadvantage of this route is the low natural isotopic abundance of ^{164}Er, which is only 1.6 %.

Chemistry In order to reduce the amount of other (radioactive or stable) lanthanides in a ^{163}Ho sample, we developed a chemical separation technique of erbium from bulk dysprosium, details of which are available in reference [103]. A non-hygroscopic natural dysprosium oxide (Dy$_2$O$_3$) target of (12 ± 0.5) mg/cm^2 thickness on a 1.5 mg/cm^2-thick aluminum backing was bombarded by 40 MeV α-particles for 5.5 h up to a total dose of 4.4×10^4 μC. The presence of ^{161}Er in the matrix was assured by γ-spectrometry. No holmium radioisotopes were observed above detection limit in the irradiated target matrix. Since the use of di-(2-ethylhexyl)phosphoric acid (HDEHP) in liquid-liquid extraction (LLX) is established in the separation of lanthanides [104,105], the same reagent was used to separate no-carrier-added erbium radioisotopes from bulk dysprosium target. The study shows that at lower acidity (≤ 0.01 M HCl), both the lanthanides are extracted to the HDEHP phase while both

stay in the acid phase at 1 M HCl concentration. The variation of HCl concentration (0.1 M–0.4 M) was studied against two HDEHP concentrations, 1 % and 0.5 %. The extraction of both metals was reduced at 0.5 % HDEHP compared to that of 1 % HDEHP. Optimum separation was achieved at 0.2 M HCl and 1% HDEHP where ∼ 80 % erbium and ∼40 % dysprosium were extracted into the HDEHP phase. The dysprosium fraction was back extracted quantitatively from the 1 % HDEHP to the aqueous phase with the help of 0.5 M HCl phase along with ∼ 25 % erbium. The rest of the erbium was brought back to the aqueous phase using 6 M HCl [103].

7.3 Reactor production of ^{163}Ho

Well before production using particle accelerators, ^{163}Ho had already been prepared and identified by a three month reactor irradiation of enriched ^{162}Er, followed by chemical separation via cation exchange chromatography and electromagnetic mass separation [106]. After renewed interest in ^{163}Ho, the same production route was again followed in the 1980s [18,30].

If compared to charged-particle irradiation at accelerator facilities, neutron irradiation profits from large cross sections for neutron-induced reactions. Hence, large amounts can be produced comparatively quickly. In addition, a multitude of samples can be irradiated simultaneously in a reactor, in contrast to needing dedicated accelerator operation, thus facilitating easier access to a facility for irradiation time. Sufficient ^{163}Ho for the ECHo project can be produced via thermal neutron activation of ^{162}Er and the subsequent EC decay of the resulting ^{163}Er ($T_{1/2} = 75$ min), see Figure 20. The cross section for the reaction ^{162}Er(n,γ)^{163}Er is 19 b [107]. Erbium oxide with an isotopic enrichment of ^{162}Er up to about 40 % is currently commercially available. With such samples, some 10^{18} to 10^{19} atoms of the long-lived ^{163}Ho can easily produced by steady-state irradiation of several tens of mg large Er targets for several weeks in high flux research reactors (such as the reactor at the Institut Laue-Langevin in Grenoble, France or the HFIR-reactor operated at the Oak Ridge National Laboratory in Oak Ridge, USA) at a thermal neutron flux exceeding 10^{15} cm^{-2}s^{-1} [108].

Within the ECHo collaboration, the Institute for Nuclear Chemistry at the Johannes Gutenberg University Mainz, which has decade-long experience with high-performance chemical separation of substantial amounts of radionuclides, see, e.g., [109–111], performs the chemical separation. The mass separation is performed at the RISIKO mass separator [112,113] operated at the Institute of Physics at the Johannes Gutenberg University Mainz or at the General Purpose Separator at the ISOLDE facility at CERN [60] to further purify the initial ^{163}Ho samples by an efficient and selective suppression of the ^{166m}Ho contamination.

Chemical separation procedure After the production of a small amount of ^{163}Ho by proton-induced Ta-spallation at ISOLDE-CERN (see Sect. 7.1), further samples were produced, so far exclusively in the reactor production pathway. In the following, the development and implementation of the strategy of the ECHo collaboration to obtain radiochemically pure ^{163}Ho samples is described; for details see [114].

An exploratory neutron irradiation of 5 mg ∼ 30 % enriched ^{162}Er was performed for 11 days at the BER II research reactor of the Helmholtz-Zentrum Berlin, at a thermal neutron flux of 1.2×10^{14} cm^{-2}s^{-1}. A calculation of the number of ^{163}Ho atoms produced in this irradiation, based on the number of target atoms, neutron flux, irradiation time, and ^{162}Er(n,γ) cross section suggests that 1.5×10^{16} ^{163}Ho atoms should have been produced. However, this calculation should be regarded as the most optimistic value for two reasons: first, it neglects burn-up of ^{163}Ho during the irradiation due to neutron capture. Second, a substantial fraction of the irradiated Er

consisted of ^{167}Er, which has a high neutron capture cross section of 650 b, thus acting as a neutron poison. As long as ^{167}Er is present in substantial amounts, this leads to a reduced local neutron flux, thus reducing the production of ^{163}Ho. How strongly these two factors influence the final yield of ^{163}Ho is uncertain. As expected, multiple long-lived contaminants (e.g., ^{46}Sc, ^{110}Ag, ^{169g}Yb, ^{170}Tm, ^{192,194}Ir) were identified in significant quantities in the sample. Ion-chromatographic separation using standard Dowex AG1X8 resin material and α-HIBA as eluting agent was applied to separate the micro-quantities of ^{163}Ho from the Er bulk material and from impurities due to other lanthanides. The resulting chromatogram revealed only a minor fraction of Ho to be Er-free. In later separations, the decontamination factors of neighboring elements have been significantly improved by the use of advanced resin material compared to standard resins that have been used in the past.

To minimize the content of unwanted products from other elements, the following scheme was applied for the production of the next ^{163}Ho samples. For details, see [114].

(i) Commercially available enriched ^{162}Er [isotopic composition: ^{162}Er: $(20.4 \pm 0.1)\,\%$; ^{164}Er: $(3.94 \pm 0.05)\,\%$; ^{166}Er: $(33.5 \pm 0.1)\,\%$; ^{167}Er: $(17.6 \pm 0.1)\,\%$; ^{168}Er: $(17.3 \pm 0.1)\,\%$; ^{170}Er: $(7.29 \pm 0.05)\,\%$]) was chemically purified prior to irradiation employing the new ion-chromatographic resin material. All lanthanide elements lighter than Er were removed quantitatively, thus preventing the production of undesired radioisotopes of elements lighter than Er during the subsequent irradiation.

(ii) Two samples of the purified Er were irradiated for 54 and 56 days respectively at the high-flux reactor of ILL Grenoble in fluxes between 1.2×10^{15} and $1.5 \times 10^{15}\,\mathrm{cm}^{-2}\mathrm{s}^{-1}$, yielding an amount of ^{163}Ho atoms of the order of 10^{18}. A more precise quantification is currently ongoing.

(iii) Both samples were chemically separated using an advanced chemical separation scheme similar to that used for the purification prior to irradiation, but tailored to yield the lighter lanthanides before the heavier ones.

The position of holmium during chemical separation can be determined by adding, after the irradiation, carrier-free pure ground-state ^{166}Ho ($T_{1/2} = 26.80\,\mathrm{h}$) which can be separated from neutron irradiated ^{164}Dy, which has been previously purified from Ho. This method allows to monitor the separation from all heavier lanthanides, including the erbium target material and thulium byproducts (especially the long-lived ^{170}Tm and ^{171}Tm, which were formed in GBq amounts from heavy Er-isotopes during irradiation).

The radiochemical purity of the obtained Ho fraction was analyzed by γ-spectroscopic measurements. These demonstrate that ^{166m}Ho is the only detectable γ-emitting contaminant, as shown in Figure 23. Any other contaminant is present at most at a significantly smaller activity level. Decontamination factors > 500 for erbium and $> 10^5$ for thulium have been achieved by the chemical processing of the target with $\sim$95% yield for Ho.

7.4 Mass separation

For the MMC-based calorimetric measurements, the ^{166m}Ho content of the samples is substantially too large. Therefore, a mass separation step of the obtained Ho fraction is required. For ECHo, the acceptable level of contamination with radionuclides other than ^{163}Ho depends on their half-lives and the energy their decay deposits in the MMCs. For ^{166m}Ho, a maximum atom content up to a few units in 10^{-9} relative to ^{163}Ho appears acceptable for the ECHo project. Within ECHo, the mass separation has so far been carried out at two mass separators which have very similar properties.
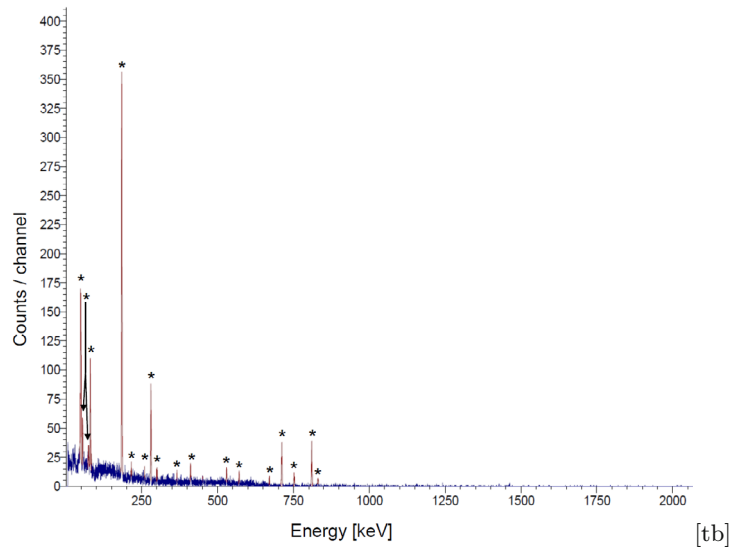
Fig. 23. Gamma spectrum of the Ho fraction, isolated from one of the erbium targets. Peaks labeled with an asterisk originate from ^{166m}Ho.

One is the ISOLDE GPS in off-line mode, where first implantations of ^{163}Ho into MMCs were performed using a sample that was chemically processed as described in Section 7.3 [64]. ^{163}Ho-implanted MMCs produced in this run have been employed to obtain the calorimetric spectrum shown in Figure 12. A second attractive option for performing this final separation step is to employ the RISIKO mass separator in Mainz (see Fig. 24), which is installed in close proximity to the labs employed for the chemical separation procedure. RISIKO is a 30 kV high transmission mass separator that has been set up specifically for elemental ultra-trace determination using resonance ionization mass spectrometric (RIMS) techniques with lasers [115]. As one of the leading development facilities for on-line laser ion sources worldwide, it is equipped with a number of tunable solid-state laser systems for resonance ionization. This combination of laser spectroscopic and mass spectrometric selection ensures both, high overall ionization and retrieval efficiency for the analyte, in combination with optimum suppression of the contaminating isotope or isobar by many orders of magnitude [116]. Efficient resonance ionization schemes for Ho were developed by the Mainz group at the Holifield Radioactive Ion Beam Facility at Oak Ridge National Laboratory [117], showing specifically high ionization efficiency of up to 40 %. In preparatory experiments with stable ^{165}Ho with calibrated atom amounts in the range of 10^{14} to 10^{16}, reproducible efficiencies in the range of (32 ± 5) % independent of the sample size were reached at RISIKO [113].

In addition to the yield measurement, the relative suppression of neighboring masses was studied by analyzing the shape of a single isotope peak in the mass spectrum. As shown in Figure 25, the peak exhibits long tails below the Gaussian part, which dominate the achievable suppression of neighboring masses. For the ^{166m}Ho/^{163}Ho separation, the relative ion current at $\Delta m = -3$ is important, which is around 3×10^{-5}. With an expected ^{166m}Ho content of about 1×10^{-4} in the reactor produced ^{163}Ho after chemical separation, a ratio of ^{166m}Ho atoms per atom ^{163}Ho in the MMC detectors of a few units in 10^{-9} could be reached. As described in Section 8.4, this would be at the edge of the allowed values. Therefore, upgrade work in the ion source region of RISIKO has been implemented and served to improve
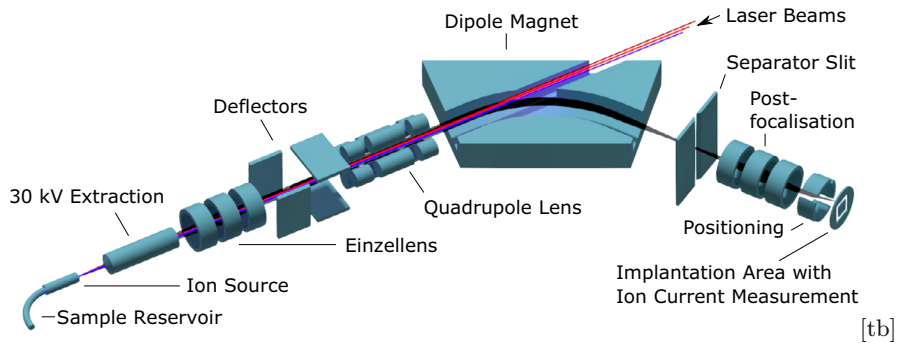
Fig. 24. Overview of the RISIKO mass separator used for the isotope separation and ion beam implantation.
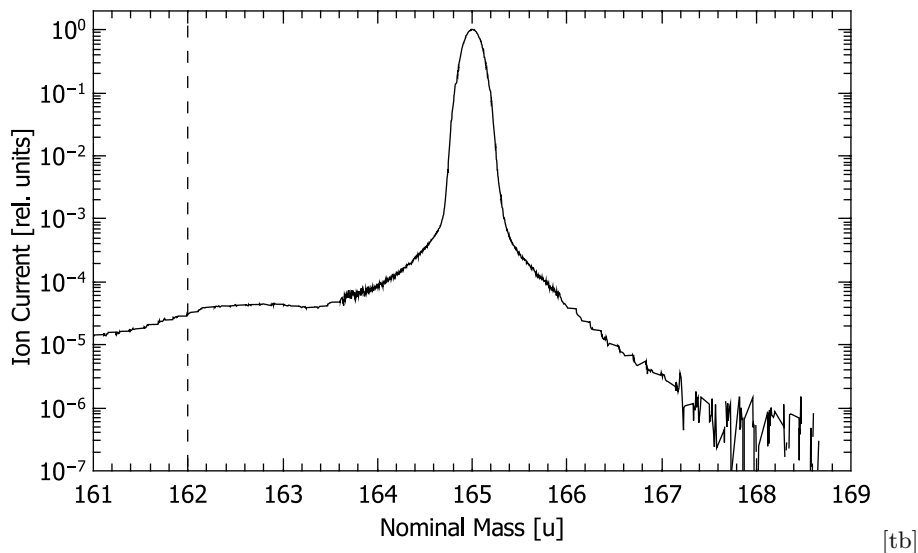

Fig. 25. Mass spectrum of stable ^{165}Ho recorded at the focal plane of RISIKO. The peak features extended tails, especially towards lower ion energies. The dashed line marks the position of $\Delta m = -3$, from which the expected suppression for $^{166\mathrm{m}}$Ho in the implantation is extracted.

both the separation and the ion trajectories [118]. Furthermore, the use of ^{162}Er with higher enrichment will lead in the future to lower $^{166\mathrm{m}}$Ho initial concentrations.

The spatial distribution of implanted ions was visualized by radiographic imaging [119] of the radiation emitted after neutron activation of the implanted ^{165}Ho. The beam spot is elliptical with a FWHM of 3.5 mm in the horizontal direction and 1.5 mm in the vertical direction. This is significantly larger than the size of the individual MMCs. Consequently, the efficiency for implanting an available number of ^{163}Ho atoms using RISIKO can be significantly improved by the installation of astigmatic focusing optics in front of the separator magnet as well as further focusing optics between the focal plane and the position at which the beam is implanted. These upgrade measures have led to a circularly shaped beam spot with a FWHM of 0.7 mm, much better suited to the size of the MMC detectors [118].

For calorimetric measurements with MMCs, the ^{163}Ho atoms need to be implanted in the center of a 5-μm thick absorber, ensuring that no radiation is escaping the

absorber. Therefore, with RISIKO (or ISOLDE-GPS), implantation into a half-thick layer, followed by covering with an additional 5-μm thick Au layer is an ideal solution to combine mass separation of ^{163}Ho with preparation of samples suitable for calorimetric measurements. While losses of ^{163}Ho initially were substantial - almost 90 % of the ^{163}Ho atoms reaching the focal plane were not transmitted to the detectors - the implemented upgrade measures at RISIKO as well as the design of further MMC arrays, where the detectors are more densely packed and arranged in a way ideally adapted to the ion beam profile, allowed the overcoming of these issues.

7.5 Preparation of samples for ECHo and their characterization

Samples for microcalorimetric measurements So far, implantations of ^{163}Ho for the measurement of the calorimetric spectrum have been performed at ISOLDE GPS [32,64] and at RISIKO [113,118] as described above. Further implantations for the study of all relevant aspects of the ^{163}Ho EC, for the optimization of detectors, and for the production of the ECHo-1k detector array for the measurement of the high-statistics spectrum are ongoing.

Samples for Penning trap mass spectrometry For the direct determination of the mass difference between ^{163}Ho and ^{163}Dy by Penning trap mass spectrometry, separate samples are needed for each isotope. Both the Penning traps used in preparatory studies (TRIGA-TRAP, Institute for Nuclear Chemistry, Mainz University [120]) and the first direct high precision measurements (SHIPTRAP, GSI Darmstadt [23]) employ a laser ablation ion source and a dedicated Penning trap in which the produced ion ensemble is separated by mass. Although the laser ablation ion source produces ions from the sample not only of the elementary species but of monoxide, dioxide or hydroxide species as well, the mass resolving power of $m/\Delta m > 10^5$ of the purification Penning trap is typically able to select a specific isotope, even eliminating possible isobaric molecular sidebands. But in the case of the tiny mass difference between ^{163}Ho and ^{163}Dy, a separation is not possible, therefore both ion species would enter the measurement trap and make the measurement impossible.

The sample for ^{163}Dy was made from either commercially available dysprosium nitrate pentahydrate dissolved in nitric acid (TRIGA-TRAP) or from a single element standard for ICP-MS (inductively coupled plasma mass spectrometry) analysis of dysprosium (1000 ppm) in 4 % nitric acid (SHIPTRAP). For each measurement run, at TRIGA-TRAP and SHIPTRAP, 4×10^{15} to 10^{16} atoms of Dy, i.e., about $(1.0 - 2.5) \times 10^{15}$ atoms ^{163}Dy, in 10 μl solvent were dried on a 2 mm spot on a glassy carbon SIGRADUR substrate for TRIGA-TRAP and 5 mm $\times$ 5 mm Ti foil for SHIP-TRAP, respectively. The ^{163}Ho samples were taken from the chemically purified sample and a similar amount was dried on a second spot on the same substrates. Both Penning trap experiments were successful and did not indicate a ^{163}Dy contamination in the original solution or cross-contamination of the two samples due to the laser ablation.

In addition, samples will be prepared for commissioning and future exploitation of the PENTATRAP facility [121] (see Sect. 9). The ion production mechanism for PENTATRAP will differ significantly from that for TRIGA-TRAP and SHIPTRAP, mainly because PENTATRAP will make use of highly charged ions, in contrast to the singly charged ions employed by the other two facilities. First preparatory work involves the preparation of samples with stable ^{165}Ho. Currently, electrochemical deposition of Ho on thin titanium wires appears ideally suited for this. Later on, ^{163}Ho samples will be produced, facilitating the measurement of the ^{163}Ho Q_{EC}-value with ultra-high precision of the order of 1 eV.

7.6 Sample characterization

Along the process of chemical and physical separation to the final samples, knowledge of the sample constitution is crucial for characterizing and minimizing systematic uncertainties, excluding mistakes as well as optimizing the process at each step. The dominant radioactive species can be identified and quantified by γ-spectrometry. After chemical separation, only peaks belonging to ^{166m}Ho appear in the spectra, as ^{163}Ho does not emit any radiation beyond 2.8 keV energy. For further characterization of the samples, ICP-MS, RIMS and NAA (neutron activation analysis) are used. Whereas ICP-MS offers a quick and reliable way to determine relative and absolute contents, it is limited by isobaric systems. In this case, the application of resonance ionization in RIMS can easily enhance the ion currents from one element to another by two orders of magnitude. Here, a more detailed determination of the dysprosium isotope composition in the ^{163}Ho sample after chemical separation is foreseen. After mass separation, no stable co-implants above 10^{-5} are expected. Concerning ^{166m}Ho, the expected relative concentration of 10^{-9} may be not too far from becoming critical. Therefore, its direct quantification, e.g., by γ-spectrometry, is ongoing.

8 Background identification and reduction

In order to achieve the designed sensitivity for the ECHo experiment, the different sources of background have to be analyzed and reduced. In the first phase of the ECHo experiment, ECHo-1k, in one year of measuring time, a statistics of about 10^{10} ^{163}Ho electron capture events in the full spectrum will be collected. In this phase, MMC arrays with a total number of about 100 detectors, each detector being loaded with an activity of the order of 10 Bq of ^{163}Ho, will be employed. For the determination of the neutrino mass, the interval of the spectrum around the endpoint, which is defined by the total energy available to the decay $Q_{EC} = 2.833 \pm 0.030_{stat} \pm 0.015_{syst}$ keV [23], will be analyzed. Only a small fraction of all ^{163}Ho EC events of about 5×10^{-10} is expected within the last 10 eV below Q_{EC}. In ECHo-1k, this corresponds to a signal rate of $\sim 1 \times 10^{-4}$ counts/eV/det/day. Due to the low number of expected signal counts, the fluctuations are governed by Poissonian statistics, thus a simple subtraction of the expected background from the observed number of events in the region of interest is not possible. To reduce the statistical weight of background events in the analysis, the sum of all background sources must be reduced below the level of the signal rate. In the following we discuss how to identify background sources affecting the energy region below 6 keV, how we model their contribution in the calorimetrically measured spectrum using Monte Carlo simulations and which strategies can be adopted to reduce the effect of those events to a negligible level. Furthermore, we show how the developed Monte Carlo simulations can be checked against dedicated test measurements to verify and improve the accuracy of the simulations.

8.1 Study background sources

The background for the ECHo experiment can be classified in mainly five categories:

(1) irreducible background from the unresolved pile–up of ^{163}Ho EC events which is related to the ^{163}Ho activity per pixel and to the time resolution of the detector;

(2) bulk contaminations of the detectors which are assumed to be dominated by radioisotopes which could be implanted together with the ^{163}Ho, in particular ^{166m}Ho;

(3) ambient radioactivity due to natural occurring α-, β-, EC and γ- unstable nuclides;

(4) cosmogenic muons as well as the hadronic part of cosmic rays, in case the experiment is performed above ground, and the cascades of secondary particles;

(5) radionuclides produced by neutron interaction (interesting are the case of production of ^{162}Ho and ^{164}Ho).

In Section 3.2 the sensitivity on the electron neutrino mass was discussed assuming that the unresolved pile-up is the dominant component of the background at the end point region of the ^{163}Ho spectrum. For the presently planned two phases of ECHo, this assumption defines the allowed background level. For ECHo-1k the background level should be $b < 10^{-5}$ counts/eV/det/day while for ECHo-1M the goal is to improve by at least one order of magnitude and reach $b < 10^{-6}$ counts/eV/det/day. To reach these goals, several investigation lines have been started.

The most sensitive parts of the ECHo detectors are the absorber and the sensor, while other parts of the detector chip are either insensitive or energy depositions into such parts can be discriminated from events in the absorber by pulse shape discrimination [32]. Radioactive contaminants are present in the raw materials and may be further accumulated during the storage and the assembly of the experimental setup due to cosmogenic activation and exposure to radon contaminated air and dust particles. The screening of the different materials used for the detector fabrication and assembly with low background gamma spectrometers will be used to select radiopure components as well as to define an upper limit for the presence of dangerous radioactive nuclides.

For the ECHo experiment a detailed model of background in the calorimetrically measured spectrum through Monte Carlo simulation will be developed. In many cases, this will consist in studying the low energy emissions in typical natural radioactive nuclides, in particular cases the decay of more exotic radioisotopes will be modeled and included in the simulations. In the following, we want to discuss a few specific radionuclides which have been studied through Monte Carlo simulation: the effect of ^{166m}Ho, which could be co-implanted with ^{163}Ho, of ^{210}Pb and ^{40}K, both natural occurring nuclides which could be present nearby the sensitive part of the detectors.

Finally plans to reduce the effect of cosmic radiation will be discussed. ECHo-1k is foreseen to be installed above ground and in this case we consider to reduce this background by synchronizing the signal of the detectors containing the ^{163}Ho with signals from a specifically designed muon veto.

8.2 Material screening

The material screening of the components used in the construction of the ECHo experiment is required to control the level of radioactive contaminants in the experimental setup. Two facilities with a high purity germanium (HP–Ge) detector are available for the screening of materials to be used in the fabrication and installation of the detectors as well as for a local shielding:

– the underground laboratory (UGL) at Eberhard–Karls–Universität Tübingen with a shielding of 16 meters of water equivalent (mwe) respect to cosmic muons [122];

– the Felsenkeller underground laboratory near Dresden with an overburden of rock of 47 m which corresponds to a muon shielding of 125 mwe [123].

Due to the small size of the different components of the detector setup, it is not possible to define the contamination for each of them. For the material screening, therefore, sputtering targets, used in the microfabrication of the detectors, as well

as samples of the order of 10^2 g to 10^3 g from which parts of the detector can be machined or selected will be analyzed through gamma spectroscopy.

Of particular interest for the ECHo experiment is to set a limit on the traces of ^{166m}Ho with respect to ^{163}Ho which could be present in the implanted beam. The goal for the ECHo experiment is to reduce the ratio ^{166m}Ho$/^{163}$Ho to less than a few units in 10^{-9}. According to what discussed in Section 7, first tests on the chemical purification of ^{163}Ho sources indicate a contamination level ^{166m}Ho$/^{163}$Ho $\sim 10^{-4}$ which, combined with the precise mass separation between ^{163}Ho and ^{166m}Ho (separated by 3 mass units) the presence of ^{166m}Ho in the ^{163}Ho beam could be reduced more than four orders of magnitude. The left ^{166m}Ho contamination would then be very close to the allowed value. Nevertheless, for each implantation cycle, the presence of ^{166m}Ho will be tested with respect to the amount of the implanted ^{163}Ho. Such an expected small contamination level in the implanted atoms will make the identification of ^{166m}Ho in single detectors impossible. Because of that, a precise Monte Carlo code, able to simulate the effect of such a source in the calorimetric measurement, is of outmost importance to define systematic uncertainties.

8.3 Monte Carlo simulations

Monte Carlo simulations are an important tool for the investigation of the detector performance and background effects on the measured spectrum. The high energy physics standard Monte Carlo simulation framework GEANT4.10.0.1 [124,125] and the ROOT framework for data processing and analysis are used as basis for the simulations discussed here. Due to the particular requirements of the ECHo experiment GEANT4 simulations have to take into account the following peculiarities:

- the energy range which is interesting for the ECHo experiment, 0–6 keV, is very low with respect to the energy ranges used in other GEANT4 applications;
- the typical particle absorber geometry of about $200\,\mu$m $\times$ $200\,\mu$m $\times$ $10\,\mu$m is tiny compared to standard sizes in high energy physics experiments;
- the decay scheme of natural occurring radioactive nuclides (already very precisely characterized for energies larger that 100 keV for experiments searching for direct dark matter interactions or neutrinoless double beta decay [126]) is still not so well defined for the atomic de-excitation components;
- the correct creation and propagation of secondary low energy particles produced in processes like fluorescence, ion sputtering and other decay modes must be ensured in the simulation and these models must be validated against appropriate measurements;
- nuclides such as ^{163}Ho, with forbidden K- and L-shell capture, and the long-lived isomer ^{166m}Ho are quite exotic in the context of standard applications in GEANT4.

It is therefore important to test if the models used in the simulations reflect the physical process well enough. This requires to perform dedicated measurements to benchmark the simulation.

For a large fraction of typical background sources such as cosmic radiation, gamma and alpha particles, a direct hit of the primary radiation on the detector generally deposits too much energy to interfere with the small region of interest below the endpoint of the spectrum around 2.8 keV. However, these particles could deposit just a fraction of their energy in the interaction with the detector material or create secondary radiation at lower energy and even sputtered nuclei with rather low energies. In all these cases, structures in the ^{163}Ho spectrum could appear. In the same way, atomic de-excitations following the decay of unstable nuclides, where X-rays and low
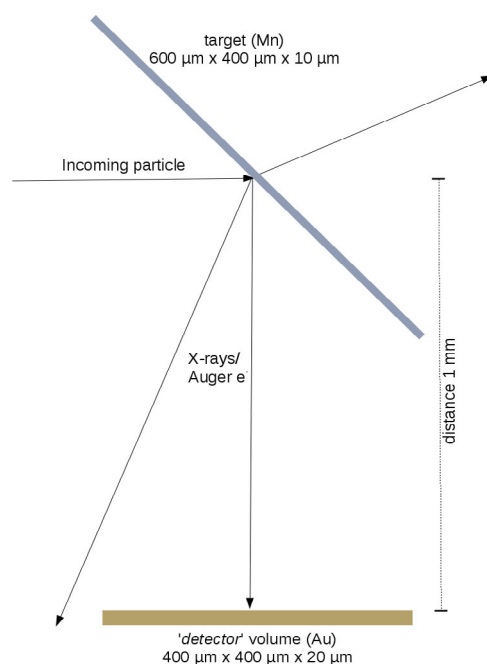
Fig. 26. The test setup in the simulation is composed by a large "detector" volume ($400\,\mu$m $\times$ 400 μm $\times 20$ μm) made out of gold beneath a very thin manganese target ($600\,\mu$m $\times$ 400 μm $\times$ 10 μm) located at the distance of 1 mm above the gold volume.

energy electrons are emitted, contribute to the background. For the investigation of such background contributions on a realistic experimental setup, the usage of Monte Carlo simulations is mandatory.

The precision in generating low energy particles in a simulation of electromagnetic radiation depends crucially on the accuracy and completeness of the used database for the atomic shell structure. The uncertainties in the energy loss function for particles having such low energies, which is of the order of 10% [127], should be carefully considered.

An important aspect in the development of the Monte Carlo simulations for electromagnetic radiation is the definition of a minimum energy or minimum step length to which electromagnetic particles are propagated. Particles with a range smaller than the minimum step length are usually stopped and their kinetic energy is deposited in the volume they are in. This means that if a too large step size is chosen, an artificially enhanced stopping power of the detector is obtained and if a too small step size is chosen, the computation time required by the simulation grows. To simulate interactions in a detector having a gold absorber with the typical size discussed above, a step length of 500 nm is sufficiently small to resolve the details of the energy loss.

The electromagnetic physics lists provided with GEANT4 were checked for their ability to reproduce the full spectra of fluorescence X-rays, Auger electrons and particle induced X-rays (PIXE) and ensure that the secondary electrons and X-rays are produced as dynamic particles which are propagated through the simulated setup as shown in Figure 26. X-rays and electrons which were emitted perpendicular to the beam direction hit the gold detector and the type of particle, its kinetic energy and the deposited energy were collected into a detector spectrum. The energies and ratios of the given lines were then compared to the literature and were found to be in good agreement with both the Penelope physics list and the LivermoreEM physics list.
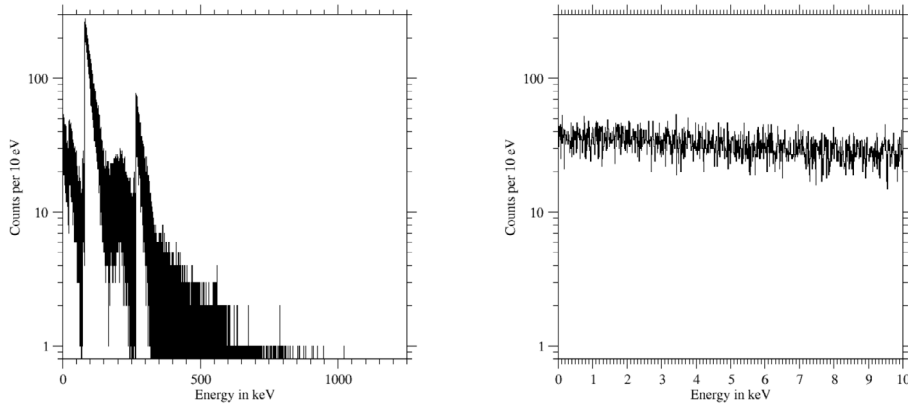
Fig. 27. Energy deposition in the gold absorber of an MMC with dimensions as discussed in the text for 10^6 $^{166\mathrm{m}}$Ho decays with a binning of 10 eV. (Left) The complete energy range investigated in the simulation is shown. The various β^--decay branches of $^{166\mathrm{m}}$Ho are clearly visible. (Right) The low energy region up to 10 keV is shown. A flat spectrum is observed across the ROI with 40 counts/ 10 eV/ 10^6 primary events, i.e. a fraction of 4×10^{-5} of all $^{166\mathrm{m}}$Ho decays will be found within a 10 eV bin around the ROI.

After comparing the results obtained in the different simulations, the LivermoreEm, which includes more atomic shells for the calculation of the secondary particles, was selected.

8.4 Co-implanted $^{166\mathrm{m}}$Ho

Dangerous bulk background sources are radioisotopes which could be co-implanted with ^{163}Ho in the detector chip [32]. $^{166\mathrm{m}}$Ho, a long-lived β-emitter, $T_{1/2} = 1200$ a, $Q = 1854.7$ keV, has two low energy β-decay branches having $Q = 33.1$ keV with $E_{\beta_{\mathrm{mean}}} = 8.38$ keV and $Q = 73.7$ keV with $E_{\beta_{\mathrm{mean}}} = 19.02$ keV respectively [128,129], which could give rise to a non negligible background in the region of interest of the spectrum.

The difficulty in detecting the possible very small traces of this isotope in detectors with implanted ^{163}Ho (an $^{166\mathrm{m}}$Ho activity smaller than 100 nBq is expected in each detector) makes a Monte Carlo simulation necessary in order to determine the shape of the induced background in the region of interest around 2.5–3.0 keV. This information can then be used to reduce the systematic uncertainty due to not detecting any $^{166\mathrm{m}}$Ho signature.

A code based on GEANT4 has been developed to study the effect of $^{166\mathrm{m}}$Ho contamination in detectors. For this simulation, the geometry of a single detector was modeled including a gold absorber of size 190 μm $\times$ 190 μm $\times$ 10 μm connected by small gold stems, 5 μm thick and having a diameter of 20 μm, to the **Au**:Er sensor of size 190 μm $\times$ 190 μm $\times$ 1.3 μm. The $^{166\mathrm{m}}$Ho was placed in the middle plane of the absorber and its decay was handled by the *G4RadioactiveDecay* physical process which has been modified to correct for the description of the metastable states.

Figure 27 (Left) shows the simulated calorimetrically measured spectrum due to 10^6 $^{166\mathrm{m}}$Ho decays occurring within the absorber. The various β^--decay branches of $^{166\mathrm{m}}$Ho are clearly visible. Figure 27 (Right) shows a magnification of the full spectrum into the first 10 keV. An almost flat spectrum is observed across this energy range with, in average, 40 counts/ 10 eV/ 10^6 primary events, i.e. a fraction of 4×10^{-5} of all $^{166\mathrm{m}}$Ho decays will be found within a 10 eV bin around the region of interest. An

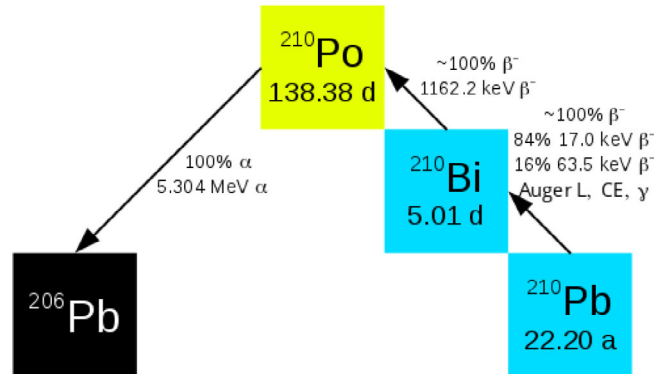**Fig. 28.** Decays of ^{210}Pb and its daughter nuclei.

experiment to validate these results is planned where ^{166m}Ho is implanted in an MMC detector designed for the ECHo experiment. Already at this stage, an estimation can be given for the upper limit for the ratio of the number of ^{166m}Ho atoms with respect to the number of ^{163}Ho atoms, R, which is required for the first two phases of the ECHo experiment. In ECHo-1k an experiment is planned which will last about one year using 100 detectors, each with about 10 Bq ^{163}Ho for a total activity of about 1000 Bq. For this measurement, about 15 ^{163}Ho events are expected in the last 10 eV of the ^{163}Ho spectrum. By asking that the counts in these last 10 eV due to ^{166m}Ho decays are 10 times smaller than the statistical fluctuation of the ^{163}Ho events, we obtain $R < 5 \times 10^{-8}$. For the second phase of the experiment, ECHo-1M, the requirement will be $R < 5 \times 10^{-9}$. This suppression of ^{166m}Ho with respect to ^{163}Ho can be reliably obtained with the planned optimized procedures for the physical purification of the ^{163}Ho source by means of mass separation techniques, as discussed in Section 7.4.

8.5 ^{210}Pb and its decay products

Among natural occurring radioactive nuclides, an isotope of special interest is ^{210}Pb ($T_{1/2} = 22.2$ a, $Q_{\beta^-} = 63.5$ keV). Figure 28 shows the decay scheme of ^{210}Pb. This lead isotope is produced in the decay of the gaseous ^{222}Rn which is present in nature being part of the uranium-radium decay chain. ^{222}Rn can be adsorbed on surfaces and therefore ^{210}Pb is present on detector components after storing them at the air. Additionally, the bulk material used in the construction could contain traces of ^{210}Pb from the decay of predecessors in the material itself. ^{210}Pb is a rather low energy β^--emitter with two branches, one with 84 % branching ratio (BR) having $Q = 17$ keV and $E_{\beta_\mathrm{mean}} = 4.16$ keV while the other one having $Q = 63.5$ keV and $E_{\beta_\mathrm{mean}} = 16.16$ keV [128]. The first branch is accompanied by the emission of 46.54 keV of energy in the form either of a γ-ray or conversion electrons (CE).

The detector response to ^{210}Pb contaminations was studied with a GEANT4 Monte Carlo simulation. The used geometrical setup is the same as in the case of the simulation of ^{166m}Ho presented in Section 8.4, but the ^{210}Pb nuclei where uniformly distributed throughout the volume of the detector. Since the energy of the decay is so small, the approximate allowed contamination for a given background level of decays on the surface of the detector is twice the maximum allowed bulk contamination.

We simulated one million primary ^{210}Pb decays, followed by the subsequent decays of the daughter nuclei ^{210}Bi (β^-) and ^{210}Po (α). The energy depositions of ^{210}Pb
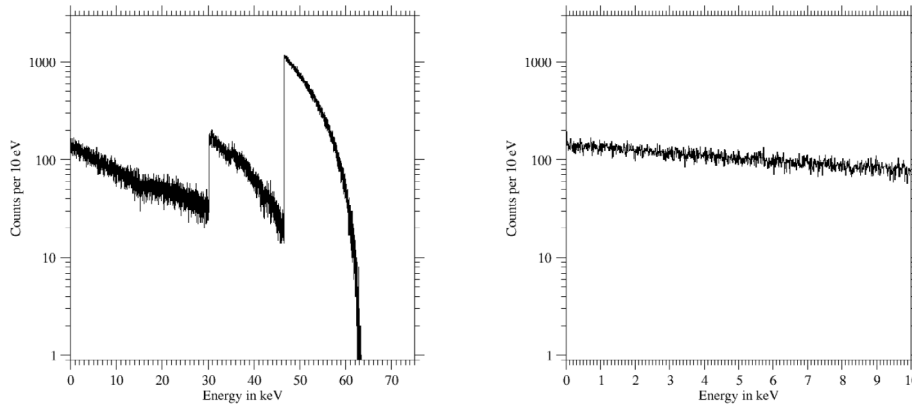
Fig. 29. (Left) Total deposited energy in the detector within 1 ms after the ^{210}Pb decay. (Right) Deposited energy in the detector up to 10 keV within 1 ms after decay of ^{210}Pb.

decays and the daughter nuclei were registered, where energy depositions within a time window of 1 ms were treated as a single event to account for pile-up effects. The deposited energy in the detector is shown in Figure 29. The background in the ROI, between 0 keV and 10 keV, is very slowly decreasing with energy.

The activity of ^{210}Pb, which would lead to a background at the level of 50% of the expected ^{163}Ho signal in the last 10 eV below the Q_{EC}-value, would be $A_{210\text{Pb}} = 5$ mBq for ^{210}Pb atoms enclosed in all the absorbers (or 10 mBq for contaminations sitting on the surface of all the absorbers). Such a level of contamination is well beyond typical values of ^{210}Pb concentration in the material used for the detector fabrication. On the other hand, dedicated procedures for handling and storing detectors, readout components and experimental holders will be defined to reduce the ^{222}Rn contamination of the surfaces. Therefore, we expect that the background level due to ^{210}Pb in the ^{163}Ho spectrum will be negligible and well below the unresolved pile-up level.

8.6 ^{40}K as surface contamination

Another naturally occurring nuclide which could strongly contribute to the background in the energy range around the endpoint of the ^{163}Ho spectrum is ^{40}K. This is an odd-odd nuclide and can decay either via EC or positron emission to ^{40}Ar in 11% of the cases or via beta process to ^{40}Ca in the rest of the cases, as shown in Figure 30. The half-life of ^{40}K is $T_{1/2} = 1.248$ Ga and the energy available to the decay to ^{40}Ar is $Q_{EC} = 1.504$ MeV while the energy available to the decay to ^{40}Ca is $Q_\beta = 1.311$ MeV. It is clear that electrons emitted during the beta decay of ^{40}K, either in the detector volume or in the close vicinity, could be partially or completely stopped in the detector itself and therefore generate events which could be in the energy range of the ^{163}Ho spectrum. Looking at the EC process in ^{40}K, the characteristic γ-photons with energy $E_\gamma = 1.46$ MeV, would hardly lead to background events in the interesting energy region. X-rays and electrons generated during the de-excitation of the daughter atom ^{40}Ar are in the range below 3 keV. The decay modes of ^{40}K are presented in Figure 31.

The main contributions at very low energies are dominated by the EC branch of the decay. The spectrum of the β-decay branch peaks at much higher energies and leaves only a residual flat background in the region of interest. For a contamination sitting right on top of the detector or on an adjacent surface, it is possible that the
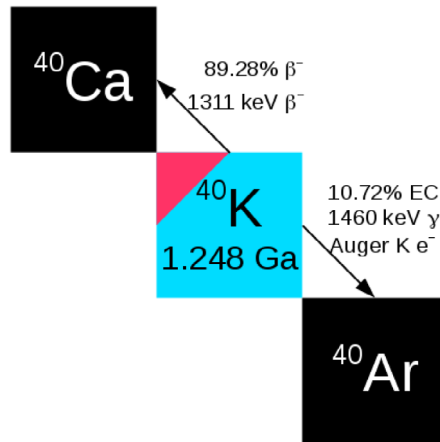
1668 The European Physical Journal Special Topics

Fig. 30. Simulated decay modes of ^{40}K. The main decay branch with a branching ratio (BR) of 89.28% is the β^- decay to ^{40}Ca with an endpoint energy of 1311.07 keV. The electron capture decay to ^{40}Ar has a BR of 10.72% and a Q_{EC} value of 1504.69 keV. The energies of the various Auger electrons are found between 2.5 to 3.1 keV. The rare β^+ decay branch of ^{40}K has been omitted from this schematic.
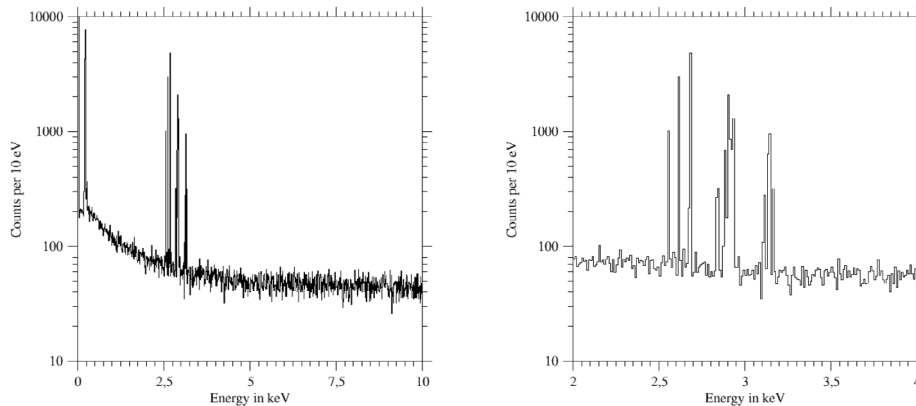

Fig. 31. Decay modes of ^{40}K. Left: deposited energy within an energy window between 0 keV and 10 keV. Right: deposited energy in the region around the endpoint of the ^{163}Ho spectrum, from 2 keV to 4 keV from decays of ^{40}K positioned above the surface of the detector. The different Auger lines in the aftermath of the EC decay are clearly visible.

detector will stop just the Auger electrons or the X-rays from the de-excitation of the atomic shells. If this is the case, on top of a flat background contribution the lines from the various Auger electrons and x-rays will be seen.

X-rays are expected at 2.955 keV (Ar K$_{\alpha2}$, 3.7% per K shell vacancy) and 2.957 keV (Ar K$_{\alpha1}$, 7.4% per K shell vacancy). The energies of the most intense Auger electron lines are at 2.707 keV (Ar K-L$_2$ L$_3$, 30%) and 2.709 keV (Ar K-L$_3$ L$_3$, 17%). Weaker lines from Auger de-excitations are expected around 2.553 keV, 2.63 keV, 2.86 keV, 2.94 keV and 3.16 keV [130].

The detector setup described in Section 8.4, without ^{166m}Ho, was used for the simulation of one million decays of ^{40}K atoms which were uniformly distributed on the surface of the detector. The resulting spectrum of the energy deposited in the detector is shown in Figure 31. On top of a flat background due to Compton scattering

and incomplete energy deposition of escaping particles, the expected lines from Auger electrons are clearly visible. While a good overall agreement is found for the relative branching ratios of the Auger electrons and X-rays with respect to the published values, the energies of the Auger electrons are a few eV lower in the simulated spectra. This deviation does not affect the estimation of the allowed contamination level.

From the simulation we could deduce that about 6 mBq of ^{40}K on top of all detectors are sufficient to result in a flat background signal in the ROI, 10 eV below the Q_{EC}-value, with 50% of the expected ^{163}Ho signal strength. In this case, the peak from the Ar K-LM Auger electrons at 2.864 keV contains twice as many counts as expected from the ^{163}Ho signal. The lines around 2.95 keV from the Ar$_{K\alpha}$ X-rays and Auger electrons are expected to be about 5–8 times above the expected signal.

In case of the ECHo-1K detector configuration, the above mentioned activity corresponds to 200 µg of natural potassium left directly on all the 100 detector surfaces during the production and setup assembly. To reach this amount of potassium to be distributed all over the detectors is extremely difficult, but special attention in handling the different parts of the detector setups should be taken.

Upper limits for the ^{40}K contamination on parts in close vicinity of the detector modules are difficult to simulate since the exposure of the detectors depends crucially on the distribution of ^{40}K. Surface contaminations contribute according to the solid angle under which the detectors appears. Generally, bulk contaminations in the materials composing the surrounding of the detectors are irrelevant since the Auger electrons are effectively stopped.

The contamination of ^{40}K both in the detector volume as in the components present in the detector setup should be reduced and kept under control in order to estimate the contribution of the corresponding background in the ^{163}Ho spectrum. The contribution to the background in the ^{163}Ho spectrum due to ^{40}K bulk and surface contamination will be defined by performing Monte Carlo simulation where ^{40}K contaminations are located in well defined positions of the setup. This analysis will be used to define and reduce the systematic uncertainties due to a not clear signal of ^{40}K structures in the spectrum. Therefore, for the case of ^{40}K, as we discussed for the case of ^{210}Pb, we do not expect a major contribution to the ^{163}Ho spectrum due to the Auger electrons lines. Nevertheless, it will be of utmost importance to monitor the presence of ^{40}K in the different part constituting the detector setups.

9 Independent measurement of Q_{EC}

9.1 High-precision Penning-trap mass spectrometry

Precise knowledge of the Q_{EC}-value of the EC in ^{163}Ho is demanded for a successful realization of the ECHo experiment. Since the ECHo project is chronologically divided into several phases, the required precision in the Q_{EC}-value determination is defined by a particular phase of this experiment. For the development of the first phase, it is desirable to know the Q_{EC}-value with an uncertainty of a few ten eV. This will help to fix the scale of the experiment and enable a determination of the neutrino mass below 10 eV/c^2 from the analysis of the microcalorimetric de-excitation spectrum of the EC in ^{163}Ho. In a second phase, the goal will be to reach a sensitivity on the electron neutrino mass on a sub-eV level. At this stage it is important to have a direct independent measurement of the Q_{EC}-value with an uncertainty of approximately 1 eV.

Nowadays, the only technique which is capable of directly measuring the Q_{EC}-value of the EC in ^{163}Ho with the required uncertainty is high-precision Penning-trap mass spectrometry (PTMS) [131,132]. The Q_{EC}-value is the mass difference of the

initial and final states of the transition:

$$\frac{Q_{\mathrm{EC}}}{c^2} = m_{\mathrm{Ho}} - m_{\mathrm{Dy}} = m_{\mathrm{Dy}} \left(\frac{m_{\mathrm{Ho}}}{m_{\mathrm{Dy}}} - 1 \right) = m_{\mathrm{Dy}} \left(R - 1 \right), \tag{8}$$

where m_{Ho} and m_{Dy} are the atomic masses of ^{163}Ho and ^{163}Dy, respectively, and R is the ratio of the masses of ^{163}Ho and ^{163}Dy. Remarkably, in order to determine the Q_{EC}-value of the EC in ^{163}Ho on 1 eV level, it is sufficient to know the mass of ^{163}Dy with an uncertainty of 65 MeV. Thus, a precise determination of this Q_{EC}-value reduces to a high-precision measurement of the ratio R of two masses since the absolute mass of ^{163}Dy is well known enough [19].

The superiority of high-precision Penning-trap mass spectrometry over other mass measurement techniques is based on the fact that in a Penning trap the mass m of a nuclide is determined by measuring the free cyclotron frequency ν_c of the nuclide ion of charge q in a strong static homogeneous magnetic field B:

$$\nu_c = \frac{1}{2\pi} \frac{q}{m} B. \tag{9}$$

In order to reach a sub-ppb uncertainty in the cyclotron-frequency determination, the ion must be confined to a well-localized volume within the homogeneous magnetic field for at least some seconds. This is achieved by a superposition of a static three-dimensional quadrupole electric field on the magnetic field such that an electrostatic potential well along the magnetic field lines is created. Such a configuration of fields is called a Penning trap. An exhaustive overview of the theory of the Penning trap can be found in [133].

The presence of the electrostatic quadrupole field modifies the pure ion's cyclotron motion to three independent trap motions: modified cyclotron, magnetron and axial motions with the frequencies ν_+, ν_- and ν_z, respectively. Although none of these frequencies are simple functions of the ion's mass, the invariance theorem [134] gives a simple relation between the pure cyclotron and the trap frequencies:

$$\nu_c^2 = \nu_+^2 + \nu_-^2 + \nu_z^2. \tag{10}$$

In Penning-trap mass spectrometry of radioactive nuclides the cyclotron frequency is determined from [135]:

$$\nu_c = \nu_+ + \nu_-. \tag{11}$$

The latter approach is used for mass measurements on short-lived nuclides with uncertainties larger than 10^{-10}, whereas the former method is chosen for mass-difference measurements on long-lived and stable nuclides with relative uncertainties below 10^{-10}.

The ratio of free cyclotron frequencies of two particles with the same charge state in the same magnetic field is equal to the ratio of their masses. When an ion with well-known mass is taken as reference the mass of the second ion is immediately obtained. Obviously, carbon ions as defining particles for the atomic mass scale (apart from small corrections by the electron mass and its binding energy with respect to neutral carbon) would be best suited as reference. Since it is of advantage to have the cyclotron frequencies of the unknown and the reference ion at similar values singly charged carbon clusters with different number of atoms [136] are routinely used for reference.

There are three methods in use to measure the cyclotron frequency: (1) via detection of the image current induced by the ion's motion in the resonant tank circuit attached to the trap (Fourier-Transform Ion-Cyclotron-Resonance (FT-ICR) method) [137], (2) with the so-called Time-of-Flight Ion-Cyclotron-Resonance technique
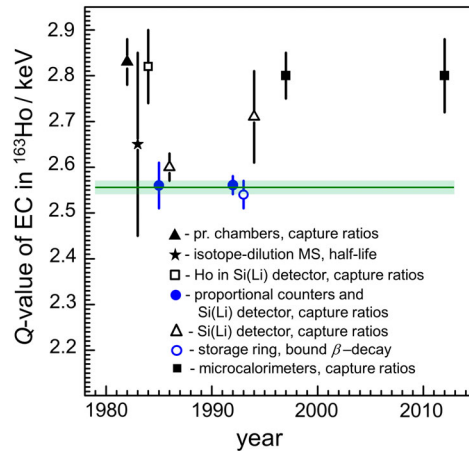
Fig. 32. The Q_{EC}-value of the EC in ^{163}Ho taken from [19] and obtained by different groups from the analysis of the electron-capture spectrum [16,18,20–22,27,30,31,147–149]. Different symbols indicate different experimental methods. The green line and shaded band correspond to the recommended Q_{EC}-value and its uncertainty, respectively [19]. The recommended Q_{EC}-value was obtained by averaging only the data points which are colored blue in the plot. Figure reproduced from [23]. (This figure is subject to copyright protection and is not covered by a Creative Commons license.)

(ToF-ICR) from the measurement of the time of flight of the ion through the strong gradient of the magnetic field [135,138–140] and (3) with the Phase-Imaging Ion-Cyclotron-Resonance technique (PI-ICR method) [141,142].

Until now, the ToF-ICR technique has been the method of choice to determine masses of short-lived nuclides. With this method it is feasible to reach a ppb-uncertainty in the mass determination of short-lived nuclides. The novel PI-ICR technique, which has recently been developed at SHIPTRAP [143], extends the achievable precision to a level of few parts in 10^{10} [141,142]. Thus, a relative mass uncertainty of few parts in 10^{10} will soon become routinely achievable even for short-lived nuclides at a wide variety of Penning-trap facilities.

The FT-ICR method is used or is planned to be used to measure the cyclotron frequency ν_c with an ultimate relative uncertainty of below 0.01 ppb at such ultra-precise Penning-trap mass spectrometers as the FSU trap [144], the THe-Trap [145], HCI [146] and PENTATRAP [121].

9.2 Determination of the Q_{EC}-value of the EC in ^{163}Ho with the Penning-trap mass spectrometer SHIPTRAP

One of the first goals of the ECHo collaboration was to obtain a direct measurement of the Q_{EC}-value on a few tens of eV to solve the controversy due to the discrepancy among old measurements. In particular, the Q_{EC}-values have been only indirectly obtained, from the analysis of the EC-spectrum in several independent experiments by different groups using different methods (Fig. 32) [16,18,20–22,27,30,31,147–149]. The results scatter by a few hundred eV from approximately 2.5 keV to 2.9 keV. The microcalorimetric Q_{EC}-values obtained with cryogenic microcalorimetry [21,22] are higher by about 250 eV than the recommended Q_{EC}-value of 2555(16) eV of the Atomic-Mass Evaluation AME2012 [19], which has been obtained by averaging only proportional counter data [31,147] and storage-ring measurements [149]. Recently, a first direct measurement has been performed using the Penning-trap setup
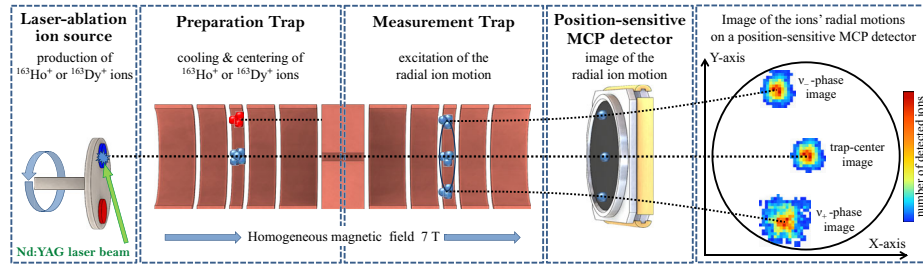
Fig. 33. Schematic of off-line SHIPTRAP with the PI-ICR technique used for the determination of the Q_{EC}-value of the EC in ^{163}Ho (see text for details). Figure reproduced from [179].

TRIGATRAP [150], however, with an uncertainty of 700 eV [120], which is insufficient to resolve this controversy. If the recommended Q_{EC}-value would be correct, then the large deviation of the values obtained using microcalorimetric techniques may hint to an insufficient understanding of the corresponding measurements of the EC spectrum, i.e. of the de-excitation processes involved in the EC in ^{163}Ho.

The presently most precise determination of the Q_{EC}-value has been performed with the Penning-trap mass spectrometer SHIPTRAP by employing the PI-ICR technique [141,142]. SHIPTRAP is located at GSI-Helmholtz center for heavy ions in Darmstadt. This Penning-trap mass spectrometer has the aim for direct high-precision mass measurements on short-lived nuclides. A detailed description of the whole project and its achievements can be found in [143]. Here only the part of the facility, for short off-line SHIPTRAP, relevant to the measurement of the Q_{EC}-value is shown in Figure 33. It consists of a Nd:YAG laser-ablation ion source [151] for production of singly charged ions from neutral species in various chemical forms, an ion optical system and the heart of the apparatus- the Penning-trap mass spectrometer.

The ^{163}Ho and ^{163}Dy ions were produced by laser-irradiating ^{163}Ho and ^{163}Dy samples in powder form spread over a 5×5 mm^2 large titanium plates. ^{163}Ho was first produced in the high-flux reactor of the Institut Laue-Langevin in Grenoble and then chemically separated via ion-chromatography optimized to separate neighboring lanthanides (see Sect. 7.3). The series of electrostatic electrodes and Einzel lenses transport the ions from the ion sources towards the Penning-trap mass spectrometer.

The Penning-trap mass spectrometer has two cylindrical Penning traps – the preparation trap (PT) and measurement trap (MT) – placed in a magnetic field of 7 T created by a superconducting magnet. The PT serves for separating the ions of interest from unwanted ions by employing the mass-selective buffer gas cooling technique [152]. For this the PT is filled with a helium gas at a pressure of a few 10^{-5} mbar. By applying rf-fields of certain multipolarity at chosen frequencies to the electrodes of the PT [153], only the nuclide of certain mass can be allowed to pass into the MT. In the MT a measurement of the cyclotron frequency of the chosen nuclide takes place via the PI-ICR technique. More details about the measurement procedure of the Q-value of the EC in ^{163}Ho is presented in [23].

The final frequency ratio R and the corresponding mass difference between ^{163}Ho and ^{163}Dy, the Q_{EC}-value, with their statistical and systematic uncertainties are $R=1.000\,000\,018\,67(20_{stat})(10_{sys})$ and $Q_{EC}=2833(30_{stat})(15_{sys})$ eV/c^2, respectively. Our result for the atomic mass difference of ^{163}Ho and ^{163}Dy deviates by more than seven sigmas experimental uncertainty from the accepted value of the Atomic-Mass Evaluation AME2012 [19] while being in perfect agreement with the microcalorimetric measurements: $Q_{EC} = 2800(50)$ eV [21] and $Q_{EC} = 2800(80)$ eV [22] (see Fig. 32).
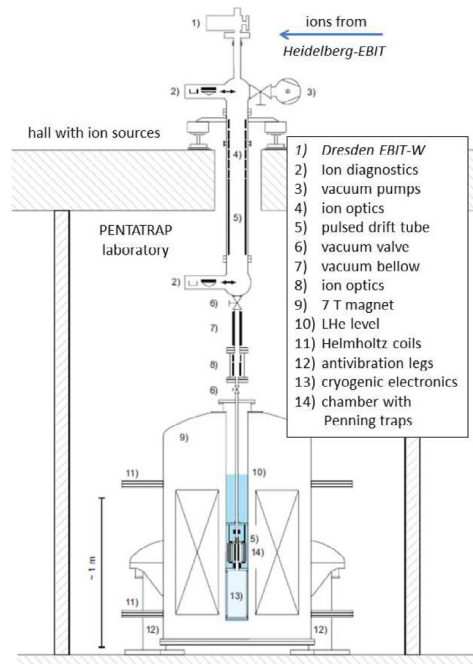
Fig. 34. Schematic of PENTATRAP. The experiment is situated on two levels. On the upper level there are two ion sources for a production of highly charged ions – Dresden- and Heidelberg-EBITs. The Penning-trap mass spectrometer is located on the lower level in the PENTATRAP laboratory. The ion beamline, which interfaces the ion sources and the mass spectrometer, consists of a set of electrostatic Einzel lenses, pulsed drift tubes and ion diagnostics. Figure slightly modified from [121].

Thus, on the level of the present accuracy there are no unexpected deviations due to systematic effects of cryogenic microcalorimetry or of the theoretical description of the spectrum.

The realization of the ultimate goal of the ECHo project – the determination of the neutrino mass on a sub-eV level – requires a direct measurement of the Q_{EC}-value of the EC in ^{163}Ho with an unprecedentedly low uncertainty of approximately 1 eV. Presently, there are no means to perform such a precise measurement. This will become possible with the Penning-trap mass spectrometer PENTATRAP, which is currently being built at the Max-Planck Institute for Nuclear Physics, Heidelberg (Fig. 34) [121,154].

10 Parameterization of the electron-capture spectrum for ^{163}Ho atoms and implications on the neutrino mass

The electron-neutrino mass affects the energy spectrum of electron capture processes [28,29,41]. As already discussed, nowadays ^{163}Ho is considered the best isotope to be used in experiments for the determination of the absolute scale of the electron-neutrino mass by the analysis of the calorimetrically measured electron-capture spectrum. To be able to identify the effect of sub-eV neutrino masses, a precise and reliable description of the de-excitation processes in the region close to the end point

of the capture spectrum is of paramount importance. For many years only so-called first-order transitions with one hole in the atomic shells of the formed [163]Dy have been included in the calculations for the [163]Ho spectrum. Given the modest energy resolution of the detectors used in early days, the agreement between theory and data was quite good. The electronic part of the parameters describing the [163]Ho spectrum for first-order transitions have recently been re-calculated adopting the fully relativistic Dirac-Hartree-Fock (DHF) method for describing the initial- and the final-state orbitals [41], including a self-consistent consideration of the corresponding final-state holes within the DHF iterations. Since the orbitals of the initial and the final states are calculated for different atomic systems, the so-called overlap corrections are automatically incorporated. Similarly, the exchange corrections due to the Pauli principle are fully accounted for, as the matrix elements between the Slater determinants describing the initial and the final states were calculated using the formalism of many-body second quantization. Furthermore, the finite nuclear size was considered in the DHF orbital calculation as well as in the evaluation of the (single-electron) matrix element describing the nuclear capture of an electron by the proton. In more detail, the nuclear charge distribution for the parent and the daughter atoms were included. The Gamow-Teller transition of the proton into the neutron and the bound electron into the continuum neutrino incorporates an integration over the nucleus with the weight r^2. The value of the electronic wave function at the surface of the nucleus is used instead of the one at the origin (as used in all previous works). This is a better approximation. However, even this calculation and thus the underlying model was shown to be not precise enough for the description of the data obtained in high-energy-resolution measurements performed within the ECHo experiment. In Section 5, the discrepancy between the measured [163]Ho spectrum and the expected shape calculated including only first-order excited states in [163]Dy was discussed.

In 2014, Robertson [37] considered the possibility that also higher-order excitation processes, characterized by the creation of more than one hole during the electron capture, could lead to visible structures in the calorimetrically measured [163]Ho spectrum. In particular, that work focused on the case of excitations with two holes in the formed excited [163]Dy atom. The second hole is created by shake-up processes which occur simultaneously to the electron capture. In fact, as is discussed in more detail below, the occurrence of these processes is a consequence of the fact that the spectator electrons cannot follow adiabatically the capture process. To provide a first estimate of the probabilities for such processes, results by Carlson and Nestor [155,156] which were determined for xenon, having $Z = 54$, were used. Even in this relatively rough approximation, the theoretical electron-capture spectrum showed the presence of additional Breit-Wigner resonances due to the two-hole excited states in different parts of the spectrum and, in particular, in the range between 400 eV and 600 eV where the excess of counts have been seen experimentally.

These first preliminary results have motivated more refined calculations. In [38] a completely relativistic method, extending the one developed and applied for the calculation of the one-hole transition matrix elements in [41], was used to calculate the probabilities that excited states characterized by two holes are populated in dysprosium following the electron capture process in [163]Ho. Also these two-hole probabilities were calculated with the fully relativistic DHF code of Grant [157], Desclaux [158], and Ankudinov et al. [159] with the full antisymmetrization in the atoms holmium and dysprosium accounted for. In the calculation of the probabilities for the second electron hole in dysprosium the $n\,s_{1/2}$ or $n\,p_{1/2}$ $(n \geq 3)$ one-hole states are included self-consistently in the DHF iteration. Thus for each one-hole state in dysprosium a fully self-consistent DHF iteration with a hole in the different orbitals is performed

for all the electrons in the atom. Finally, the same framework was adopted to consider also three-hole final states [24].

10.1 Electron capture of ^{163}Ho

Assuming the validity of the sudden approximation for the electron-capture process, the probability of populating a specific final state $|\Upsilon_f\rangle$ of ^{163}Dy, if the parent ^{163}Ho was initially in its ground state $|\Upsilon_0\rangle$ is

$$\mathcal{P}_f \ \propto \ g(m_\nu^2, Q_{\mathrm{EC}} - E_f) \ \left| \langle \Upsilon_f | \hat{V}_W | \Upsilon_0 \rangle \right|^2 \tag{12}$$

where $\hat{V}_W$ is the weak-interaction operator and g is the kinematic phase-space factor that depends on (the square of) the neutrino mass m_ν and the energy available to the neutrino, i.e. the difference between the energy release of the capture process Q_{EC} and the energy E_f left in the remaining system if formed in state Υ_f. It is given by

$$g(m_\nu^2, Q_{\mathrm{EC}} - E_f) = (Q_{\mathrm{EC}} - E_f)\sqrt{(Q_{\mathrm{EC}} - E_f)^2 - m_\nu^2 c^4} \ \Theta(Q_{\mathrm{EC}} - m_\nu c^2 - E_f) \tag{13}$$

where $Q_{\mathrm{EC}} = (M_{^{163}\mathrm{Ho}} - M_{^{163}\mathrm{Dy}})\, c^2$ is the mass difference between parent and daughter atom. The Heaviside function Θ takes care of the energy balance, limiting the accessible final states to those with energies $E_f \leq Q_{\mathrm{EC}} - m_\nu c^2$. In the case of ^{163}Ho this condition allows only for the capture of electrons with main quantum number $n \geq 3$. Often, the Heaviside function is omitted and the energy conservation is tacitly assumed.

Due to the different intrinsic time scales of nucleonic and electronic motion, the total wave functions Υ_0 and Υ_f are well approximated by a single product of a nuclear wave function χ and electronic wave functions Φ or Ψ, i.e. one finds $|\Upsilon_0\rangle \approx |\Psi_0 \chi_0\rangle$ and $|\Upsilon_f\rangle \approx |\Phi_f \chi_f\rangle$. In the simplest (additional) approximation, the electronic wavefunction of the Z-electron parent atom is expressed as a single product of orbitals ψ, $\Psi_0(\mathbf{r}_1, \mathbf{r}_2, \ldots \mathbf{r}_Z) \approx \psi_1(\mathbf{r}_1)\psi_2(\mathbf{r}_2)\cdots\psi_Z(\mathbf{r}_Z)$. The indices of the orbitals denote the set of atomic quantum numbers n, ℓ, m, s (main quantum number n, angular momentum ℓ, magnetic quantum number m, and spin s) according to $j \equiv \{n_j, \ell_j, m_j, s_j\}$ or, as is more appropriate for a heavy atom like Ho and Dy the spin-orbit coupled basis states, $j \equiv \{n_j, \ell_j, J_j, m_{J_j}\}$. Since in the electron-capture process a bound electron and a proton transform into a neutron and a neutrino, the daughter atom possesses $Z - 1$ electrons as well as nuclear charge $Z - 1$. Using the same level of approximation as was adopted for the initial state, the final-state electronic wavefunction is $\Phi_f^{(j)}(\mathbf{r}_1, \mathbf{r}_2, \cdots, \mathbf{r}_{j-1}, \mathbf{r}_{j+1}, \cdots \mathbf{r}_Z) \approx$ $\phi_{f_1}(\mathbf{r}_1)\phi_{f_2}(\mathbf{r}_2)\cdots\phi_{f_{j-1}}(\mathbf{r}_{j-1})\phi_{f_{j+1}}(\mathbf{r}_{j+1})\cdots\phi_{f_Z}(\mathbf{r}_Z)$, if electron j was captured.

Due to the short range of the weak interaction, the capture process requires the bound electron to possess a non-zero probability density at the nucleus. Ignoring the finite size of the nucleus, this effectively reduces the action of $\hat{V}_W$ onto the electronic wavefunction to a delta function for the captured electron j at the origin, $\delta(\mathbf{r}_j)$, and allows for a factorization of the transition amplitude,

$$\mathcal{P}_f^{\mathrm{prod}} \ \propto \ g(m_\nu^2, Q_{\mathrm{EC}} - E_f) \, C_f \ |\psi_j(0)|^2 \ P_f^{\mathrm{prod}} \tag{14}$$

with
$$P_f^{\text{prod}} = \big| \langle \phi_{f_1}\phi_{f_2}\cdots\phi_{f_{j-1}}\phi_{f_{j+1}}\cdots\phi_{f_Z} | \psi_1\psi_2\cdots\psi_{j-1}\psi_{j+1}\cdots\psi_Z \rangle \big|^2 \qquad (15)$$

and where $C_f = \left| \langle \chi_f | \hat{V}_W | \chi_0 \rangle \right|^2$ is the nuclear transition probability. Furthermore, it has been used that a bound-state wavefunction ψ can always be chosen to be purely real. In an improved description, the finite size of the nucleus is accounted for. As a result, the electronic wavefunction of the captured electron is not calculated at the centre-of-mass of the nucleus using a δ function, but may be integrated explicitly over the nuclear volume or, at least, it may be calculated at the nuclear surface R as is done in [41]. The inclusion of the finite-size of the nucleus does, however, not only modify the prefactor, $\psi_j(R)$ instead of $\psi_j(0)$, but also allows for the capture from orbitals that otherwise would be symmetry forbidden. In fact, for all orbitals except the ones of s or $p_{1/2}$ symmetry one finds $\psi_j(0) = 0$. On the other hand, $\psi_j(R \neq 0)$ yields non-zero prefactors and thus allows for capture from orbitals with other symmetries, though evidently with much smaller probability.

A further simplification is achieved, if it is assumed that the orbitals of the daughter atom agree with those of the parent atom, i.e. $\phi_i \approx \psi_i$. Within this assumption the orthogonality of the orbitals enforces that the capture of an electron from a specific orbital j necessarily can only result in a single final state f ($P_f^{(0)} = 1$) with population probability

$$\mathcal{P}_f^{\phi=\psi} \propto g(m_\nu^2, Q_{\text{EC}} - E_f)\, C_f\, |\psi_j(R)|^2. \qquad (16)$$

In this final state all but the captured electron remain in their unchanged initial orbitals. Compared to the daughter atom in its electronic ground state there is thus a hole in the orbital j from which the electron was captured while there is an additional electron in the outermost orbital, provided the captured electron was not one from this outermost orbital. This configuration is $\Phi_0^{(j)}(\mathbf{r}_1, \mathbf{r}_2, \cdots, \mathbf{r}_{j-1}, \mathbf{r}_{j+1}, \cdots, \mathbf{r}_Z) = \phi_1(\mathbf{r}_1)\phi_2(\mathbf{r}_2)\cdots\phi_{j-1}(\mathbf{r}_{j-1})\phi_{j+1}(\mathbf{r}_{j+1})\cdots\phi_Z(\mathbf{r}_Z)$ and thus characterized by $f_i = i$ for $i = 1, 2, \ldots, j-1, j+1, \ldots, Z$. As a consequence, all final states (except the one that is equal to the ground state of the daughter atom) are metastable against non-radiative decays, like, e.g., Auger processes, or radiative relaxation processes. If all decay processes of a given final state can be subsumed under a single exponential decay rate, this exponential decay in time leads to a Lorentzian shape in the energy domain. Therefore, even in this simplest approximation the electron-capture spectrum, i.e. the calorimetrically measured energy distribution of all particles but the neutrino, is not simply a set of discrete peaks as one could expect from equation (16) after considering the capture from all initially occupied spin orbitals $j \in$ occ, but given as

$$\frac{\mathrm{d}N^{\phi=\psi}}{\mathrm{d}E_C} \propto g(m_\nu^2, Q_{\text{EC}} - E_C) \sum_{j \in \text{occ}} C_j\, |\psi_j(R)|^2\, \frac{(2\pi)^{-1}\,\Gamma_j}{(E_C - E_j)^2 + (\Gamma_j^2/4)}. \qquad (17)$$

Thus the spectrum recorded as a function of the continuous energy E_C is given as a sum over Lorentzian peaks that are centered at $E_C = E_j$ where E_j is the energy difference between the initial ^{163}Ho and the final ^{163}Dy atoms if an electron from orbital j was captured. Within the approximation of adopting the same orbitals for both atoms ($\phi_i \approx \psi_i$) these energies are simply given by the orbital energies ϵ_j of the captured electron, $E_j = \epsilon_j$ in equation (17).

The approximation $\phi_i \approx \psi_i$ leading to equation (16) ignores evidently the fact that the orbitals of a neutral atom with nuclear charge Z differ from those for an atom with $Z - 1$. While it is a reasonable zeroth-order approximation to adopt the

same orbitals for parent and daughter atoms, especially for large values of Z, a more careful calculation must account for the difference of the orbitals and thus return to equation (14). With the assumption that nevertheless all but the captured electron are pure "spectators" and thus all of their quantum numbers remain the same, one finds

$$\mathcal{P}_f^{\text{prod}} \;\propto\; g(m_\nu^2, Q_{\text{EC}} - E_f)\, C_f\, B_j^{\text{ovl}}\, |\,\psi_j(R)\,|^2 \tag{18}$$

with the overlap correction factor

$$
\begin{aligned}
B_j^{\text{ovl}} \equiv P_j^{\text{prod}} &= |\,\langle\,\phi_1\,|\,\psi_1\,\rangle\langle\,\phi_2\,|\,\psi_2\,\rangle \ldots \langle\,\phi_{j-1}\,|\,\psi_{j-1}\,\rangle\langle\,\phi_{j+1}\,|\,\psi_{j+1}\,\rangle \ldots \langle\,\phi_Z\,|\,\psi_Z\,\rangle\,|^2 \\
&= \prod_{i \in \text{occ}\backslash j} |\langle\,\phi_i\,|\,\psi_i\,\rangle|^2\,.
\end{aligned}
\tag{19}
$$

Equation (19) implies, however, yet an additional approximation, since it assumes that the set of orbitals of the daughter atom, $\{\phi_j\}$, is the same for every final state. A natural choice seems to be the orbitals obtained within some (relativistic) Hartree-Fock or density-functional-theory calculation for the ground state of the daughter atom. However, depending on the orbital from which an electron is captured the remaining (spectator) electrons experience a different electronic cloud and thus a different mean-field potential. This is, e.g., evident from the fact that obviously the screening of the nucleus is different in the case of a hole in a very deeply lying orbital with angular momentum $\ell = 0$ or a hole in a valence shell, possibly even with $\ell > 0$. Therefore, a better approximation is achieved, if the orbitals are calculated self-consistently for the different hole states that occur for capturing electrons from different orbitals j [41]. In other words, for every hole j there is one full set of orbitals $\{\phi_i^{(j)}\}$.

Above, the many-electron wavefunctions Ψ and Φ of the parent and the daughter atoms, respectively, were approximated by a simple product of one-electron wave functions (orbitals). Clearly, this approximation ignores the fact that the atomic electrons are indistinguishable and thus have to obey the Pauli principle. A more proper description is thus the one in which the many-electron wave functions are each represented by a Slater determinant (SD), i.e. $|\,\tilde{\Psi}_0\,\rangle$ and $|\,\tilde{\Phi}_0^{(j)}\,\rangle$. This does not only lead to the occurrence of exchange terms within the orbital calculation itself, for example in a Hartree-Fock calculation, but also in the calculation of the transition probabilities in equation (12). The occurrence of the exchange term for the transition matrix element may be illustrated using the example of a two-electron system. In this case the initial state in the product approximation is $|\,\psi_1(1)\,\psi_2(2)\,\rangle$ while the properly antisymmetrised state would be $2^{-1/2}\,(|\,\psi_1(1)\,\psi_2(2)\,\rangle - |\,\psi_2(1)\,\psi_1(2)\,\rangle)$. Assuming capture of electron 1, the possible final states are either $|\,\phi_1(2)\,\rangle$ or $|\,\phi_2(2)\,\rangle$. Using the product state, the probabilities for those two final states are $\psi_2(0)\,\langle\,\phi_1\,|\,\psi_1\,\rangle$ and $\psi_1(0)\,\langle\,\phi_2\,|\,\psi_2\,\rangle$, respectively. Insertion of the antisymmetrised state instead yields for the same two final states the amplitudes $2^{-1/2}\,(\psi_1(0)\,\langle\,\phi_1\,|\,\psi_2\,\rangle - \psi_2(0)\,\langle\,\phi_1\,|\,\psi_1\,\rangle$ and $2^{-1/2}\,(\psi_1(0)\,\langle\,\phi_2\,|\,\psi_2\,\rangle - \psi_2(0)\,\langle\,\phi_2\,|\,\psi_1\,\rangle)$ and thus additional exchange terms of the type $\langle\,\phi_i\,|\,\psi_j\,\rangle, i \neq j$. While the problem of matrix elements between Slater determinants with non-orthogonal orbitals has been considered already by Löwdin in [160], a more modern approach is based on second quantization and was used in the recent calculation of the overlap and exchange corrections in [41]. In that work, the general result for Z electrons including overlap and exchange corrections (adapted to

the present notation) is given by

$$B_j^{\text{ovl+ex}} \equiv P_j^{\text{SD}} = (-1)^{j+1} \prod_{i \in \text{occ} \backslash j} \langle\, \phi_i \,|\, \psi_i \,\rangle + (-1)^j \sum_{i' \in \text{occ} \backslash j} \langle\, \phi_j \,|\, \psi_{i'} \,\rangle \prod_{i \in \text{occ} \backslash j, i'} \langle\, \phi_i \,|\, \psi_i \,\rangle \tag{20}$$

which reduces to the two-electron result above, if it is reminded for this case that the probability is equal to the squared amplitude yielding a prefactor $1/2$ which cancels when considering that an identical probability as the one given for capture of one electron comes from considering capture of the other electron, as they are now (in the antisymmetrised case) indistinguishable. Finally, it may be noted, however, that even the *ansatz* of a properly antisymmetrised wave function like a Slater determinant for both $\tilde{\Psi}_0$ and $\tilde{\Phi}_f$ leads to $\mathcal{P}_f^{(0)}$ as defined in equation (16), if the approximation $\phi_i \approx \psi_i$ is adopted. Thus overlap and exchange corrections vanish ($B_j^{\text{ovl+ex}} = 1$), if identical orbitals are used for parent and daughter atoms. This is equivalent to saying that within this approximation there is always a one-to-one correspondence between the hole and the final state of Dy, i. e. Dy is left with unity probability in the configuration $\Phi_0^{(j)}$ (or $\tilde{\Phi}_0^{(j)}$).

On the other hand, this is not the case, if non-identical orbitals are used. The matrix elements describing the electron-capture process within the sudden approximation fulfill the sum rule

$$\sum_f \left| \langle \Upsilon_f | \hat{V}_W | \Upsilon_0 \rangle \right|^2 = \sum_j C_j \,|\, \psi_j(R) \,|^2 \sum_{f(j)} \left| \langle\, \tilde{\Phi}_f^{(j)} \,|\, \tilde{\Psi}_0^{(j)} \,\rangle \right|^2$$

$$= \sum_j C_j \,|\, \psi_j(R) \,|^2 \langle\, \tilde{\Psi}_0^{(j)} \,| \sum_{f(j)} |\, \tilde{\Phi}_f^{(j)} \,\rangle\langle\, \tilde{\Phi}_f^{(j)} \,|\, \tilde{\Psi}_0^{(j)} \,\rangle$$

$$= \sum_j C_j \,|\, \psi_j(R) \,|^2 \tag{21}$$

where the sums over $f(j)$ run over all final states accessible for capture of an electron from orbital j and it is used that the set of all final states $\{\, \tilde{\Phi}_f^{(j)} \,\}$ for a given hole (in j) spans the complete Hilbert space of $Z-1$ electrons. Furthermore, the minor $|\, \Psi_0^{(j)} \,\rangle$ of the Slater determinant $|\, \Psi_0 \,\rangle$ has been introduced in which the row and column in which orbital j occurs was removed. Since the overlap (overlap and exchange) correction factors B_j^{ovl} ($B_j^{\text{ovl+ex}}$) are smaller than unity, the sum-rule result directly shows that for a given hole (in orbital j) there is a non-vanishing probability for populating more than one final state. In fact, the probability that the final-state configuration differs from the initial state of the parent atom by more than the hole in the orbital $j \equiv \{n_j, \ell_j, J_j, m_{Jj}\}$ and thus the probability of forming configurations with additional excitations from configuration $|\, \tilde{\Phi}_0^{(j)} \,\rangle$ is (within the single-determinant approximation) given *exactly* by $P_{\text{exc}}^{(j)} = 1 - B_j^{\text{ovl+ex}}$. This equation highlights again that the possibility of exciting different final state after capture from a specific orbital is within the here considered level of approximation solely due to the non-orthogonality of the orbitals in the parent and daughter atoms. The occurrence of these excitations and its possible importance for holmium neutrino-mass experiments was first pointed out by Robertson [37]. In fact, he concentrated on a sub-class of the excited states that he coined two-hole states. The idea behind this name is that almost all states of the daughter atom that differ from the configuration $\tilde{\Phi}_0^{(j)}$ by the transfer

of one electron from an orbital occupied in $\tilde{\Phi}_0^{(j)}$ to one that in $\tilde{\Phi}_0^{(j)}$ was unoccupied correspond to two-hole configurations. However, as the capture of the outermost valence electron does not lead to a hole, but is nevertheless commonly subsumed under one-hole states, all configurations that are (formally) created by the excitation of a single electron from $\tilde{\Phi}_0^{(j)}$ are usually called two-hole states. This includes those states in which there is only a single hole in orbital j, but excitation of one of the outermost electrons. It may also be noted that in general there is a non-zero transition matrix element (overlap) also for those configurations in which, e.g., an electron from an orbital occupied in $\tilde{\Phi}_0^{(j)}$ is transferred to the hole. Also these configurations belong to the singly-excited configurations relative to the reference configuration $\tilde{\Phi}_0^{(j)}$, but possess only a single hole (or no hole in the case that the hole is filled by an outermost electron which corresponds to the Dy ground state) and in fact no hole in orbital j. From this discussion it should be clear that the sometimes also adopted notion of first-order and higher-order transitions is formally more adequate (less misleading). In this case, the number of formal electron transfers out of the reference configuration $\tilde{\Phi}_0^{(j)}$ is specified. The first-order transition means no further excitation and the final state is equal to $\tilde{\Phi}_0^{(j)}$. A second-order transition involves one excitation and thus one electron occupies a different orbital compared to $\tilde{\Phi}_0^{(j)}$, i.e. $\tilde{\Phi}_{p \to q}^{(j)}$ describes the configuration with the hole in orbital j and an additional electron being transferred from orbital p to q which in most cases represents a two-hole state with holes in the orbitals j and p. Nevertheless it should be reminded that even this notion is strictly applicable only within the single-determinant approximation in which a state is uniquely represented by a single configuration.

While in [37] the relevance of the two-hole states was estimated on the basis of matrix elements calculated earlier for Xe atoms, a more thorough calculation was presented in [38]. The relevance of double excitations with respect to $\tilde{\Phi}_0^{(j)}$ (usually called three-hole states) were then considered in [24]. In analogy to inner-shell photoionization of atoms in which the fast removal of an electron close to the nucleus leads to a sudden change of the screening experienced by the other electrons and thus a non-orthogonality of the orbitals of the parent atom and the daughter ion, the population of the final states different from $\tilde{\Phi}_0^{(j)}$ has also been named shake up, if the excited electron occupies a bound orbital below the ionization threshold, or shake off, if it is transferred into the ionization continuum. It should be reminded, however, that (as in photoionization) shake up and shake off are no physical processes on their own that occur with a time-delay to the electron capture, but are an intrinsic part of the capture process itself. As a consequence, the energy that is, e.g., formally required for exciting a second electron (by forming a second hole) has to be accounted for in the energy balance as being part of the final-state energy E_f that describes the energy of the final state of the daughter atom (relative to the one of the parent atom). This energy is not available to the neutrino and thus directly enters the phase-space factor g defined in equation (13). Every such final state contributes an own Lorentzian peak to the capture spectrum. This is different for real physical processes describing the decay of the final states after they were formed in the capture process, like photon emission (with decreasing probability, if the hole is formed in an outer shell), Auger decay (increasing probability for outer shells), or Coster-Kronig transitions. The energies released in these relaxation processes are, in contrast to the shake up or off "processes", absorbed in the micro calorimeters and thus only their consequences for the widths of the final states due to their finite life times have to be accounted for in theory, but not the energy portions taken away by photons or electrons.

The probability for populating the second-order (two-hole) state $\tilde{\Phi}_{p \to q}^{(j)}$ is evidently (within the single-determinant approximation and ignoring the finite size of the

nucleus) proportional to

$$P_{j,p \to q}^{\mathrm{SD}} \;=\; \left| \langle\, \tilde{\Phi}_{p \to q}^{(j)} \,|\, \sum_{j=1}^{Z} \delta(r_j - R) \,|\, \tilde{\Psi}_0 \,\rangle \right|^2 . \tag{22}$$

If the indistinguishability of the electrons is ignored and the wavefunctions are expressed by simple products of the orbitals, this expression reduces to

$$
\begin{aligned}
P_{j,p \to q}^{\mathrm{prod}} &= \left| \langle\, \Phi_{p \to q}^{(j)} \,|\, \delta(r_j - R) \,|\, \Psi_0 \,\rangle \right|^2 \\
&= \big| \psi_j(R) \, \langle\, \phi_1 \, \phi_2 \, \cdots \, \phi_{j-1} \, \phi_{j+1} \, \cdots \, \phi_{p-1} \, \phi_q \, \phi_{p+1} \, \cdots \, \phi_Z \,| \\
&\qquad\qquad |\, \psi_1 \, \psi_2 \, \cdots \, \psi_{j-1} \, \psi_{j+1} \, \cdots \, \psi_{p-1} \, \psi_p \, \psi_{p+1} \, \cdots \, \psi_Z \,\rangle \big|^2 \\
&= \left| \psi_j(R) \, \langle\, \phi_q \,|\, \psi_p \,\rangle \prod_{i \in \mathrm{occ} \setminus j,p} \langle\, \phi_i \,|\, \psi_i \,\rangle \right|^2
\end{aligned}
\tag{23}
$$

where, as before, "occ" refers to the orbitals occupied in the initial state $|\,\Psi_0\,\rangle$. In practice, the index i should start for electron capture in Ho at the main quantum number $n_i = 3$, since otherwise the energy release in the capture process cannot fulfill the energy-conservation law. The Pauli principle evidently requires also that the spin orbital q that should be populated has to have been unoccupied in $|\,\Psi_0\,\rangle$. Note that within this simplified description double counting has to be avoided. Since the electrons are treated as being distinguishable, the state in which the electron in orbital p is captured and this capture process is accompanied by an excitation from orbital j into q occurs as a different process than a capture from j accompanied by an excitation from p to q. This is, of course, a non-physical short-coming of the model that is easily cured by a corresponding proper selection of the possible final states ($p > j$, for the orbital energies ϵ this corresponds to $\epsilon_p \geq \epsilon_j$) or using the properly antisymmetrised Slater determinants as in equation (22). Finally, it may be used that all initially occupied orbitals (and thus all but orbital q) are definitely bound and may thus the chosen to be purely real (or imaginary). Considering also the definition of B_j^{ovl} in equation (20) this yields

$$P_{j,p \to q}^{\mathrm{prod}} \;=\; |\,\psi_j(R)\,|^2 \, |\langle\, \phi_q \,|\, \psi_p \,\rangle|^2 \prod_{i \in \mathrm{occ} \setminus j,p} |\langle\, \phi_i \,|\, \psi_i \,\rangle|^2 = |\,\psi_j(R)\,|^2 \, \frac{|\langle\, \phi_q \,|\, \psi_p \,\rangle|^2}{|\langle\, \phi_p \,|\, \psi_p \,\rangle|^2} \, B_j^{\mathrm{ovl}} . \tag{24}$$

As a consequence of the non-orthogonality of the orbitals of Dy and Ho the electron-capture spectrum contains thus satellite peaks (each of Lorentzian shape) centred at the various energies $E_{p \to q}^{(j)}$ that are the energy differences between the states $|\,\tilde{\Phi}_{p \to q}^{(j)}\,\rangle$ of Dy and $|\,\tilde{\Psi}_0\,\rangle$ of Ho, respectively. These lines occur in addition to the main peaks at E_j that is the energy difference between $|\,\tilde{\Phi}_0^{(j)}\,\rangle$ and $|\,\tilde{\Psi}_0\,\rangle$. Clearly, every final state possesses also its own life time and thus contributes a Lorentzian with a different width. However, the by far fastest relaxation processes involve the deepest hole. Therefore, as a first approximation the same width Γ may be used for all final states $|\,\tilde{\Phi}_{p \to q}^{(j)}\,\rangle$ with the same j. Clearly, this may not be a very good approximation, if p belongs to the same shell as j, but for reasons of energy conservation these double-hole states can in Ho only occur in the capture of an electron from an outer shell ($n \geq 4$) and thus further away from the neutrino-mass-sensitive

end point. An extension to higher-order terms (three-hole states etc.) is evident. For third-order terms one has to use $|\tilde{\Phi}^{(j)}_{p,p'\rightarrow q,q'}\rangle$ instead of $|\tilde{\Phi}^{(j)}_{p\rightarrow q}\rangle$ in equation (22) where $|\tilde{\Phi}^{(j)}_{p,p'\rightarrow q,q'}\rangle$ differs from $|\tilde{\Phi}^{(j)}_{0}\rangle$ by promoting two electrons from the orbitals p and p' into q and q'. As was pointed out in [24, 38], in a more accurate treatment, the orbitals should be optimized differently for different final states. If only the leading effect of the different screening due to the holes is incorporated in the calculation, there is one set of orbitals $\{|\phi^{(j)}_i\rangle\}$ for all states with a single hole in j, another set $\{|\phi^{(j,p)}_i\rangle\}$ for all states with two holes in j and p, etc. In fact, so far the calculations considered a single hole in the orbital calculation, i. e. $\{|\phi^{(j)}_i\rangle\}$ for all states obtained after capture from orbital j.

Within the spirit of the single-determinant approximation every final state (including all single-hole states, two-holes states, etc.) is independent of all others, since there is no interference between different transition amplitudes as every transition leads to a distinct final state. More accurately, this independence formally requires orthogonality between all final states $|\tilde{\Phi}_f\rangle$ which is not strictly fulfilled, if not identical orbitals $\{\phi_i\}$ are used for all final states, but the orbitals are optimized for different final states and, e. g., $\{\phi^{(j)}_i\}$ are adopted. However, even in this case it is nevertheless expected to be a reasonable approximation, especially when comparing states with a different number of excitations from $|\Phi^{(j)}_0\rangle$, i. e., a different number of holes. (Note that this independence of the transition amplitudes is not necessarily a good approximation for the widths, since in this case different relaxation processes can in principle connect the same initial and final states even in the single-determinant approximation with an identical set of orthogonal orbitals.) With the assumption of independent amplitudes the total probability for populating a final state with two holes in the orbitals j and p is obtained from an incoherent sum over the individual transition probabilities in equations (22) or (24),

$$P^{\text{SD}}_{j,p} = \sum_{q\in\text{unocc}} P^{\text{SD}}_{j,p\rightarrow q} \approx \sum_{q\in\text{occ}\backslash j,p} P^{\text{prod}}_{j,p\rightarrow q}$$

$$= |\psi_j(R)|^2 \frac{B^{\text{ovl}}_j}{|\langle\phi_p|\psi_p\rangle|^2} \sum_{q\in\text{unocc}} \langle\psi_p|\phi_q\rangle\langle\phi_q|\psi_p\rangle . \qquad (25)$$

Since the sum over q runs over all initially unoccupied orbitals and thus includes, in fact, an integral over all continuum orbitals, it is convenient to use the completeness relation

$$\mathbf{1} = \sum_{q=1}^{\infty} |\phi_q\rangle\langle\phi_q| = \sum_{q\in\text{occ}\backslash p} |\phi_q\rangle\langle\phi_q| + |\phi_p\rangle\langle\phi_p| + \sum_{q\in\text{unocc}} |\phi_q\rangle\langle\phi_q| \qquad (26)$$

to rewrite equation (25) as

$$P^{\text{SD}}_{j,p} \approx P^{\text{prod}}_{j,p} = |\psi_j(R)|^2 \frac{B^{\text{ovl}}_j}{|\langle\phi_p|\psi_p\rangle|^2} \left(1 - |\langle\phi_p|\psi_p\rangle|^2 - \sum_{q\in\text{occ}\backslash p} |\langle\phi_q|\psi_p\rangle|^2\right) . \qquad (27)$$

In the so-called Vatai approximation [161, 162] the overlaps between Ho and Dy wavefunctions with the same indices and thus identical quantum numbers are approximated by unity. In equation (27) such overlaps occur three times, namely as the second term within the parentheses and twice in the fraction (both in the nominator

implicitly in B_j^{ovl} and in the denominator). Since the term within the parentheses is subtracted from unity, it is evidently not a good idea to use the Vatai approximation for it. (In fact, the probability becomes negative in this case.) This is different for the term outside the parentheses which may thus be approximated by unity to give

$$P_{j,p}^{\text{Vatai}} \;=\; |\,\psi_j(R)\,|^2 \left(1 \;-\; |\,\langle\,\phi_p\,|\,\psi_p\,\rangle\,|^2 \;-\; \sum_{q\in\,\text{occ}\,\backslash p} |\,\langle\,\phi_q\,|\,\psi_p\,\rangle\,|^2 \right). \tag{28}$$

In the evaluation of $P_{j,p}^{\text{prod}}$ or $P_{j,p}^{\text{Vatai}}$ it may be used that many matrix elements are identical, i.e. the value of $\langle\,\phi_p\,|\,\psi_p\,\rangle$ ($p \equiv \{n_p, \ell_p, J_p, m_{Jp}\}$) is independent of the quantum number m_{Jp} yielding $\langle\,\phi_p\,|\,\psi_p\,\rangle = \langle\,\phi_{p'}\,|\,\psi_{p'}\,\rangle$ for $n_p = n_{p'}, \ell_p = \ell_{p'}, J_p = J_{p'}, m_{Jp} \neq m_{Jp'}$. Similarly, the off-diagonal overlaps $\langle\,\phi_q\,|\,\psi_p\,\rangle$ with $p \neq q$ vanish for symmetry reasons, if the two orbitals $|\,\phi_q\,\rangle$ and $|\,\psi_p\,\rangle$ do not agree in all but the main quantum numbers n_p and n_q and one has $\langle\,\phi_q\,|\,\psi_p\,\rangle = \langle\,\phi_{q'}\,|\,\psi_{p'}\,\rangle$ for $n_q = n_{q'}, \; n_p = n_{p'}, \; \ell_q = \ell_{q'} = \ell_p = \ell_{p'} = \ell, \; J_q = J_{q'} = J_p = J_{p'} = J, \; m_{Jq} = m_{Jp} \neq m_{Jq'} = m_{Jp'}$. Thus it is convenient to introduce reduced sets of quantum numbers $\tilde{p} \equiv \{n_p, \ell_p, J_p\}$ and the corresponding m_{Jp} independent overlaps $\langle\,\phi_{\tilde{q}}\,|\,\psi_{\tilde{p}}\,\rangle$. According to [38] one finds then in agreement with the result given in [156] within this approximation

$$\tilde{P}_{j,p}^{\text{Vatai}} \;=\; \frac{P_{j,p}^{\text{Vatai}}}{|\,\psi_j(R)\,|^2} \;=\; 1 \;-\; |\,\langle\,\phi_{\tilde{p}}\,|\,\psi_{\tilde{p}}\,\rangle\,|^{2\,N_{\tilde{p}}} \;-\; \sum_{\tilde{q}\in\,\text{occ}\,\backslash\tilde{p}} \frac{N_{\tilde{q}}\,N_{\tilde{p}}}{2J+1} |\,\langle\,\phi_{\tilde{q}}\,|\,\psi_{\tilde{p}}\,\rangle\,|^2 \tag{29}$$

where $N_{\tilde{i}}$ is the number of occupied magnetic substates with the same reduced quantum numbers $\tilde{i}$. For all closed shells one evidently finds $N_{\tilde{i}} = 2J_{\tilde{i}} + 1$. For not fully closed shells one has to use a correspondingly modified value.

The calorimetrically measured electron capture spectrum has been calculated within the sudden and the single-determinant approximations, but considering all effects discussed above for the first-order (single-hole) states on the level of equations (18) and (20) (including the effects of the finite size of the nucleus). Furthermore, the second-order (two-hole) states were included using equation (29), but including overlap and exchange corrections. The resulting spectrum

$$\frac{\mathrm{d}N}{\mathrm{d}E_C} \propto g(m_\nu^2, Q_{\text{EC}} - E_C) \sum_{j\in\text{occ}} C_j\,|\,\psi_j(R)\,|^2\,B_j^{\text{ovl+ex}} \left(\frac{(2\pi)^{-1}\,\Gamma_j}{(E_C - E_j)^2 \,+\, (\Gamma_j^2/4)} \right.$$

$$\left. + \sum_{p\in\text{occ},\,p\geq j} \frac{\tilde{P}_{j,p}^{\text{Vatai}}}{|\,\langle\,\phi_p\,|\,\psi_p\,\rangle\,|^2} \frac{(2\pi)^{-1}\,\Gamma_j}{(E_C - E_{j,p})^2 \,+\, (\Gamma_j^2/4)} \right) \tag{30}$$

with the excitation energy $E_{j,p}$ of the two-hole state $\tilde{P}_{p\to q}^{(j)}$ for $q = \{n_q = 4, \ell_q = 3, J_q = 7/2\} \equiv 4f_{7/2}$ is shown in Figure 35. This spectrum is compared to the one that is obtained when using the parameters in [37]. Note that in equation (30) the sums over j and p run over all possible orbitals from which capture is possible (including $j = 4f_{7/2}$ which is not leading to a hole), including their magnetic substates. In practice, it is more convenient to perform the sum over inequivalent hole states and to multiply the expression with the multiplicities of the states. Furthermore, it has to be emphasized that equation (30) implies the additional approximation that the whole transition probability of a given second-order transition (two-hole state) is put into one Lorentzian peak centered at the energy of the lowest lying state $|\,\Phi_{j,p\to q}\,\rangle$ within the q manifold. De Rujula and Lusignoli [40] on the other hand advocate to explicitly take into account especially the shape of the shake-off spectrum, i.e. to consider
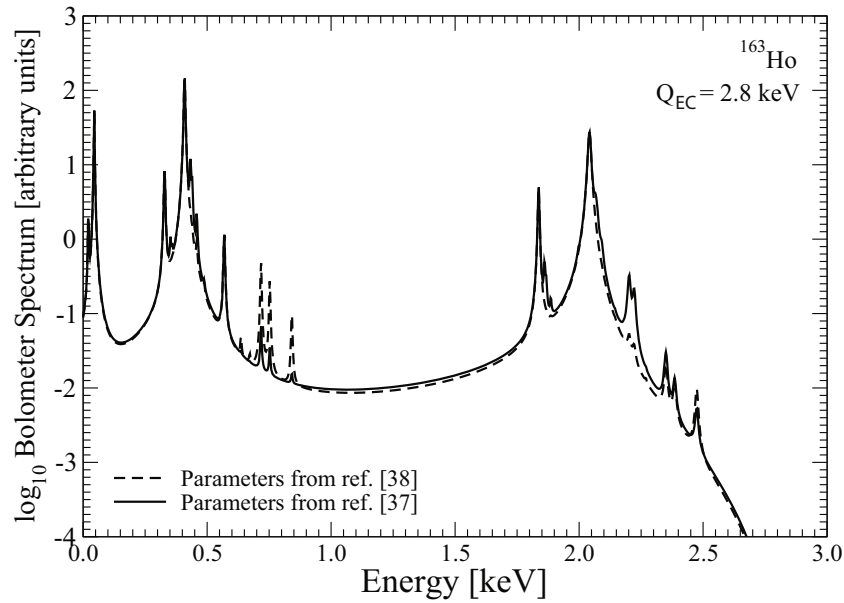
Fig. 35. Calorimetrically measured spectrum plotted with Logarithmic (basis 10) y-scale (30) including the one- and two-hole probabilities calculated with the parameters given in [38] (dashed line) and with the ones from [37] (solid line), assuming $Q = 2.8\,\mathrm{keV}$. Figure reproduced from [24]. (This figure is subject to copyright protection and is not covered by a Creative Commons license.)

the energy distribution due to the various shake-up and shake-off states represented by q which in the latter case are even continuous. However, they use less advanced wavefunctions for both first and second order transitions in comparison to the ones used in this work. An intermediate approximation in between those two would be to still put the whole transition strength at one energy, but to use a mean two-hole excitation energy $\bar{E}_{j,p}$.

10.2 Sensitivity to the neutrino mass

As is evident from equation (30), every final state f contributes (within this approximation) a Lorentzian peak to the calorimetrically measured spectrum. Thus, *per se*, it is irrelevant which character the final state has, i.e. whether it is a single-hole, a two-hole, or a multi-hole state or whether it is of any other nature. The importance of a specific state for the determination of the neutrino mass depends on its contribution to the bolometer spectrum close to the neutrino-mass sensitive end point. This in turn depends on the relative strength of the transition $S_{f=\{j(p)\}} = |\psi_j(R)|^2 \, B_j^{\mathrm{ovl+ex}} \, T_{j(p)}$ with $T_{j(p)} = 1$ for a one-hole state with capture from orbital j and $T_{j(p)} = \tilde{P}_{j,p}^{\mathrm{Vatai}} \, |/\langle \phi_p | \psi_p \rangle|^2$ for a two-hole state, the energy distance $\Delta E_f = Q_{\mathrm{EC}} - E_f$ (with $E_f = E_j$ or $E_f = E_{j,p}$) of the state from the end point, and the width Γ_f of the state. In equation (30), it is also assumed that the nuclear matrix element is independent of the final state of the Dy atom, and thus $C_j = C$ has been omitted from the relative transition strength $S_{j(p)}$.

The relative weight of a final state f to the bolometer spectrum at the end point $(E_\mathrm{C} \approx Q_\mathrm{EC})$, i.e. its contribution relative to other final states, is

$$W_f^\mathrm{rel} \approx \frac{S_{f=\{j(p)\}}}{\Delta E_f^2}, \tag{31}$$

if the state is sufficiently far from the endpoint $(\Delta E_f \gg \Gamma_f)$. Assuming that the value $Q_\mathrm{EC} \approx 2.8\,\mathrm{keV}$ determined most recently by the ECHo collaboration [23] is correct, and that the widths of the final hole states are of the order of 10 eV, the approximation in equation (31) is well satisfied for all first- and second-order transitions used in the calculation of the spectrum according to equation (30) and listed explicitly in Tables 1 and 2 of [38]. Based on these data, out of the one-hole states (first-order transitions) the evidently clearly dominant contribution close to the endpoint stems from the $j = 3s_{1/2}$ single-hole state, since it is closest to the endpoint and has an about four times larger strength (S_j) compared to the more than 1.5 keV further away $4s_{1/2}$ hole state. If the relative strength of the $3s_{1/2}$ state is (arbitrarily) set equal to $S_{j=3s_{1/2}} = 100\,\%$, one finds $W_{j=3s_{1/2}} = 100\,\%/(2.8 - 2.04)^2 = 174\,\%\,\mathrm{keV}^{-2}$. Analogously, the relative weight of the $4\mathrm{s}_{1/2}$ is $W_{j=4s_{1/2}} = 24.4\,\%/(2.8 - 0.41)^2 = 4.3\,\%\,\mathrm{keV}^{-2}$. While the $3p_{1/2}$ hole state is about 1 keV further away from the endpoint, its strength is a factor 20 smaller compared to $S_{j=3s_{1/2}}$, $W_{j=3p_{1/2}} = 5.1\,\%/(2.8 - 1.84)^2 = 5.5\,\%\,\mathrm{keV}^{-2}$. The two-hole states $f = \{j = 3s_{1/2}, p\}$ are closer to the endpoint than the $3s_{1/2}$ single-hole state, but possess much smaller transition strengths. The $f = \{j = 3s_{1/2}, p = 4s_{1/2}\}$ two-hole state (being closest to the end point) has a relative weight $W_{j=3s_{1/2},p=4s_{1/2}} = 0.17\,\%/(2.8 - 2.47)^2 = 1.6\,\%\,\mathrm{keV}^{-2}$ and the $f = \{j = 3s_{1/2}, p = 4d_{3/2}\}$ two-hole state (having the largest transition strength) has $W_{j=3s_{1/2},p=4d_{3/2}} = 0.93\,\%/(2.8 - 2.2)^2 = 2.6\,\%\,\mathrm{keV}^{-2}$. Based on these numbers the bolometer spectrum close to the end point is clearly dominated by a single resonance, the $j = 3s_{1/2}$ single-hole state. This is important for the extraction of the neutrino mass from bolometer experiments, since this reduces the number of parameters that have to be fitted dramatically. Under this assumption and assuming a Lorentzian shape, one has four parameters to fit simultaneously: the neutrino mass m_ν, the distance $\Delta E_{j=3s_{1/2}}$ of the resonance (with respect to Q_EC), its strength $S_{j=3s_{1/2}}$ and the width $\Gamma_{j=3s_{1/2}}$. To include the experimental resolution in the fit, one must first fold the theoretical upper end of the spectrum with the experimentally determined profile of the detector.

11 ECHo schedule

11.1 Medium scale experiment – ECHo-1k

In 2015, the ECHo collaboration has started the first phase of the project leading to a medium size experiment capable of reaching a sensitivity of less than 10 eV/c^2 on the electron neutrino mass. A ^{163}Ho activity of about 1 kBq is employed, correspondingly, this project phase is referred to as ECHo-1k. This first phase is structured to be completed within a three-year period, 2015–2018. According to Figure 5, to reach the intended sensitivity, a total statistics of about 10^{10} events in the full ^{163}Ho spectrum needs to be acquired. With 1 kBq ^{163}Ho activity, such a spectrum is obtained within about one year.

A variety of novel experimental techniques and methods are being developed and brought together in order to achieve this result. These include: the preparation of large-scale radiochemically ultra-pure ^{163}Ho sources, the development of fast high-energy resolution MMC arrays readout using a frequency domain multiplexing scheme

and characterized by having ^{163}Ho enclosed in the absorbers, and, in order to operate the detectors, the design and construction of a well-shielded cryogenic platform with unprecedented short and long term temperature stability. At the same time investigations of all possible background contributions and the development of methods to reduce them are needed as well as a more precise understanding of the expected spectral shape. In this respect, a very important result was already obtained within ECHo-1k: a more precise Q_{EC}-value for the EC in ^{163}Ho with an uncertainty of about 30 eV has been measured using the Penning trap mass spectrometer SHIPTRAP at GSI, Darmstadt, removing one of the largest uncertainties in the description of the end point region of the ^{163}Ho spectrum. The next aspect we aim to clarify is the contribution of higher order processes, involved in the electron capture decay of ^{163}Ho and understand which signatures those excited states produce in the shape of the spectrum, in particular in the last few hundreds eV.

In this first phase of the experiment, two MMC arrays (with about 50 pixels each) with a foreseen energy resolution $\Delta E_{FWHM} \leq 5$ eV will be designed and fabricated. Each pixel will contain about 10 Bq of ^{163}Ho. This will be ion-implanted in the absorber of each detector of the arrays at ISOLDE-CERN and/or at the RISIKO facility at Mainz University. The design of the MMC arrays has been developed on the basis of the results obtained with the first two detector designs that have been used for ^{163}Ho ion-implantation [32,64]. In particular the ^{163}Ho activity in the pixels will be chosen as the minimum between the value ensuring the unresolved pile-up fraction to be smaller than 10^{-5} and the value for which the contribution to the total detector heat capacity of the corresponding implanted ^{163}Ho ions is not the dominant one.

As the main route, thermal neutron activation of enriched ^{162}Er targets will be adopted to produce the ^{163}Ho sources. A careful separation of ^{163}Ho will be performed by a combination of chemical separations before as well as chemical and mass separation after the irradiation of the sample to reach the required purity of the sources to be used in calorimetric measurements. A minimization of background sources inside the detector itself can be achieved based on detailed characterization of the source material, including measurements in a low-level underground laboratory.

In order to read out the two MMC arrays of ECHo-1k, a frequency domain multiplexing scheme based on unshunted rf-SQUIDs has been developed which is capable to meet the required properties in terms of speed and energy resolution. The complete experiment will be mounted in a dedicated cryogenic platform which has been designed and built. This cryostat allows for performing measurements at a base temperature below 30 mK with ultrahigh temperature stability in a shielded environment.

For a successful analysis of the endpoint region of the spectrum to extract information on the electron neutrino mass, a precise study of the background sources, which lead to energy depositions in MMCs with energies below 10 keV, is presently carried out. Effects of radioactive contamination in the materials, which is used for detectors and detector set-up fabrication, and effects of cosmic radiation are investigated through Monte Carlo simulation using GEANT4 and with dedicated experiments to validate the results of the simulations. Measures to reduce the background in the calorimetric measurement are presently under development, including material screening and the installation of an optimized muon veto.

During ECHo-1k, R&D will be done towards the second phase of the ECHo project, called ECHo-1M.

11.2 ECHo-1M and the investigation of the sub-eV range

The second stage of the ECHo experiment, ECHo-1M, takes its name from the fact that the total ^{163}Ho activity which will be enclosed in the detectors will be of the

order of one MBq. This ^{163}Ho activity is necessary to reach a neutrino mass sensitivity below 1 eV within a few years of measuring time.

ECHo-1M is not simply a scaling up of ECHo-1k, but more stringent requirements have to be fulfilled. During ECHo-1k an intense R&D is performed for the optimization of the single pixel properties and the multiplexed readout. The optimization of the activity per pixel and a study of several absorber materials will be performed. Assuming that the activity per pixel will still be a few tens of Bq, as in ECHo-1k, the number of single detectors which are needed to host the required activity will be of the order of 10^4–10^5. This large number of detectors can only be read out by using a sophisticated multiplexing scheme able to keep the single pixel performance almost unchanged. The time resolution of the signal in ECHo-1M will be about the same as in ECHo-1k, $\tau_\mathrm{r} < 0.5\,\mu$s. Therefore the bandwidth per detector in the multiplexed array of MMCs will not be strongly modified. On the other hand the larger number of pixels, which are required to host order of MBq of ^{163}Ho, still leads to a number of technological challenges, even if the microwave SQUID multiplexing is an intrinsically scalable multiplexing approach, i.e., the total number of channels can be easily increased without affecting the SQUID or detector performance. First, about 10^4 virtually identical detectors, each with two pixels, are envisaged to be produced. This is feasible by using standard microfabrication techniques. Currently, we are aiming at using 3 inch Si substrates, each hosting about 1000 detectors that are read out by an integrated μMUX. Thus, about 50 wafers need to be processed. Second, the development of a specifically optimized SDR platform as well as the implementation of an efficient algorithm for channelization and signal processing running on that platforms is an on-going research field. In parallel we are investigating the possibility to overcome the limits due to Nb CPW microwave resonators. For this reason, we are looking for alternative approaches, for example materials with very high kinetic inductance ratio that allow for shrinking the geometrical size of the resonators and therefore to increase the total number of detectors on a wafer by more than one order of magnitude. This will be of utmost importance for potential future experiments beyond ECHo-1M where the number of detectors could be larger than 10^6.

A similar scaling approach is required also for the production of a large amount of ^{163}Ho samples characterized by extremely high purity. For ECHo-1M a total activity inventory that is about 1000 times higher compared to ECHo-1k will be required, translating to the need of ^{163}Ho samples with a volume significantly larger than 10^{18} atoms. As first steps in this direction, chemical separation techniques will be tailored towards the processing of larger Er samples, and, ideally, material of higher enrichment in ^{162}Er than was used to date will be irradiated. To evaluate the optimum irradiation cycle, the cross-section of the ^{163}Ho(n,γ) reaction needs to be known and is currently under determination within ECHo-1k [114].

The requirements on the background level for ECHo-1M will be defined by the more precise understanding of the sources and a more precise modeling of the background spectrum worked out during ECHo-1k.

The sensitivity to the sub-eV electron neutrino mass is deeply related to the precise determination of the Q_EC-value. The aim is to have available for the analysis of the spectrum in the ECHo-1M experiment, a Q_EC-value measured with a precision of 1 eV. This goal is planned to be reached by the use of the newly developed Penning traps system PENTATRAP [121,154]. The PENTATRAP project aims at mass-ratio measurements of long-lived and stable nuclides in a wide mass range with a so far unreached uncertainty well below 10^{-11}. This makes the project unique among the existing and planned Penning-trap mass spectrometers. Physics programs which demand such extremely low uncertainties in mass-ratio measurements embrace, e.g., the determination of the neutrino mass, both in tritium-based experiments as well as in ^{163}Ho-based experiments, the search for sterile neutrinos or tests of Einstein's

energy-mass relation and of quantum electrodynamics in strong electromagnetic fields [163]. A successful measurement of the Q_{EC}-value of the EC in ^{163}Ho rests on several pillars. First of all, extremely stable magnetic field and trap voltages of the mass spectrometer will be provided. Several measures are called to ensure this: screening the magnet from stray electrical and magnetic fields, a temperature stabilized experimental room with a vibration-free concrete cushion for the magnet, a sophisticated system for the stabilization of the magnetic field of the mass spectrometer and a dedicated trap-voltages power supply developed at the MPIK. Second, the measurement will be performed on highly-charged ions of ^{163}Ho and ^{163}Dy, which will be produced either with the Dresden-EBIT [164] or Heidelberg-EBIT [165] ion source. Third, the cyclotron frequencies of the two nuclides will be measured simultaneously. For this, five cylindrical Penning traps will be employed [154] and the novel cyclotron-frequency measurement technique described in [166] will be applied.

As mentioned in Section 10, the availability of high statistics spectra, acquired within ECHo-1k and while ECHo-1M is running, will allow us to determine the empirical ^{163}Ho spectral shape at a very high level of accuracy. At the same time, these high statistics spectra will be the basis for theorists to test their models. In parallel we plan to perform calorimetric measurements on other nuclides decaying through electron capture in order to test the model developed to describe the ^{163}Ho spectrum on other systems.

12 Search of sterile neutrino signatures with the analysis of the ^{163}Ho spectrum

The aim of the ECHo collaboration is to reach sub-eV sensitivity on the electron neutrino mass by means of the analysis of calorimetrically measured ^{163}Ho spectra. Therefore high statistics ^{163}Ho spectra will be measured with high energy resolution over the full energy range, from a threshold energy of a few tens of eV to the endpoint of the spectrum. The availability of these high precision spectra opens the possibility to perform additional investigation in respect to the main goal to determine the electron neutrino mass. The quite pressing question on the existence of sterile neutrinos, both in the eV (see the reviews in [167,168]) and in the keV ranges (see the recent review [169]), could be addressed by the analysis of the high statistics ^{163}Ho spectra acquired within the several phases of ECHo.

In the model where only three active neutrinos exist, the electron neutrino state can be written in terms of the single mass eigenstates as:

$$m(\nu_e)^2 = \sum_{i=1}^{3} |U_{ei}^2| m(\nu_i)^2. \tag{32}$$

In case sterile neutrinos would exist, at least a fourth neutrino mass eigenstate, m_4, would mix with the three "active" mass eigenstates to give the electron neutrino emitted in EC processes. In such a case, and considering the approximation that the three light neutrino mass eigenstates are much lighter than m_4, the electron neutrino state can be written as:

$$m(\nu_e)^2 = \sum_{i=1}^{3} |U_{ei}^2| m(\nu_i)^2 + |U_{e4}^2| m(\nu_4)^2 = |U_{ea}^2| m_a^2 + |U_{e4}^2| m_4^2. \tag{33}$$

By including this expression for the electron neutrino mass in the equation describing the ^{163}Ho spectrum and by using the approximation that $m_a = 0$ eV, the

spectrum assume the following form:

$$\frac{\mathrm{d}N}{\mathrm{d}E_{\mathrm{C}}} = A\left((Q_{\mathrm{EC}} - E_{\mathrm{H}})^2(1 - U_{\mathrm{e}4}^2) + (Q_{\mathrm{EC}} - E_{\mathrm{H}})^2 U_{\mathrm{e}4}^2 \sqrt{1 - \frac{m_4^2}{(Q_{\mathrm{EC}} - E_{\mathrm{H}})^2}}\right)$$
$$\times \sum_H C_H n_H B_H \, \phi_H^2(0) \frac{\Gamma_H/2\pi}{(E_{\mathrm{C}} - E_H)^2 + \Gamma_H^2/4}. \tag{34}$$

The existence of a fourth neutrino mass eigenstate reduces the phase space for energy between $Q_{\mathrm{EC}} - m_4$ and Q_{EC}. With the analysis of the electron capture spectrum of ^{163}Ho it is possible to investigate the existence of eV scale sterile neutrinos as well as keV sterile neutrinos up to masses m_4 smaller than the Q_{EC}-value of the decay of about 2.8 keV.

The requirements for scrutinizing the parameter space allowed for eV-scale sterile neutrinos within the ECHo experiment have been studied in [170]. Figure 36 shows, indicated by the black curve, the region in the plane $sin^2(\theta_{ee}) - \Delta m_{41}^2$ allowed at 95.45% C.L. as derived by a global fit of short-baseline neutrino oscillation data [168]. By restricting the analysis to the data of ν_e and $\bar{\nu}_e$ disappearance experiments [171,172] and taking into account the Mainz [173] and Troitsk [174,175] bounds, the constrains on the sterile neutrino parameters are less stringent and are indicated by the region within the gray curves which enclose the 95.45% C.L. allowed regions. The parameter space that can be investigated with the ECHo experiment is indicated at 90% C.L., 95.45% C.L. and 99.73% C.L. for three different statistics in the full spectrum. For these calculations, the best value for the endpoint energy $Q_{\mathrm{EC}} = 2.833$ keV obtained in [23] was used. The detector response was assumed to be Gaussian with $\Delta E_{\mathrm{FWHM}} = 2$ eV. The only background considered was the unresolved pile-up characterized by an unresolved pile-up fraction $f_{\mathrm{pp}} = 10^{-6}$. In this analysis only first order excited states have been considered for generating the ^{163}Ho EC spectrum. As we discussed in Section 10, the presence in the spectrum of structures related to higher order excited states in ^{163}Dy has the effect of increasing the fraction of counts at the end point region of the spectrum. This increased statistics has, in turn, the effect to increase the sensitivity to finite neutrino masses and, in particular, to eV scale neutrinos. Therefore the limits presented in Figure 36 should be seen as the more conservative limits or the limits achievable in a worst case scenario. In this case, to completely cover the parameter space allowed for the eV sterile neutrinos, a total number of counts in the complete ^{163}Ho spectrum of 10^{18} would be required. Nevertheless already with 10^{16} counts it would be possible to search for the existence of eV-scale sterile neutrinos in the more restricted area enclosed by the black curve. With this statistics it will be possible to reach comparable results as it could be achieved by the KATRIN experiment [173,176]. For the investigation of eV sterile neutrinos, no additional modifications to the design of the ECHo experiment are required since the fraction of the spectrum affected by eV scale sterile neutrinos is not much larger than the region that will be analyzed to identify effects due to the "active" component of electron neutrinos, only the analysis tools will be modified to include the parameters describing the mixing of m_4 with the three light mass eigenstates.

The investigation of keV sterile neutrinos using ^{163}Ho has been discussed already in [169] and in [177]. In [177–179] the fact that the ratio between the amplitude of the NI-line and the MI-line is affected by the reduced phase space for the capture of 3s electrons due to the existence of a keV scale mass m_4 between $Q_{\mathrm{EC}} - E_{3s}$ and $Q_{\mathrm{EC}} - E_{4s}$ was analyzed. The sensitivity achievable with this approach is limited by the accuracy on the Q_{EC}-value since the amplitude of the resonances in the spectrum are shaped by the phase space factor which strongly depends on Q_{EC}. In fact, if a Q_{EC}-value smaller than the real one would be assumed in the analysis then, for given
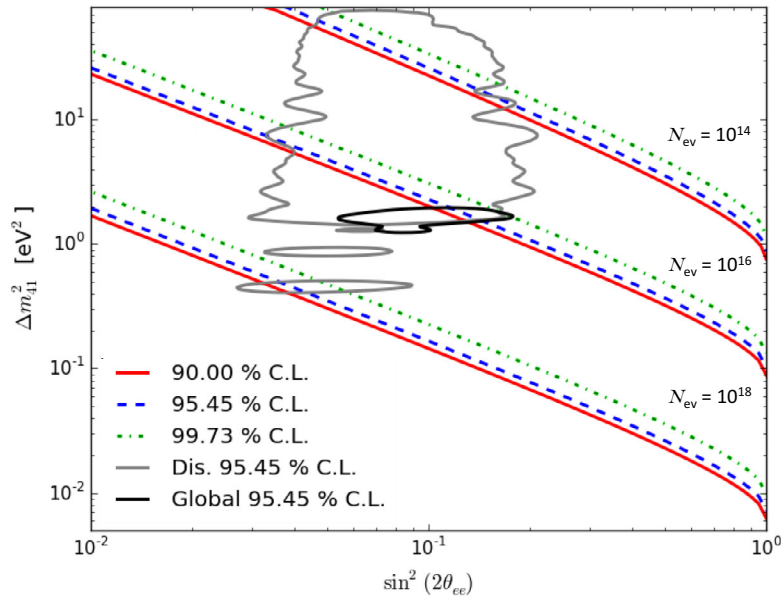
Fig. 36. Estimated sensitivity curves at 90% C.L. (red), 95.45% C.L. (dashed blue) and 99.73% C.L. (dash-dotted green) in the $\sin^2(2\theta_{ee}) - \Delta m_{41}^2$ plane in the case of 3+1 neutrino mixing for total statistics in the ^{163}Ho spectrum of $N_{\rm ev} = 10^{14}$, 10^{16} and 10^{18}. The parameter describing the experimental configuration are discussed in the text. The black curve encloses the region allowed at 95.45% C.L. by a global fit of short-baseline neutrino oscillation data [168]. The gray curves enclose the 95.45% C.L. allowed regions obtained by considering only the data from $\nu_{\rm e}$ and $\bar\nu_{\rm e}$ disappearance experiments [171,172] together with the Mainz [173] and Troitsk [174,175] bounds. The picture is re-elaborated from [170].

atomic physics parameters describing the capture probabilities, the measured ration would be mimic the effect of a keV scale m_4.

To circumvent this problem, the method to identify the kink at $Q_{\rm EC} - m_4$ can be used, as described in [169]. In respect to the previous approach, the precision on the $Q_{\rm EC}$-value affects only the accuracy of m_4, while the amplitude of the kink is related to the squared mixing matrix element. Figure 37 shows the sensitivity that can be reached with 10^{10} and 10^{14} ^{163}Ho events occurring in the detectors. These curves are obtained considering only statistical uncertainties: assuming no background and a perfect knowledge of the spectrum. In case of an experiment with a statistics in the full ^{163}Ho of 10^{14}, as can be reached within ECHo-1M, a sensitivity of about 10^{-7} for the mixing element can be reached for heavy neutrino masses between 1 keV and 2 keV.

In order to investigate the existence of keV sterile neutrinos with the ECHo experiment, it is extremely important to have a perfect knowledge of the ^{163}Ho calorimetric spectrum. The presence of structures in the spectrum due to higher order excited states in ^{163}Dy could be, if not precisely described, a cause of large systematic errors. As already discussed, within the first stage of ECHo, ECHo-1k, one of the milestones is the precise study of the higher order excited states in ^{163}Dy: the excitation probabilities as well as the shape of the related structures in the spectrum. Another aspect that will be addressed within ECHo-1k and that will be fundamental in the search for keV sterile neutrino signatures in the ^{163}Ho EC spectrum is the possibility to fast process a large data flow.
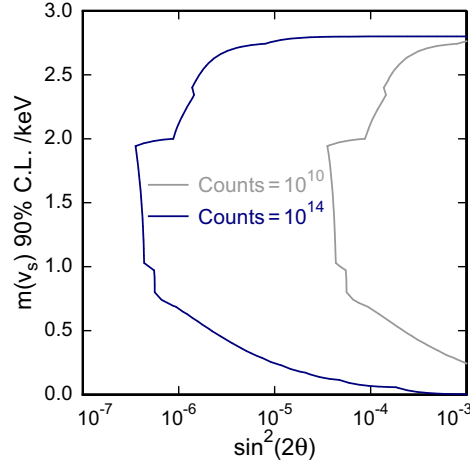
Fig. 37. Estimated sensitivity curves at 90% C.L. in the $\sin^2(2\theta_{ee}) - m_4$ plane in the case of 3+1 neutrino mixing considering keV scale sterile neutrinos. The blue curve is calculated for $N_{ev} = 10^{14}$ while the grey curve is calculated for $N_{ev} = 10^{10}$. The figure is re-elaborated from [169].

13 Conclusions

The determination of the neutrino masses is one of the most difficult challenges in the investigation of the fundamental properties of elementary particles. The ECHo experiment has been conceived to reach sub-eV sensitivity on the electron neutrino mass by the analysis of the endpoint region of the ^{163}Ho electron capture spectrum. The motivations and expectations of the ECHo experiment as well as the first two phases of ECHo have been discussed. ECHo-1k is a three-year project, started in 2015, which will allow to reach a sensitivity below 10 eV for the electron neutrino mass, employing about 1000 Bq of highly radiochemically pure ^{163}Ho. In this first stage of the experiment the present limit on the electron neutrino mass is expected to be improved by more than one order of magnitude with respect to the result obtained in [16]. During ECHo-1k, R&D for up-scaling the size of the experiment by about three orders of magnitude will be carried out. ECHo-1M will be based on the technologies developed during ECHo-1k and will consist of large arrays hosting of the order of one MBq of high purity ^{163}Ho source. This experiment will allow to investigate the electron neutrino mass in the sub-eV region.

On the way to reach sub-eV sensitivity, a large number of cutting edge technologies have to be developed, like the production of large sample of high purity ^{163}Ho as well as the development of large MMC arrays and a precise parameterization of the ^{163}Ho spectrum. Already in the first phase of ECHo-1k very interesting results have been achieved, such as the precise measurement of the Q_{EC}-value [23] and the discovery of spectral structures due to higher order excited states in ^{163}Dy [62]. The possibility to have high statistics ^{163}Ho spectra will not only allow for studying the absolute value of the neutrino mass, but will also open the possibility to perform very interesting investigations like the search for signatures in the spectra due to sterile neutrinos, both on the eV-scale as well on the keV-scale. Results from ECHo are also expected to increase our understanding on the formation of excited states in daughter atoms populated in the electron capture process as well as the influence of the host material on the spectral shape.

References

1. Y. Fukuda et al., Super Kamiokande Collaboration, Phys. Rev. Lett. **81**, 1562 (1998)
2. Q.R. Ahmad et al., (SNO collaboration), Phys. Rev. Lett. **89**, 011301 (2002)
3. G.L. Fogli et al., Phys. Rev. D **84**, 053007 (2011)
4. K.N. Abazajian et al., Astropart. Phys. **35**, 177 (2011)
5. F.T. Avignone III et al., Rev. Mod. Phys. **80**, 481 (2008)
6. F. Simkovic et al., Phys. Rev. C **77**, 045503 (2008)
7. S. Eliseev et al., J. Phys. G: Nucl. Part. Phys. **39**, 124003 (2012)
8. G. Pagliaroli et al., Astropart. Phys. **33**, 287 (2010)
9. G. Drexlin et al., Adv. High Ener. Phys. **2013**, 293986 (2013)
10. KATRIN Design Report, FZKA7090 (2004)
11. Ch. Kraus et al., Eur. Phys. J. C **40**, 447 (2005)
12. Ch. Weinheimer, Prog. Part. Nucl. Phys. **57**, 22 (2006)
13. N. Aseev et al., Phys. Rev D **84**, 112003 (2011)
14. D.M. Asner et al., Phys. Rev. Lett. **114**, 162501 (2015)
15. S. Betts et al., arXiv:`1307.4738`[astro-ph.IM]
16. P.T. Springer et al., Phys. Rev. A **35**, 679 (1987)
17. C.W. Reich, B. Singh, Nuclear Data Sheets **111**, 1211 (2010)
18. P.A. Baisden et al., Phys. Rev. C **28**, 337 (1983)
19. G. Audi et al., The Ame2012 atomic mass evaluation, Chinese Phys. C **36**, 1157 (2012)
20. J.U. Andersen et al., Phys. Lett. B **113**, 72 (1982)
21. F. Gatti et al., Phys. Lett. B **398**, 415 (1997)
22. P.C.-O. Ranitzsch et al., J. Low Temp. Phys. **167**, 1004 (2012)
23. S. Eliseev et al., Phys. Rev. Lett. **115**, 062501 (2015)
24. A. Faessler et al., Phys. Rev. C **91**, 064302 (2015)
25. C.L. Bennett et al., Phys. Lett. B **107**, 19 (1981)
26. S. Yasumi et al., Phys. Lett. B **122**, 461 (1983)
27. S. Yasumi et al., Phys. Lett. B **334**, 229 (1994)
28. A. De Rujula, M. Lusignoli, Phys. Lett. B **118**, 429 (1982)
29. A. De Rujula, arXiv:`1305.4857` (2013)
30. E. Laegsgaard et al., *Proceeding of 7th International Conference on Atomic Masses and Fundamental Constants (AMCO-7)* (1984)
31. F.X. Hartmann, R.A. Naumann, Nucl. Instr. Meth. A **13**, 237 (1992)
32. L. Gastaldo et al., Nucl. Inst. and Meth. A **711**, 150 (2013)
33. L. Gastaldo et al., J. Low Temp. Phys. **176**, 876 (2014)
34. B. Alpert et al., Eur. Phys. J. C **75**, 112 (2015)
35. `http://p25ext.lanl.gov/~kunde/NuMECS/`
36. M.P. Croce et al., J. Low Temp. Phys. **184**, 938 (2016)
37. R.G.H. Robertson, Phys. Rev. C **91**, 035504 (2015)
38. A. Faessler, F. Simkovic, Phys. Rev. C **91**, 045505 (2015)
39. A. De Rujula, M. Lusignoli, arXiv:`1510.05462` (2015)
40. A. De Rujula, M. Lusignoli, arXiv:`1601.04990` (2016)
41. A. Faessler et al., J. Phys. G **42**, 015108 (2015)
42. R.D. Deslattes et al., Rev. Mod. Phys. **75**, 35 (2003)

43. A. Thompson et al., X-ray data booklet (2009), `xdb.lbl.gov`
44. J. Campbell, T. Papp, At. Data Nucl. Data Tables **77**, 1 (2001)
45. R.L. Cohen et al., Phys. Rev. B **5**, 1037 (1972)
46. M. Lusignoli, M.Vignati, Phys. Lett. B **697**, 11 (2011)
47. A. Fleischmann et al., in *Cryogenic Particle Detection (Springer Topics in Applied Physics 99)* ed Enss C (Berlin: Springer) (2005), p. 151
48. A. Fleischmann et al., AIP Conf. Proc. **1185**, 571 (2009)
49. C. Pies et al., J. Low Temp. Phys. **167**, 269 (2012)
50. J.A.B. Mates et al., Appl. Phys. Lett. **92**, 023514 (2008)
51. A. Fleischmann et al., in preparation
52. C. Enss, in *Cryogenic Particle Detection*, Top. Appl. Phys. (2005), Vol. 99
53. A. Enss, D. Mac Cammon, J. Low Temp. Phys. **151**, 5 (2008)
54. K.D. Irwin, G.C. Hilton, Top. Appl. Phys. **99**, 63 (2005)
55. J.-P. Porst et al., J. Low Temp. Phys. **176**, 617 (2014)
56. J.-P. Porst et al., Nucl. Phys. B (Proc. Suppl.) **229-232**, 446 (2012)
57. L. Gastaldo et al., AIP Conf. Proc. **1185**, 607 (2009)
58. A. Fleischmann et al., J. Low Temp. Phys. **118**, 7 (2000)
59. G. Hölzer et al., Phys. Rev. A **56**, 4554 (1997)
60. E. Kugler, Hyperfine Interact. **129**, 23 (2000)
61. A.G. Kozorezov et al., Phys. Rev. B **87**, 104504 (2013)
62. P.C.-O. Ranitzsch, arXiv:**1409.0071**[physics.ins-det] (2014)
63. D. Drung et al., IEEE Trans. Appl. Supercond. **17**, 699 (2007)
64. C. Hassel et al., J. Low Temp. Phys. **184**, 910 (2016)
65. K. Prasai et al., Rev. Sci. Instr. **84**, 083905 (2013)
66. I.M. Band, M.B. Trzhaskovskaya, Atomic Data and Nuclear Data Tables **35**, 1 (1986)
67. J. Clarke, A.I. Braginski, eds., in *The SQUID Handbook: Fundamentals and Technology of SQUIDs and SQUID Systems* (Wiley-VCH, Weinheim, 2004)
68. S. Kempf et al., Supercond. Sci. Technol. **28**, 045008 (215)
69. D. Drung, M. Mück, SQUID electronics *in The SQUID Handbook: Fundamentals and Technology of SQUIDs and SQUID Systems*, edited by J. Clarke and A.I. Braginski (Wiley-VCH, Weinheim, 2004)
70. S.R. Bandler et al., J. Low Temp. Phys. **167**, 254 (2012)
71. J. Beyer, D. Drung, Supercond. Sci. Technol. **21**, 105022 (2008)
72. J.-P. Porst et al., IEEE Trans. Appl. Supercond. **23**, 2500905 (2013)
73. K.D. Irwin, K.W. Lehnert, Appl. Phys. Lett. **85**, 2107 (2004)
74. K.W. Lehnert et al., IEEE Trans. Appl. Supercond. **17**, 705 (2007)
75. J.M. Goodkind, D.L. Stolfa, Rev. Sci. Instrum. **41**, 799 (1970)
76. P.K. Hansma, J. Appl. Phys. **44**, 4191 (1973)
77. R. Rifkin et al., J. Appl. Phys. **47**, 2645 (1976)
78. S. Kempf et al., J. Low Temp. Phys. **175**, 850 (2014)
79. J.A.B. Mates et al., J. Low Temp. Phys. **167**, 707 (2012)
80. B.A. Mazin et al., Nucl. Instr. Meth. A **559**, 799 (2006)
81. S.J.C. Yates et al., Appl. Phys. Lett. **95**, 042504 (2009)
82. R. Duan et al., Proc. of SPIE **7741**, 77411 (2010)
83. S. Kempf et al., J. Low Temp. Phys. **176**, 426 (2014)
84. S. Kempf et al., AIP Advances **7**, 015007 (2017)
85. C. Bueno, Radiographic Testing, in *Nondestructive testing handbook*, 3rd edn (The American Society for Nondestructive Testing, Columbus, OH, USA, 2002), Vol. 4
86. D. Rowe, Appl. Energ. **40**, 241 (1991)
87. J. Runke et al., J. Radioanal. Nucl. Chem. **299**, 1081 (2014)
88. J. Magill et al., *Karlsruher Nuklidkarte*, 8th edn. (Nucleonica GmbH, 76344 Eggenstein-Leopoldshafen, Germany, 2012)
89. J.W. Engle et al., Nucl. Instrum. Meth. B **311**, 131 (2013)
90. S. Niese et al., J. Radioanal. Nucl. Chem. **233**, 167 (1998)
91. G. Heusser. Annu. Rev. Nucl. Part. Sci. **45**, 543 (1995)

92. J. Korkisch. *CRC Handbook of Ion Exchange Resins*, Vol. I-V (CRC Press, Boca Raton, FL, USA, 1988)
93. V. Mocko et al., Radiochim. Acta **103**, 577 (2015)
94. H.L. Ravn et al., AIP Conf. Proc. **99**, 1 (1983)
95. M. Fujioka et al., CYRIC Ann. Rep. **1981**, 25 (1981)
96. M. Blann, H.K. Vonach, Phys. Rev. C **28**, 1475 (1983)
97. K. Katsube et al., CYRIC Ann. Rep. **1982**, 28 (1982)
98. F. Tárkányi et al., Appl. Radiat. Isot. **98**, 87 (2015)
99. O. Kawakami et al., Phys. Rev. C **38**, 1857 (1988)
100. A. Koning et al., *TALYS-1.0* (EDP Sciences, 2007), p. 58
101. Z. Szucs et al., in *Proceedings of the third international conference on application of radiotracers and energetic beams in sciences: extended abstracts of the plenary lectures and contributed papers* (2014)
102. M. Maiti et al., in *International Conference on Modern Trends in Activation Analysis 14 (MTAA 14)* (2015)
103. M. Maiti et al., J. Radioanal. Nucl. Chem. **307**, 1667 (2016)
104. S. Lahiri et al., Appl. Radiat. Isot. **51**, 27 (1999)
105. S. Lahiri et al., Appl. Radiat. Isot. **61**, 1157 (2004)
106. R.A. Naumann et al., J. Inorg. Nucl. Chem. **15**, 195 (1960)
107. N. Holden, Neutron Scattering and Absorption Properties, in *CRC Handbook of Chemistry and Physics*, cd-rom edn. (CRC Press, Boca Raton, FL, USA, 2006), p. 11
108. U. Köster et al., Radiother. Oncol. **102**, S102 (2012)
109. P. Armbruster et al., Phys. Rev. Lett. **54**, 406 (1985)
110. N. Trautmann, H. Folger, Nucl. Instrum. Meth. A **282**, 102 (1989)
111. K. Eberhardt et al., Nucl. Instrum. Meth. A **521**, 208 (2004)
112. K. Zimmer. Ph.D. thesis, Johannes Gutenberg-Universität Mainz, 1995
113. F. Schneider et al., Nucl. Instrum. Meth. B **376**, 388 (2016)
114. H. Dorrer et al., to be submitted in Radiochim. Acta
115. L. Monz et al., Spectrochim. Acta B **48**, 1655 (1993)
116. K. Wendt. Eur. J. Mass Spectrom. **8**, 273 (2002)
117. T. Gottwald et al., AIP Conf. Proc. **1104**, 138 (2009)
118. T. Kieck et al., to be submitted to NIM B
119. D. Liebe et al., Nucl. Instrum. Meth. A **590**, 145 (2008)
120. F. Schneider et al., Eur. Phys. J. A **51**, 89 (2015)
121. J. Repp et al., Appl. Phys. B **107**, 983 (2012)
122. C. Sailer, Diploma thesis, Physikalisches Institut der Eberhard Karls Universität Tübingen, 2008
123. M. Köhler et al., Appl. Rad. Isot. **67**, 736 (2009)
124. S. Agostinelli et al., Nucl. Instr. Meth. A **506**, 250 (2003)
125. J. Allison et al., IEEE Trans. Nucl. Sci. **53**, 270 (2006)
126. D.S. Leonard et al. (EXO-Collaboration), Nucl. Inst. Meth. A **591**, 490 (2008)
127. International Commission on Radiation Units and Measurements, *Stopping Powers for Electrons and Positrons*, *ICRU Report* **37** (1984).
128. `http://www.nndc.bnl.gov/`
129. C.M. Baglin, Nuclear Data Sheets for A = 166, Nucl. Data Sheets **109**, 1103 (2008)
130. S.Y.F. Chu, L.P. Ekström, R.B. Firestone, *The Lund/LBNL Nuclear Data Search, Version 2.0, Feb. 1999*, `http://nucleardata.nuclear.lu.se/toi/xray.asp`
131. K. Blaum, Phys. Rep. **425**, 1 (2006)
132. K. Blaum et al., Phys. Scr. **T152**, 014017 (2013)
133. L.S. Brown, G. Gabrielse, Rev. Mod. Phys. **58**, 233 (1986)
134. L.S. Brown, G. Gabrielse, Phys. Rev. A **25**, 2423 (1982)
135. M. König et al., Int. J. Mass Spectrom. **142**, 95 (1995)
136. K. Blaum et al., Eur. Phys. J. A **15**, 245 (2002)
137. H. Dehmelt, F. Walls, Phys. Rev. Lett. **21**, 127 (1968)

138. M. Kretzschmar, Int. J. Mass Spectrom. **264**, 122 (2007)
139. S. George et al., Phys. Rev. Lett. **98**, 162501 (2007)
140. S. George et al., Int. J. Mass Spectrom. **264**, 110 (2007)
141. S. Eliseev et al., Phys. Rev. Lett. **110**, 082501 (2013)
142. S. Eliseev et al., Appl. Phys. B **114**, 107 (2014)
143. M. Block et al., Eur. Phys. J. D **45**, 39 (2007)
144. W. Shi et al., Phys. Rev. A **72**, 022510 (2005)
145. S. Streubel et al., Appl. Phys. B **114**, 137 (2014)
146. S. Sturm et al., Nature **506**, 467 (2014)
147. F. Hartmann, R. Naumann Phys. Rev. C **31**, 1594 (1985)
148. S. Yasumi et al., Phys. Lett. B **181**, 169 (1986)
149. F. Bosch, M. Jung, GSI Annual Rep. 65, 1993
150. J. Ketelaer et al., Nucl. Instr. Meth. A **594**, 162 (2008)
151. A. Chaudhuri et al., Eur. Phys. J. D **45**, 47 (2007)
152. G. Savard et al., Phys. Lett. A **158**, 247 (1991)
153. K. Blaum et al., J. Phys. B **36**, 921 (2003)
154. C. Roux et al., Appl. Phys. B **107**, 997 (2012)
155. Th. A. Carlson et al., Phys. Rev. **169**, 27 (1968)
156. Th. A. Carlson, C. W. Nestor, Phys. Rev. A **8**, 2887 (1973)
157. I. P. Grant, Adv. Phys. **19**, 747 (1970)
158. J. P. Desclaux, Comp. Phys. Com. **9**, 31 (1975)
159. A.L. Ankudinov et al., Comp. Phys. Com. **98**, 359 (1996)
160. P.-O. Loewdin Phys. Rev. Lett. **97**, 1474 (1955)
161. E. Vatai, Nucl. Phys. **A156**, 541 (1970)
162. E. Vatai, Nucl. Phys. **A402**, 1 (1983)
163. K. Blaum K et al., Contem. Phys. **51**, 149 (2010)
164. `www.dreebit.com`
165. J.R. Crespo Lopez-Urrutiaet al., Hyperfine Interact. **127**, 497 (2000)
166. S. Sturm et al., Phys. Rev. Lett. **107**, 143003 (2011)
167. K.N. Abazajian et al., arXiv:**1204.5379**[hep-ph] (2012)
168. S. Gariazzo et al., J. Phys. G **43**, 033001 (2016)
169. R. Adhikari et al., JCAP **01**, 025 (2017)
170. L. Gastaldo et al., JHEP **06**, 061 (2016)
171. C. Giunti et al., Phys. Rev. D **86**, 113014 (2012)
172. C. Giunti et al., Phys. Rev. D **87**, 013004 (2013)
173. C. Kraus et al., Eur. Phys. J. C **73**, 2323 (2013)
174. A.I. Belesev et al., JETP Lett. **97**, 67 (2013)
175. A.I. Belesev et al., J. Phys. G **41**, 015001 (2014)
176. A. Esmaili, O. Peres, Phys. Rev. D **85**, 117301 (2012)
177. P.E. Filianin et al., J. Phys. G **41**, 095004 (2014)
178. L. Fleischmann et al., IEEE Trans. Appl. Supercond. **19**, 63 (2009)
179. P. Filianin et al., Phys. Lett. B **758**, 457 (2016)